$SO(N)$ gauge theories in $2+1$ dimensions

Richard Lau
St John's College, Oxford

A thesis submitted for the degree of Doctor of Philosophy
at the University of Oxford.

Trinity Term, 2014

Abstract

We calculate the string tensions, mass spectrum, and deconfining temperatures of $SO(N)$ gauge theories in $2+1$ dimensions. After a review of lattice field theory, we describe how we simulate the corresponding lattice gauge theories, construct operators to project on to specific states, and extrapolate values to the continuum limit. We discuss how to avoid possible complications such as finite size corrections and the bulk transition.

$SO(N)$ gauge theories have become recently topical since they do not have a fermion sign problem, are orbifold equivalent to $SU(N)$ gauge theories, and share a common large-N limit in their common sector of states with $SU(N)$ gauge theories. This motivates us to compare the physical properties of $SO(N)$ and $SU(N)$ gauge theories between 'group equivalences', which includes Lie algebra equivalences such as $SO(6)$ and $SU(4)$, and particularly a large-N equivalence. We discuss the large-N orbifold equivalence between $SO(N)$ and $SU(N)$ gauge theories, which relates the large-N gauge theories perturbatively. Using large-N extrapolations at fixed 't Hooft coupling, we test to see if $SO(N)$ gauge theories and $SU(N)$ gauge theories share non-perturbative properties at the large-N limit. If these group equivalences lead to similar physics in the gauge theories, then we could imagine doing finite chemical potential calculations that are currently intractable in $SU(N)$ gauge theories by calculating equivalent quantities in the corresponding $SO(N)$ gauge theories.

We show that the $SO(N)$ and $SU(N)$ values match between group equivalences and at the large-N limit.

Acknowledgements

I could not have written this thesis without the help of many people during my time at Oxford.

I thank Mike Teper, my supervisor and the one who introduced me to lattice field theory and to this project. Mike supported me throughout my time at Oxford, answered my many questions when I didn't know what to do, provided guidance when I found something surprising, and offered reassurance when I got it right. I am very grateful and I hope that Mike will enjoy a well-deserved break.

I thank the department for giving me this opportunity and to Michelle for helping me through all the logistics. I am grateful for the support I received from St John's College, and it was a privilege to work with people there to make it a better place for graduates. I was funded by a doctoral training grant from the Science and Technology Facilities Council.

When I look back at my time in Oxford, I will remember the many friends who supported me. I thank David for our chats and for always being optimistic, Ed for pushing me to do new things and for being there for me, Madu for our MCR adventure and for providing advice, Rory for keeping me in shape and for taking time to share perspectives on life, and to Elizabeth, Gaëlle, John, Prelisha, Rhorry, and many others for being great friends.

Finally, I thank Mum, Dad, and Jennie, who supported me through everything and inspired me throughout university.

Contents

Introduction

In this thesis, we will consider the physical properties of $SO(N)$ pure gauge theories in $2+1$ dimensions. We will calculate the string tensions, mass spectrum, and deconfining temperatures in the continuum limit of various $SO(N)$ gauge theories, and then extrapolate those values to the large-N limit. Finally, we will compare our $SO(N)$ results to known $SU(N)$ values between group equivalences.

$SO(N)$ and $SU(N)$ gauge theories share several equivalences. Some of these equivalences are Lie algebra equivalences between specific groups such as $SO(4)$ and $SU(2) \times SU(2)$ or $SO(6)$ and $SU(4)$. In addition, recent papers also describe a large-N equivalence between $SO(N)$ and $SU(N)$ gauge theories on a perturbative level. These equivalences motivate us to ask just how similar are $SO(N)$ and $SU(N)$ gauge theories. If they are similar, understanding these equivalences might help us to understand current problems in $SU(N)$ QCD, for example, QCD at finite chemical potential. We then could calculate quantities in $SO(N)$ gauge theories that are intractable in the equivalent $SU(N)$ gauge theories.

To understand fully the physics of $SO(N)$ and $SU(N)$ gauge theories, we need to consider their non-perturbative properties. However, analytic attempts to understand their non-perturbative physics such as confinement or the glueball spectrum have been mostly unsuccessful as they have no perturbative explanation. Hence, we take two alternative approaches. Firstly, we use lattice field theory to investigate non-perturbative properties. On the lattice, we use a discretised theory on a finite spacetime volume where the finite lattice spacing introduces an ultraviolet cutoff and the finite volume introduces an infrared cutoff. Secondly, we use an alternative expansion parameter instead of the running coupling in QCD. 't Hooft proposed that the natural expansion parameter for $SU(N)$ gauge theories should be $1/N$ and that the corrections from finite $SU(N)$ to $SU(N \to \infty)$ are $\mathcal{O}(1/N^2)$ for pure gauge theories. Adapting this argument, we will see that the natural expansion parameter for $SO(N)$ gauge theories is again $1/N$ and that the corrections from finite $SO(N)$ to

$SO(N \to \infty)$ are $\mathcal{O}(1/N)$ for pure gauge theories. This allows us to extrapolate to the large-N limit.

This motivates the large-N approach in this thesis. We can use the large-N equivalence to connect $SO(N \to \infty)$ and $SU(N \to \infty)$ gauge theories, while the large-N arguments connect finite $SO(N)$ to $SO(N \to \infty)$ and finite $SU(N)$ to $SU(N \to \infty)$. Collectively, this provides a route between $SO(N)$ and $SU(N)$ gauge theories. This could allow us to discuss $SU(N)$ QCD through considering $SO(N)$ physics. Hence, by calculating the physical properties of $SO(N)$ gauge theories and considering the values between group equivalences and at the large-N limit, we see how we might relate $SO(N)$ and $SU(N)$ gauge theories.

Thesis Structure

In Chapter 1, we review the basic ideas of lattice field theory. We describe the lattice setup, the physics in $2+1$ dimensions, the process behind numerical simulations, and the method behind calculating masses.

In Chapter 2, we discuss the equivalences between $SO(N)$ and $SU(N)$ gauge theories. We start by considering specific Lie algebra equivalences between $SO(N)$ and $SU(N)$ groups such as $SO(4)$ and $SU(2) \times SU(2)$, and $SO(6)$ and $SU(4)$. We then go on to look at physics in the large-N limit. Firstly, we discuss 't Hooft's $1/N$ argument, applying it to the familiar case of $SU(N)$ gauge theories and then to the case of $SO(N)$ gauge theories. We show that the leading correction to the $SO(N \to \infty)$ limit is $\mathcal{O}(1/N)$ for pure gauge theories, allowing us to extrapolate to the large-N limit. Secondly, we describe the large-$\tilde{N}$ orbifold equivalence between $SO(2\tilde{N})$ and $SU(\tilde{N})$ gauge theories through which we can obtain large-$\tilde{N}$ $SU(\tilde{N})$ QCD from large-$\tilde{N}$ $SO(2\tilde{N})$ QCD-like theories under specific conditions. Finally, we consider one possible application for $SO(N)$ physics, which is the fermion sign problem. This problem currently prevents us from investigating $SU(N)$ QCD at finite chemical potential in lattice field theory whereas the problem does not affect $SO(N)$ gauge theories.

In Chapter 3, we calculate $SO(N)$ string tensions. We discuss the operators that we use and string tension models before calculating the string tensions in the continuum limit for different $SO(N)$ values. We then extrapolate to the large-N limit. We will show that the string tensions agree between group equivalences and that there is excellent agreement between the $SO(N \to \infty)$ and $SU(N \to \infty)$ values.

In Chapter 4, we calculate the $SO(N)$ mass spectrum. We again discuss the operators we use and how to minimise finite size corrections. We then calculate the $SO(N)$ mass spectra in the continuum limit before extrapolating to the large-N limit. We will show that the mass spectrum agree well between group equivalences and between the $SO(N \to \infty)$ and $SU(N \to \infty)$ values.

In Chapter 5, we calculate $SO(N)$ deconfining temperatures. We discuss the deconfinement phase transition, the principles of finite size scaling, and the order parameter that we use. We then explain the reweighting method we use to calculate deconfining temperatures before applying it to calculate the continuum limits and the large-N limit. We will show that the deconfining temperatures agree very well between group equivalences between the $SO(N \to \infty)$ and $SU(N \to \infty)$ values.

Conventions

In this thesis, we will use the following conventions.

We use N to refer to general $SO(N)$ and $SU(N)$ gauge groups. When we refer to odd or even N for $SO(N)$ gauge groups, we use $SO(2\tilde{N})$ and $SO(2\tilde{N}+1)$ respectively where $\tilde{N} \in \mathbb{N}$.

We set the lattice spacing to be a. We relate a physical length l to a lattice length L by $l = aL$.

We use U_p or $U_{\mu\nu}$ to represent the plaquette, the ordered product of link variables about a square with length a in directions μ and ν. We take the trace of the plaquette to form a colour singlet operator.

We use l_P to represent the Polyakov loop, the trace of a closed loop winding around the lattice in a particular direction. The Polyakov loop is a colour singlet operator since its definition includes the trace.

Chapter 1

Lattice field theory

In this chapter, we introduce lattice field theory. We consider how to relate lattice field theory and continuum field theory, the features of $D = 2 + 1$ gauge theories, the process of numerical simulations, and how we calculate masses.

1.1 Setting up the lattice

1.1.1 The lattice

We start by constructing a cubic lattice in $2 + 1$ dimensions. We set the lattice spacing to be a and, in lattice units, the length of the spatial directions to be L_s and in the temporal direction to be L_t. Hence, the lattice volume is $L_s^2 L_t$ in lattice units and $a^3 L_s^2 L_t$ in physical length units. We can construct general orthonormal vectors $\hat{\mu}, \hat{\nu}, \ldots$ of length a, which point in the lattice directions $\mu, \nu, \ldots$. We set the temporal direction to be the third direction and we can explicitly order the orthonormal vectors $\hat{x}$, $\hat{y}$, and $\hat{t}$, which point in the first, second, and third directions respectively. The sites on the lattice are at physical positions $\mathbf{x} = a(x, y, t)$ where $x, y \in \{0, 1, \ldots, L_s - 1\}$ and $t \in \{0, 1, \ldots, L_t - 1\}$.

We can then construct oriented link variables that connect nearest neighbour lattice sites. A link variable $U_\mu(\mathbf{x})$ connects a site $\mathbf{x}$ to a site $\mathbf{x} + \hat{\mu}$ in the direction μ. We set periodic boundary conditions in all lattice directions, forming tori. The link variables are elements of a gauge group such as $SO(N)$ or $SU(N)$. We can define a link variable pointing in the direction $-\hat{\mu}$ by

$$U_{-\mu}(\mathbf{x}) = \begin{cases} U_\mu(\mathbf{x} - \hat{\mu})^T & SO(N) \\ U_\mu(\mathbf{x} - \hat{\mu})^\dagger & SU(N) \end{cases} \tag{1.1}$$

1.1.2 Gauge transformations

We now consider how products of link variables transform under gauge transformations. We define $SO(N)$ or $SU(N)$ gauge transformations $\{\Omega(\mathbf{x})\}$ such that the link variables $U_\mu(\mathbf{x})$ transform as

$$U_\mu(\mathbf{x}) \to U'_\mu(\mathbf{x}) = \begin{cases} \Omega(\mathbf{x})U_\mu(\mathbf{x})\Omega(\mathbf{x}+\hat{\mu})^T & SO(N) \\ \Omega(\mathbf{x})U_\mu(\mathbf{x})\Omega(\mathbf{x}+\hat{\mu})^\dagger & SU(N) \end{cases} \tag{1.2}$$

We can form curves from the link variables connecting a site $\mathbf{x}$ to a site $\mathbf{y}$ by an ordered product of links $P[U]$

$$P[U] = U_{\mu_1}(\mathbf{x})U_{\mu_2}(\mathbf{x}+\hat{\mu}_1)\cdots U_{\mu_n}(\mathbf{y}-\hat{\mu}_n) \tag{1.3}$$

Then this ordered product of links $P[U]$ transforms as

$$P[U] \to P[U'] = \begin{cases} \Omega(\mathbf{x})P[U]\Omega(\mathbf{y})^T & SO(N) \\ \Omega(\mathbf{x})P[U]\Omega(\mathbf{y})^\dagger & SU(N) \end{cases} \tag{1.4}$$

Hence, traces of link variable products on closed curves on the lattice are invariant under gauge transformations.

1.1.3 Gauge invariant objects

We can construct gauge invariant objects on the lattice by considering traces of closed curves. A plaquette U_p is a square with unit lattice length and is the simplest, non-trivial closed curve on the lattice. A Polyakov loop l_P is the trace of a closed loop that winds around the torus in a lattice direction.

$$\begin{aligned} U_p(\mathbf{x},\hat{\mu},\hat{\nu}) &= U_\mu(\mathbf{x})U_\nu(\mathbf{x}+\hat{\mu})U_{-\mu}(\mathbf{x}+\hat{\mu}+\hat{\nu})U_{-\nu}(\mathbf{x}+\hat{\nu}) \\ l_P(\mathbf{x},\hat{\mu}) &= \mathrm{tr}\left(U_\mu(\mathbf{x})U_\mu(\mathbf{x}+\hat{\mu})\cdots U_\mu(\mathbf{x}-\hat{\mu})\right) \end{aligned} \tag{1.5}$$

We display examples of these objects in Figure 1.1.

1.1.4 Relating continuum fields to lattice fields

In a continuum gauge theory with continuum gauge fields A_μ, we can define a continuum gauge transporter $G(\mathbf{x},\mathbf{y})$, which is the path-ordered exponential of the continuum gauge fields along a curve $\mathcal{C}_{\mathbf{x}\to\mathbf{y}}$ connecting points $\mathbf{x}$ to $\mathbf{y}$.

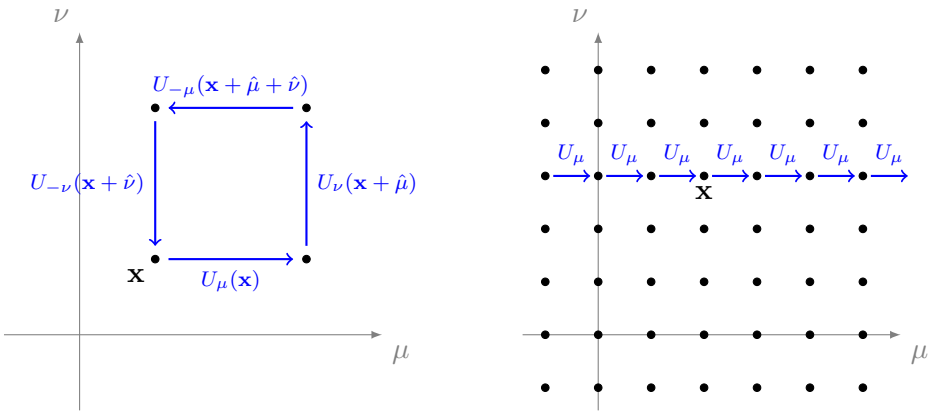

Figure 1.1: A plaquette (left) and the closed curve (right) that forms a Polyakov loop.

$$G(\mathbf{x},\mathbf{y}) \equiv P\exp\left(i\int_{\mathcal{C}_{\mathbf{x}\to\mathbf{y}}} \mathbf{A}\cdot\mathbf{dx}\right) \tag{1.6}$$

Under a set of $SO(N)$ or $SU(N)$ continuous gauge transformations $\{\Omega(\mathbf{x})\}$, the continuum gauge transporter then transforms as

$$G(\mathbf{x},\mathbf{y}) \to G'(\mathbf{x},\mathbf{y}) = \begin{cases} \Omega(\mathbf{x})G(\mathbf{x},\mathbf{y})\Omega(\mathbf{y})^T & SO(N) \\ \Omega(\mathbf{x})G(\mathbf{x},\mathbf{y})\Omega(\mathbf{y})^\dagger & SU(N) \end{cases} \tag{1.7}$$

We see that continuum gauge transporters transform in the same way as link variable products $P[U]$ in (1.4). Hence, we can relate gauge transporters G in the continuum to link variable products $P[U]$ on the lattice by discretising the continuous path $\mathcal{C}_{\mathbf{x}\to\mathbf{y}}$ as a lattice link variable path.

$$G(\mathbf{x},\mathbf{y}) \leftrightarrow P[U] = U_{\mu_1}(\mathbf{x})\cdots U_{\mu_n}(\mathbf{y}-\hat{\mu}_n) \tag{1.8}$$

Finally, we can then define lattice gauge fields $A_\mu(\mathbf{x})$, which are the lattice analogues of continuum gauge fields A_μ, and express link variables in terms of the lattice gauge fields.

$$U_\mu(\mathbf{x}) = \exp\left(iaA_\mu(\mathbf{x})\right) \tag{1.9}$$

1.1.5 The lattice field theory action

We can construct an $SO(N)$ lattice gauge action βS in $2+1$ dimensions

$$\begin{aligned} \beta S &= \beta\sum_p \left(1 - \frac{1}{N}\mathrm{tr}(U_p)\right) \\ \beta &= \frac{2N}{ag^2} \end{aligned} \tag{1.10}$$

where β is the inverse coupling and the lattice action sums over all plaquettes on the lattice. In

$D = 2+1$, the coupling $g = g(a)$ has dimensions of mass so we need a factor of a in our definition of β so that β is dimensionless. This expression for the lattice action differs slightly from the corresponding $SU(N)$ lattice gauge action since we do not need to take explicitly the real part of the trace since all $SO(N)$ traces are real. We can expand our expression for the lattice action in terms of the lattice gauge fields using (1.9).

$$\begin{aligned} \beta S &= \frac{a^3}{2g^2} \sum_{\mathbf{x}} \sum_{\mu<\nu} \mathrm{tr}\left(F_{\mu\nu}^2(\mathbf{x})\right) + \mathcal{O}(a^5) \\ F_{\mu\nu}(\mathbf{x}) &= \partial_\mu A_\nu(\mathbf{x}) - \partial_\nu A_\mu(\mathbf{x}) + i\left[A_\mu(\mathbf{x}), A_\nu(\mathbf{x})\right] \end{aligned} \tag{1.11}$$

where $F_{\mu\nu}$ is the continuum field strength tensor. Then by taking the continuum limit $a \to 0$, we find that the lattice action becomes the continuum action for an $SO(N)$ gauge theory in $2+1$ dimensions.

$$\beta S \xrightarrow[a\to 0]{} \frac{1}{2g^2} \int d^3x \, \mathrm{tr}\left(F_{\mu\nu}^2(\mathbf{x})\right) \tag{1.12}$$

We note that the leading order correction in (1.11) is $\mathcal{O}(a^2)$ from the $\mathcal{O}(a^5)$ term relative to the $\mathcal{O}(a^3)$ coefficient in the $F_{\mu\nu}^2$ term. This implies that the leading order correction to operator expectation values on finite lattices is also $\mathcal{O}(a^2)$. Measurements of physical masses will also have these $\mathcal{O}(a^2)$ corrections. Finally, we already know that the leading order correction to a dimensionless ratio of physical quantities such as $m_G/\sqrt{\sigma}$ or $T_c/\sqrt{\sigma}$ is also $\mathcal{O}(a^2)$ [1]. This will help us to calculate the continuum values in the limit $a \to 0$.

1.2 $D = 2+1$ gauge theories

1.2.1 The coupling g^2

As we noted above, the coupling g^2 has dimensions of mass in $D = 2+1$ whereas, in contrast, g^2 is dimensionless in $D = 3+1$. However, both $D = 2+1$ and $D = 3+1$ gauge theories share important dynamical properties [2].

Both theories are ultraviolet free. In $D = 2+1$, g^2 has dimensions of mass. Hence, if we use a power expansion in g^2 to calculate a quantity whose characteristic length scale is l, then we need to couple g^2 with l to create a dimensionless quantity. Hence, we define an effective dimensionless 'running' coupling parameter $g^2_{2+1}(l)$, which vanishes linearly with l as $l \to 0$.

$$g^2_{2+1}(l) \equiv g^2 l \xrightarrow[l\to 0]{} 0 \tag{1.13}$$

This effective coupling runs faster than the dimensionless coupling $g^2_{3+1}(l)$ in $D = 3+1$, which runs logarithmically with l.

$$g^2_{3+1}(l) \sim \frac{1}{\ln(l\Lambda)} \xrightarrow[l\to 0]{} 0 \tag{1.14}$$

where Λ is the QCD scale. We can alternatively see that the couplings become strong at large distances. This implies that the physics at large scales is non-perturbative.

In $D = 2+1$, the coupling has mass dimensions and hence it sets the scale for massive quantities $m = cg^2$ where m is any dynamically generated mass in the theory. This is actually the same as $D = 3+1$ physics where the running coupling introduces the QCD mass scale related to the running rate $m = c\Lambda$. Hence, the coupling sets the mass scale for both $D = 2 + 1$ and $D = 3 + 1$.

1.2.2 Confinement

We expect both $D = 2+1$ and $D = 3+1$ gauge theories to be linearly confining, which is something we hope to show in the case of $D = 2 + 1$. In $D = 2 + 1$, the Coulomb potential V_C is weakly confining, $V_C(r) \sim g^2 \ln(r)$. This is distinct from the non-perturbative linear potential $V(r) \sim r$, which we see at large r.

1.2.3 Parity doubling

In $D = 2 + 1$, spatial rotations commute so that states of spin J do not form the spin multiplets in $D = 3 + 1$ dimensions [2]. Under the parity transformation P, spatial coordinates transform as $P(x, y) = (x, -y)$. Hence, the angular momentum operator $x\partial_y - y\partial_x$ changes signs under P so that, if a state $|j\rangle$ has spin $J = j$, then $P|j\rangle$ has spin $J = -j$.

Consider a state $|j\rangle$ with spin $J = j$ and energy E_j and the two linear combinations

$$|j, \pm\rangle = |j\rangle \pm P|j\rangle \tag{1.15}$$

If they are non-null, then they form a pair of opposite parity states since $P|j, \pm\rangle = \pm|j, \pm\rangle$. These states are also degenerate since P and the Hamiltonian H commute. This means that we see parity doubling: degenerate states with the same spin but opposite parity. For $j \neq 0$, $|j\rangle$ and $P|j\rangle$ are orthogonal since they have eigenvalues $\pm j$ under the spin operator J so that the states in (1.15) are non-null. However, they are not necessarily non-null if $J = 0$. So we expect parity doubling for

$J \neq 0$ but not necessarily for $J = 0$.

We note that the argument above depends on using the continuum rotation group. However, on the square lattice, the explicit symmetries are $\pi/2$ rotations, which can affect the opposite parity states we described above. Consider states with spin $J = \pm j$ that, under a rotation θ, transform by a phase of $e^{\pm ij\theta}$. Then, if we rotate by $\theta = n\pi/2$, we see that these phases are the same for $J = 2$. Hence, parity doubling for $J = 2$ can break since these are the states that constructed the opposite parity states in (1.15). As the lattice spacing a decreases, we increasingly recover the continuum rotational symmetry and so we expect to recover $J = 2$ parity doubling. Similarly, we break the continuum rotational symmetry by having a finite spatial volume with periodic boundary conditions. Since the spatial lengths are the same, we again have rotations by $\pi/2$, which can break $J = 2$ parity doubling. As we increase the volume size past the physical length scale, we again expect to recover $J = 2$ parity doubling.

1.2.4 Bulk transition

One difference between $D = 2 + 1$ and $D = 3 + 1$ gauge theories is the location of the bulk transition. At this transition, the system moves from strong coupling to weak coupling, and the coupling expansion changes from powers of $\beta \propto 1/(ag^2)$ to $1/\beta \propto ag^2$ respectively. We can only extrapolate to the continuum limit $a \to 0$ in the weak coupling region so it is important to know where this bulk transition occurs. For $D = 3+1$ $SU(2)$ gauge theory in the adjoint representation, there is a bulk transition at a very small lattice spacing (see discussion in [3]). Since the $SU(2)$ adjoint representation is equivalent to the $SO(3)$ fundamental representation, this indicates that the location of the bulk transition may prevent us from investigating the $D = 3 + 1$ $SO(N)$ continuum limit. In fact, in the case of $D = 3+1$ $SO(3)$, initial results in [3] indicate that we need extremely large lattices to reach the confined phase. In contrast, the position of the bulk transition in $D = 2+1$ $SO(N)$ gauge theories is at a larger lattice spacing, allowing us to reach the $D = 2+1$ $SO(N)$ continuum limit. We will look at this in more detail later in this thesis. It is for this reason, and because of the similarities between $D = 2 + 1$ and $D = 3 + 1$ gauge theories explained above, that we look at $D = 2 + 1$ gauge theories in this thesis.

1.3 Numerical simulation of lattice field theory

1.3.1 Calculating observables

We define the partition function Z by

$$Z = \int \mathcal{D}[U] e^{-\beta S[U]}$$
$$\int \mathcal{D}[U] = \prod_{\mathbf{x}} \prod_{\mu} \int dU_\mu(\mathbf{x}) \tag{1.16}$$

where the Haar measure $\int \mathcal{D}[U]$ is a product over link variables U.

For an observable O, we can define an expectation value $\langle O \rangle$ and then approximate $\langle O \rangle$ with N different link variable configurations $\mathcal{U}_1, \mathcal{U}_2, \ldots, \mathcal{U}_N$

$$\langle O \rangle = \frac{1}{Z} \int \mathcal{D}[U] e^{-\beta S[U]} O[U]$$
$$\langle O \rangle \approx \frac{1}{N} \sum_{n=1}^{N} O[\mathcal{U}_n] \Big|_{\mathcal{P}[\mathcal{U}_n] \propto e^{-\beta S}} \tag{1.17}$$

where we assign to a configuration $\mathcal{U}$ a probability weight $\mathcal{P}[\mathcal{U}]$ proportional to its lattice action value. This allows us to sample statistically an estimate of $\langle O \rangle$ with finitely many configurations $\mathcal{U}$.

1.3.2 Heat bath algorithm

We need to equilibrate and update the lattice to obtain measurements at equilibrium. To do this, we use a heat bath algorithm. Consider a link U and the sum V of its four staples, defined for a link $U_\mu(x)$ by

$$V = \sum_{\nu \neq \mu} (U_\nu(x+\hat{\mu}) U_{-\mu}(x+\hat{\mu}+\hat{\nu}) U_{-\nu}(x+\hat{\nu})) + (U_{-\nu}(x+\hat{\mu}) U_{-\mu}(x+\hat{\mu}-\hat{\nu}) U_\nu(x-\hat{\nu})) \tag{1.18}$$

Using the Cabibbo-Marinari algorithm (see below), we isolate 2×2 submatrices of the matrix UV. Consider the case when $U \in SO(2)$. Using the heat bath, we update $U \to U'$ by randomly selecting U' from a probability distribution derived from the partition function [4, 5].

$$\mathrm{d}P(U) \sim \exp\left(\beta \tfrac{1}{N} \mathrm{tr}(UV)\right) \tag{1.19}$$

Each staple is an $SO(2)$ matrix so that the sum V is proportional to an $SO(2)$ matrix $\bar{V}$, $V = k\bar{V}$ where $k = \sqrt{\det(V)}$. We can express U as

$$
\begin{aligned}
U &= \begin{pmatrix} a_0 & a_1 \\ -a_1 & a_0 \end{pmatrix} && a_0^2 + a_1^2 = 1 \\
\Rightarrow \qquad \mathrm{d}P(U\bar{V}^{-1}) &\propto \mathrm{d}a_0\, \mathrm{d}a_1\ \delta(a_0^2 + a_1^2 - 1) \exp\left(\frac{2\beta k}{N} a_0\right) \\
&\propto \mathrm{d}a_0\, (1 - a_0^2)^{-1/2} \exp\left(\frac{2\beta k}{N} a_0\right) && a_1 = \pm(1 - a_0^2)^{1/2} \qquad (1.20)
\end{aligned}
$$

where we randomly choose the sign of a_1 after sampling a_0 from the probability distribution above. Since this distribution is unbounded, we change variables to form a bounded function.

$$
\begin{aligned}
z &= \exp\left(-\frac{4\beta k}{N\pi} \cos^{-1} a_0\right) && e^{-\frac{4\beta k}{N}} < z < e^{\frac{4\beta k}{N}} \\
\Rightarrow \mathrm{d}P(z) &\propto \mathrm{d}z\, z^{-1} \exp\left(\frac{2\beta k}{N} \cos\left[\frac{N\pi}{4\beta k} \ln z\right]\right) && (1.21)
\end{aligned}
$$

If we further define $\theta = \frac{N\pi}{4\beta k} \ln z$, then we want to sample the distribution $P(\theta) \sim \exp(\frac{2\beta k}{N} \cos\theta)$ with $\theta \in (-\pi, 0)$.

While this approach is good for $SO(2)$ matrices, it is inefficient at large N because the factor $\frac{2\beta k}{N}$ increases with N and the algorithm was designed assuming that this factor is small. We can adapt the algorithm by sampling θ from an alternative gaussian distribution $R(\theta)$ and then accepting it with probability $P(\theta)/R(\theta)$.

$$
\begin{aligned}
R(\theta) &= \exp\left(\frac{2\beta k}{N}\left(1 - \frac{2}{\pi^2}\theta^2\right)\right) \\
\frac{P(\theta)}{R(\theta)} &= \exp\left(\frac{2\beta k}{N}\left(\cos\theta + \frac{2}{\pi^2}\theta^2 - 1\right)\right) && (1.22)
\end{aligned}
$$

This seems to have a much better acceptance rate than the original algorithm.

We can extend the heat bath algorithm to $SO(N)$ matrices using the Cabibbo-Marinari algorithm [6]. To do this, we construct matrices $a_k : k = 1, \ldots, N-1$ using submatrices $\alpha_k \in SO(2)$ to update the link $U \to U'$.

$$
\begin{aligned}
a_k &= \begin{pmatrix} 1 & & & & & \\ & \ddots & & & & \\ & & 1 & & & \\ & & & \alpha_k & & \\ & & & & 1 & \\ & & & & & \ddots \\ & & & & & & 1 \end{pmatrix} \\
U' &= a_{N-1} a_{N-2} \cdots a_1 U && (1.23)
\end{aligned}
$$

We update the link by constructing and applying each a_k one at a time. As we update the link, the heat bath algorithm isolates a 2×2 submatrix r_k in the matrix UV. To use the algorithm, we construct a 2×2 matrix r'_k proportional to an $SO(2)$ element such that

$$\begin{aligned} \mathrm{tr}(a_k UV) &\sim \mathrm{tr}(\alpha_k r_k) \\ &= \mathrm{tr}(\alpha_k r'_k) \end{aligned} \tag{1.24}$$

where we can define r'_k from r_k

$$r_k = \begin{pmatrix} A & B \\ C & D \end{pmatrix} \Rightarrow r'_k = \begin{pmatrix} \frac{A+D}{2} & \frac{B-C}{2} \\ \frac{C-B}{2} & \frac{A+D}{2} \end{pmatrix} \tag{1.25}$$

Once the lattice is in equilibrium, we want to reduce the correlation between individual measurements. To do this, we update the lattice several times between measurements so that the system can move through the configuration space. In practice, we take one measurement every ten updates.

1.4 Calculating masses

1.4.1 Correlation functions

For an operator ϕ projecting on to a particular physical state, we can calculate the correlation function $C(t)$ of operator values ϕ on spatial slices at times 0 and t. We can then extract the energies E_n of the state represented by ϕ by

$$\begin{aligned} C(t) = \frac{\langle \phi(t)\phi(0) \rangle}{\langle \phi(0)\phi(0) \rangle} &= \frac{\langle \Omega | \, \phi(t)\phi(0) \, | \Omega \rangle}{\langle \Omega | \, \phi(0)\phi(0) \, | \Omega \rangle} \\ &= \frac{\sum_n \langle \Omega | \, \phi(0) e^{-Ht} \, | n \rangle \, \langle n | \, \phi(0) \, | \Omega \rangle}{\sum_m \langle \Omega | \, \phi(0) \, | m \rangle \, \langle m | \, \phi(0) \, | \Omega \rangle} \\ &= \frac{\sum_n |\langle \Omega | \, \phi(0) \, | n \rangle|^2 e^{-E_n t}}{\sum_m |\langle \Omega | \, \phi(0) \, | m \rangle|^2} \end{aligned} \tag{1.26}$$

where $|\Omega\rangle$ is the vacuum state and $|n\rangle$ represents the state with energy E_n.

As we take $t \to \infty$, we then find that

$$\langle \phi(t)\phi(0) \rangle \xrightarrow[t \to \infty]{} c_0 e^{-E_0 t} \tag{1.27}$$

where E_0 is the mass of the lightest state and c_0 is some constant. Figure 1.2 shows examples of correlation functions $C(t)$ for $SO(6)$ glueball operators (which we describe in a later chapter) on a lattice with $\beta = 46.0$. In this figure, we can see that $\ln(C(t))$ varies linearly with t as we would expect from (1.27). For an operator ϕ projecting on to a physical state, we can estimate the energy E for the state by calculating correlation functions $\langle \phi(t+t')\phi(t') \rangle$ of operator values ϕ on spatial slices at times $t+t'$ and t'. If the lightest state is the vacuum, we use vacuum subtracted

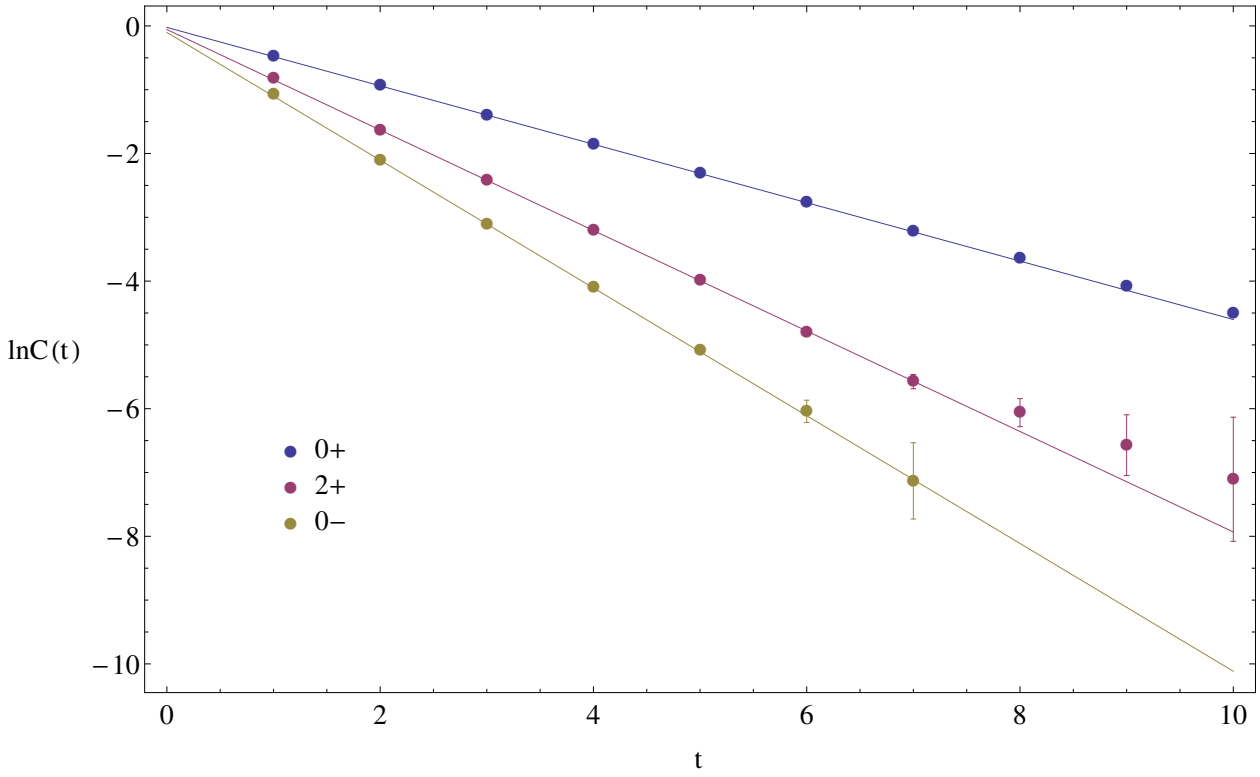

Figure 1.2: Correlation functions for $SO(6)$ glueball operators on a $36^2 44$ lattice with $\beta = 46.0$. We apply linear fits in regions where the errors are small in order to extract the glueball masses.

operators. If the lattice is finite with periodic boundary conditions, then there is an additional contribution from the 'back' of the torus. Summing this contribution leads to a hyperbolic cosine fit in t. While we always have this term in the numerical calculations, we write in this thesis the fit as an exponential in t for simplicity as though $L_t \to \infty$. We note that, in principle, we could use (1.26) to obtain the energies of excited states. However, fitting sums of exponentials is a badly conditioned problem, especially given statistical errors, so we need an alternative approach such as variational criteria.

1.4.2 Variational criteria

If we have multiple operators that project on to a particular state, we want to extend the above procedure so that we can maximise the projection and project on to excited states. To do this, we use variational criteria [2]. Suppose we have a set of n normalised operators $S = \{\phi_i : i = 1, \ldots, n\}$. We want to construct an operator Φ_1 that is a linear combination of operators from S and that maximises $C(a) = \langle \phi(a)\phi(0) \rangle$. This operator is the best estimate for the ground state operator from the set S, and $C(a)$ provides an estimate of the ground state mass. We can construct excited state operators iteratively. Suppose we have constructed new operators $\Phi_1, \ldots, \Phi_m$. Now construct

a basis of operators S_{m+1} from S that spans the $(n-m)$-dimensional subspace that is orthogonal to the subspace spanned by the new operators. Construct an operator Φ_{m+1} that both is a linear combination of operators from S_{m+1} and maximises $C(a) = \langle\phi(a)\phi(0)\rangle$. $C(a)$ then provides an estimate of the energy of the $m+1$ excited state. We can construct the Φ_i by considering the $N \times N$ correlation matrix $\mathbf{C}(t)$ by $C_{ij}(t) = \langle\phi_i(t)\phi_j(0)\rangle$. Let the eigenvectors of $\mathbf{C}^{-1}(0)\mathbf{C}(a)$ be $\{\mathbf{v}^i : i = 1, \ldots, n\}$. Then Φ_i is given by

$$\Phi_i = c_i \sum_{k=1}^{n} v_k^i \phi_k \tag{1.28}$$

for a constant c_i that normalises Φ_i.

Calculating the mass from a correlation function with a gap of one lattice spacing may not provide an accurate value. To improve on this, we consider the correlation functions $C_i(t) = \langle\Phi_i(t)\Phi_i(0)\rangle$. Within ranges of values $t \in (t_1, t_2)$, we fit a local exponential to correlation values $C_i(t)$ to provide primary mass estimates. We set $t_1 = 0$ initially, and then increase t_1 until we reach the lowest t_1 where $\bar{\chi}^2_{\text{dof}}$ is reasonable, since statistical errors grow with t_1. We usually select t_2 large so that the exponential fit is over many values. Simultaneously, we obtain secondary mass estimates for each correlation function by using the values of $C_i(t)/C_i(0)$ and the procedure in the previous section and looking for a plateau in these values. We obtain our final estimate by selecting a primary estimate from an exponential fit with a low $\bar{\chi}^2_{\text{dof}}$ that also agrees with our secondary estimate. We note that statistical errors dominate correlation functions at large t where the exponential has decayed significantly as we can see in Figure 1.2. Hence, we can only obtain mass estimates over a limited range of correlation function values at smaller t.

1.4.3 Jackknife errors

We want to calculate the errors of the mass measurements [7]. Suppose we have a data set for an observable O with N_m measurements $\{O_1, \ldots, O_{N_m}\}$. Then our estimate for O from all data is

$$\hat{O} = \frac{1}{N_m} \sum_{i=1}^{N_m} O_i \tag{1.29}$$

We can divide the data into N_b equally sized data bins, labelled $B_1, \ldots, B_{N_b}$, with N_m/N_b measurements in each bin. Then we can construct N_b new jackknife bins, labelled $B'_1, \ldots, B'_{N_b}$, where the jackknife bin B'_n includes all data except those in bin B_n. Let the estimate for O from jackknife bin B'_n be $\hat{O}'_n$. Then define the variance to be

$$\sigma_{\hat{O}}^2 = \frac{N_b - 1}{N_b} \sum_{n=1}^{N_b} (\hat{O}'_n - \hat{O})^2 \tag{1.30}$$

so that our estimate of the standard deviation of O is the square root of this variance. To use this method, it is important that each of the original bins B_n are reasonably large so that the observable estimates from each bin $\hat{O}'_n$ are approximately uncorrelated.

1.4.4 Goodness of fit

We will later use data extrapolations to calculate continuum or infinite volume limits. To judge the goodness of fit, we use the reduced chi-squared statistic $\bar{\chi}^2_{\text{dof}}$, which is the chi-squared divided by the degrees of freedom. Let $\{(O_n, \sigma_n)\}$ be a set of N values $\{O_n\}$ with corresponding errors $\{\sigma_n\}$. We wish to fit the data with a model with n parameters, which predicts that E_n is the expected value of O_n. Then the number of degrees of freedom is $N - n$ and the $\bar{\chi}^2_{\text{dof}}$ is

$$\bar{\chi}^2_{\text{dof}} = \frac{1}{N - n} \sum_{i=1}^{N} \frac{(O_n - E_n)^2}{\sigma_n^2} \tag{1.31}$$

In general, a $\bar{\chi}^2_{\text{dof}} \approx 1$ indicates that the data and model values agree with the data errors so that the model is good whereas a $\bar{\chi}^2_{\text{dof}} \gg 1$ indicates that the data and model values disagree so that the model is poor.

Chapter 2

Equivalences between $SO(N)$ and $SU(N)$ gauge theories

In this chapter, we consider the equivalences between $SO(N)$ and $SU(N)$ gauge theories. We start by considering specific Lie algebra equivalences before going on to consider the large-N limit of $SO(N)$ and $SU(N)$ gauge theories. We recall 't Hooft's argument relating $SO(N)$ and $SU(N)$ gauge theories to their respective large-N limits and then go on to look at the large-N orbifold equivalence that holds between $SO(N \to \infty)$ and $SU(N \to \infty)$ gauge theories. We discuss the fermion sign problem in $SU(N)$ gauge theories before concluding with a possible approach to this problem using $SO(N)$ gauge theories.

2.1 Lie algebra equivalences

2.1.1 $SO(4) \sim SU(2) \times SU(2)$

$SO(4)$ and $SU(2) \times SU(2)$ share the same Lie algebra. We can see this by defining a generator basis $\{t_{ij}\}$ for $SO(4)$, for $i < j \in \{1, \ldots, 4\}$.

$$[t_{ij}]_{kl} = i\left(\delta_{ik}\delta_{jl} - \delta_{il}\delta_{jk}\right) \tag{2.1}$$

We can partition these generators into two groups $\{J_i, K_i\}$ with $i \in \{1, 2, 3\}$ and define new generators $\{\tilde{J}_i, \tilde{K}_i\}$.

$$J_i = \frac{1}{2}\epsilon_{ijk}t_{jk} \qquad K_i = t_{i4}$$
$$\tilde{J}_i = -\frac{1}{2}(J_i + K_i) \qquad \tilde{K}_i = -\frac{1}{2}(J_i - K_i) \tag{2.2}$$

These new generators satisfy

$$[\tilde{J}_i, \tilde{J}_j] = i\epsilon_{ijk}\tilde{J}_k \qquad [\tilde{K}_i, \tilde{K}_j] = i\epsilon_{ijk}\tilde{K}_k \qquad [\tilde{J}_i, \tilde{K}_j] = 0 \tag{2.3}$$

Hence, the generators $\{\tilde{J}_i, \tilde{K}_i\}$ independently satisfy the $SU(2)$ Lie algebras and together form a direct sum of two $SU(2)$ Lie algebras, which verifies our initial claim. In fact, $SU(2) \times SU(2)$ forms a double cover of $SO(4)$. Assuming that the global properties of the two groups do not affect the dynamics of their gauge theories, we will consider if they share similar physical properties.

2.1.2 $SO(6) \sim SU(4)$

We recall that, in $SU(4)$,

$$4 \otimes 4 = 6 \oplus 10 \tag{2.4}$$

where the 6 corresponds to the $k = 2$ antisymmetric representation and maps to the fundamental 6 of $SO(6)$ [8]. To convert quantities in terms of the $SU(4)$ fundamental string tension to the $SU(4)$ $k = 2A$ string tension, we use the ratio of the $SU(4)$ $k = 2A$ and fundamental string tensions in $D = 2 + 1$ [9]

$$\left.\frac{\sigma_{2A}}{\sigma_f}\right|_{SU(4)} = 1.355(9) \tag{2.5}$$

Hence, assuming that the global properties of the two groups do not affect the dynamics of their gauge theories, we will test if they share similar physical properties.

2.1.3 $SO(3) \sim SU(2)$

We know that $SU(2)$ forms a double cover of $SO(3)$, where the $SO(3)$ fundamental representation is equivalent to the $SU(2)$ adjoint representation, so again we might ask if they share similar physical properties. However, there are two issues with $SO(3)$ lattice calculations. Firstly, $SO(3)$ fundamental flux tubes correspond to $SU(2)$ adjoint flux tubes. However, we know that these $SU(2)$ adjoint flux tubes are not well-defined as they can decay into glueballs, so we might expect a similar problem in $SO(3)$ gauge theories [10]. This agrees with our knowledge that $SO(3)$ lacks a non-trivial centre such as the $\mathbb{Z}_2$ centre in $SO(2\tilde{N})$ gauge theories that protects flux loops from

mixing with glueball operators. Secondly, previous calculations in $SO(3)$ gauge theories indicate that the bulk transition occurs at small lattice spacing so that we would need much larger volumes to be in the weak coupling region [3]. It is for these two reasons that we will consider $SO(3)$ gauge theories in future papers and not in this thesis.

2.2 't Hooft's $1/N$ argument

QCD lacks a natural expansion parameter since the coupling is $\mathcal{O}(1)$ at low energies. This led 't Hooft to suggest another parameter, $1/N$, where N is the number of colours in the gauge group of the theory. This motivates us to ask what is the scale of the corrections from QCD to the large-N limit: just how close is $N = 3$ to $N \to \infty$?

2.2.1 't Hooft coupling

A pure gauge theory has a Lagrangian given by

$$\begin{aligned} \mathcal{L} &= \frac{1}{2g^2}\mathrm{tr}(F_{\mu\nu}^2) \\ &= \frac{N}{\lambda}\left(\frac{1}{2}\mathrm{tr}(F_{\mu\nu}^2)\right) \end{aligned} \tag{2.6}$$

$$F_{\mu\nu}(x) = \partial_\mu A_\nu(x) - \partial_\nu A_\mu(x) + i\left[A_\mu(x), A_\nu(x)\right] \tag{2.7}$$

where g is the conventional coupling, $F_{\mu\nu}$ is the field strength tensor, and $\lambda = g^2 N$. The beta function $\beta(g)$ for a pure gauge theory is [11]

$$\beta(g) \equiv \mu\frac{dg}{d\mu} = -\frac{11N}{3}\frac{g^3}{16\pi^2} + \mathcal{O}(g^5) \tag{2.8}$$

This shows how the conventional coupling g scales with N

$$g^2(\Lambda) \approx \frac{24\pi^2}{11N\ln(\Lambda/\Lambda_{\mathrm{QCD}})} \sim \frac{1}{N} \tag{2.9}$$

indicating that we can remove the N-dependence in the beta function by rescaling the coupling to the 't Hooft coupling [12, 13] defined by

$$\lambda = g^2 N \tag{2.10}$$

This fixes the scale parameter of strong interactions Λ_{QCD}. Since λ is dimensionful in $D = 2 + 1$, fixing λ also fixes the length scale. Hence, taking the limit $N \to \infty$ while fixing λ is equivalent to

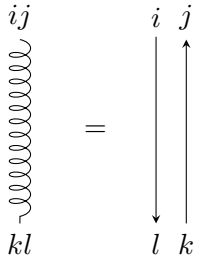

Figure 2.1: Double line representation for an $SU(N)$ gauge propagator $\left\langle [A_\mu(x)]^i{}_j [A_\nu(y)]^k{}_l \right\rangle$.

taking $N \to \infty$ while fixing the length (or mass) scale.

2.2.2 $SU(N)$ gauge theories

We first review 't Hooft's planar diagram argument for $SU(N)$ gauge theories [12,14] before applying it to $SO(N)$ gauge theories. We can express the gauge field A_μ in terms of the Lie algebra generators t^a for the gauge group $SU(N)$.

$$[A_\mu(x)]^i{}_j = \sum_a A^a_\mu(x)[t^a]^i{}_j \tag{2.11}$$

where a, b label the generators and $i, j, \ldots$ label the matrix indices. The generators t^a are traceless Hermitian matrices and we can normalise them such that $\mathrm{tr}(t^a t^b) = \frac{1}{2}\delta^{ab}$.

Now consider a gauge field propagator $\langle A_\mu(x) A_\nu(y) \rangle$ in Euclidean space and expand using (2.11).

$$\begin{aligned}
\left\langle [A_\mu(x)]^i{}_j [A_\nu(y)]^k{}_l \right\rangle &= \sum_{a,b} \left\langle A^a_\mu(x) A^b_\nu(y) \right\rangle [t^a]^i{}_j [t^b]^k{}_l \\
&= \sum_{a,b} \delta^{ab} D_{\mu\nu}(x-y) [t^a]^i{}_j [t^b]^k{}_l \\
&= \frac{1}{2}\left(\delta^i{}_l \delta^k{}_j - \frac{1}{N} \delta^i{}_j \delta^k{}_l \right) D_{\mu\nu}(x-y)
\end{aligned} \tag{2.12}$$

where $D_{\mu\nu}(x-y)$ is the propagator for a massless vector field. We can drop the $1/N$ term when we take the large-N limit for reasons that we will discuss soon so that

$$\left\langle [A_\mu(x)]^i{}_j [A_\nu(y)]^k{}_l \right\rangle \propto \delta^i{}_l \delta^k{}_j \tag{2.13}$$

We can represent this propagator diagrammatically as a double line, as we display in Figure 2.1. Each of the two index lines forming the double line represents a Kronecker delta and has an orientation that we indicate by an arrow pointing from a raised matrix index to a lowered matrix index.

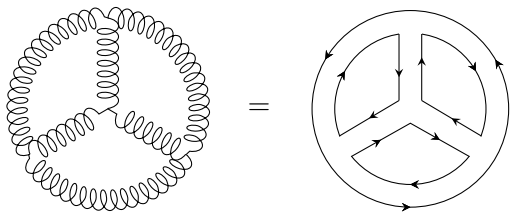

Figure 2.2: Converting a Feynman diagram into an $SU(N)$ double line diagram. This double line diagram is planar and has $(F, E, V) = (4, 6, 4)$. Hence, $\chi = 2$ and the diagram is proportional to N^2.

We now consider gluonic Feynman diagrams of the gauge theory. We can convert Feynman diagrams to double line graphs where we convert all gluon propagators to double lines with arrows, require that the arrows point in different directions on the two index lines that make a double line, and specify that the arrow flow must agree on the two index lines that meet at a vertex. Since there are no external lines, all index lines must close to form an index loop, and we can consider an index loop as the perimeter of a polygon.

We can identify the edge of one polygon with the edge of another if they are both parts of the same double line. Then the double line picture describes a polygonisation of a surface. Furthermore, the arrows orient each polygon and, since the arrows point in different directions on the edges of neighbouring polygons, this orients neighbouring polygons and so orients the entire surface. We display an example of a polygonisation in Figure 2.2.

We can count the number of faces F, edges E, and vertices V in the surface. Consider the $SU(N)$ Lagrangian in (2.6). We can see that every face is an index loop and so carries a factor of N, every edge corresponds to a propagator and so carries a factor of λ/N, and every vertex corresponds to a gluonic vertex and so carries a factor of N/λ. Hence, each double line graph corresponds to a factor

$$\lambda^{E-V} N^{F-E+V} \tag{2.14}$$

Here, we can see that this factor has a term that is a power of $\lambda = g^2 N$ and a second term that only depends on N. This indicates that we can compare the N-dependence of diagrams in different $SU(N)$ theories if we hold the 't Hooft coupling $\lambda = g^2 N$ constant. We can express the N-dependent term in (2.14) in terms of the Euler characteristic $\chi \equiv F - E + V$.

$$N^{F-E+V} \equiv N^{\chi} \tag{2.15}$$

We can also compute the Euler characteristic in a different way. All two-dimensional oriented

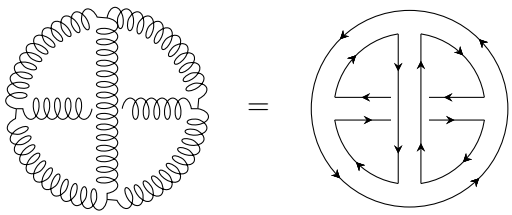

Figure 2.3: An example of a non-planar diagram in an $SU(N)$ gauge theory, which has $(F, E, V) = (2, 6, 4)$, or we could view it as $H = 1$. Hence, $\chi = 0$ and the diagram is proportional to N^0.

surfaces are topologically equivalent to a sphere with a number of holes cut out of it and handles attached to it [14]. We can count the number of holes B (for boundary) and handles H in the surface. Then we can express the Euler characteristic as $\chi = 2 - 2H - B$. However, since we are only considering gauge theories and all gluonic propagators correspond to a double line, it is not possible to construct a hole without also filling it with a new face. Hence, $B = 0$, and the Euler characteristic for double line graphs for gauge theories is $\chi = 2 - 2H$.

We earlier dropped the $\mathcal{O}(1/N)$ term in (2.12). This term corresponds to a $U(1)$ ghost gauge field [13,14] that cancels out the $U(1)$ gauge field in a $U(N)$ gauge theory to form an $SU(N)$ gauge theory. The $U(1)$ ghost gauge field completely decouples from the $SU(N)$ gauge bosons since the $U(1)$ generator commutes with all the $SU(N)$ generators. Hence, in a theory with only gauge fields, there are no further $\mathcal{O}(1/N)$ corrections from the $U(1)$ ghost gauge field. In a theory with quark fields, the leading correction diagrams with a $U(1)$ ghost gauge field would be $\mathcal{O}(1/N^2)$ with a factor of $1/N$ from the propagator and another from the explicit factor in (2.12). Hence, we can ignore this term when considering the leading correction diagrams.

Hence, the leading order double line graph is proportional to N^2 and we can form them from planar diagrams without handles. The first order correction corresponds to a planar diagram with a handle attached and is proportional to N^0. Hence, first order correction graphs here are $\mathcal{O}(1/N^2)$ when we compare them to the leading order planar diagrams. We display an example of a non-planar diagram in Figure 2.3.

Putting this all together, we expect that the physics of $SU(N)$ gauge theories has a common large-N limit with $\mathcal{O}(1/N^2)$ corrections if we keep the 't Hooft coupling $\lambda = g^2 N$ constant.

2.2.3 $SO(N)$ gauge theories

Having considered how 't Hooft's planar diagram argument applies to $SU(N)$ gauge theories, we now see how to adapt it to $SO(N)$ gauge theories [15]. We can again express the gauge field A_μ in

terms of the Lie algebra generators t^{ab} for the gauge group $SO(N)$.

$$[A_\mu(x)]^i{}_j = \sum_{a<b} A^{ab}_\mu(x)[t^{ab}]^i{}_j \tag{2.16}$$

where $a, b, \ldots$ label the generators and $i, j, \ldots$ label the matrix indices.

The generators t^{ab} are antisymmetric matrices and we can normalise them such that $\mathrm{tr}(t^{ab}t^{cd}) = \frac{1}{2}\delta^{ac}\delta^{bd}$. We can construct an explicit generator basis satisfying this normalisation condition for the $\frac{1}{2}N(N-1)$ generators t^{ab} for $a < b \in \{1, 2, \ldots, N\}$.

$$[t^{ab}]^i{}_j = \frac{i}{2}\left(\delta^{ai}\delta^b{}_j - \delta^a{}_j\delta^{bi}\right) \tag{2.17}$$

Then we can write the gauge field propagator $\langle A_\mu(x)A_\nu(y)\rangle$ in Euclidean space as

$$\begin{aligned}
\left\langle [A_\mu(x)]^i{}_j[A_\nu(y)]^k{}_l \right\rangle &= \sum_{a<b,\, c<d} \left\langle A^{ab}_\mu(x)A^{cd}_\nu(y)\right\rangle [t^{ab}]^i{}_j[t^{cd}]^k{}_l \\
&= \sum_{a<b,\, c<d} \delta^{ac}\delta^{bd}D_{\mu\nu}(x-y)[t^{ab}]^i{}_j[t^{cd}]^k{}_l \\
&= D_{\mu\nu}(x-y)\sum_{a<b}[t^{ab}]^i{}_j[t^{ab}]^k{}_l \\
&= D_{\mu\nu}(x-y)\sum_{a<b}\frac{i}{2}\left(\delta^{ai}\delta^b{}_j - \delta^a{}_j\delta^{bi}\right)\frac{i}{2}\left(\delta^{ak}\delta^b{}_l - \delta^a{}_l\delta^{bk}\right) \\
&= \frac{1}{4}\left(\delta^i{}_l\delta^k{}_j - \delta^{ik}\delta_{lj}\right)D_{\mu\nu}(x-y)
\end{aligned} \tag{2.18}$$

where $D_{\mu\nu}(x-y)$ is the propagator for a massless vector field. Here, we see that

$$\left\langle [A_\mu(x)]^i{}_j[A_\nu(y)]^k{}_l \right\rangle \propto \delta^i{}_l\delta^k{}_j - \delta^{ik}\delta_{lj} \tag{2.19}$$

The first term of the $SO(N)$ propagator has the same form as that of the $SU(N)$ propagator, which we call a straight propagator. However, there is also a new second term, which we call a twisted propagator. This combines raised or lowered matrix indices.

We can represent this propagator as a sum of two double lines as with the $SU(N)$ propagator. Each of the two index lines that form a double line represents a Kronecker delta and has an orientation that we can indicate by an arrow pointing from a raised matrix index to a lowered matrix index. However, while the double line description of the straight propagator has the same form as that of the $SU(N)$ propagator, the double line description of the twisted propagator changes the arrow flow for both index lines. We display this double line description in Figure 2.4.

As with $SU(N)$ gauge theories, these double line graphs represent polygons on a surface and we

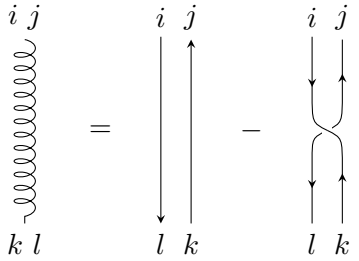

Figure 2.4: Double line description for $SO(N)$ gauge propagator. On the right hand side, the first term is the straight propagator linking $i \to l$, $k \to j$ while the second term is the twisted propagator linking i and k, j and l.

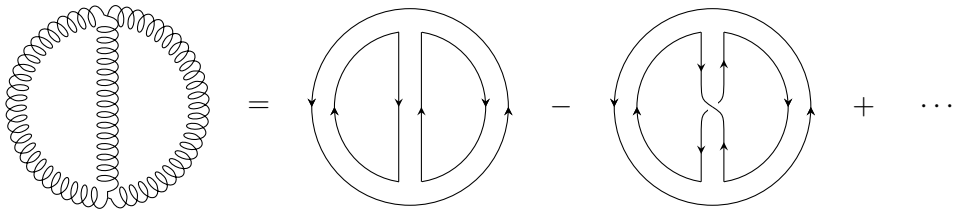

Figure 2.5: Converting a Feynman diagram into an $SO(N)$ double line diagram. The first double line diagram is planar and has $(F, E, V) = (3, 3, 2)$ so that $\chi = 2$ and the diagram is proportional to N^2. The second double line diagram is non-planar and has $(F, E, V) = (2, 3, 2)$ so that $\chi = 1$ and the diagram is proportional to N^1. There are further terms involving twisted propagators.

preserve the directions of arrows along edges and vertices with the exception of edges constructed by twisted propagators. This introduces new non-oriented surfaces. By holding the 't Hooft coupling constant, we can again classify the surfaces by the Euler characteristic and correspond each graph to a power of N.

As we would expect, the leading order double line graph is a planar diagram without twisted propagators and is proportional to N^2. However, the first order correction is not $\mathcal{O}(N^0)$. Consider a planar diagram. Now change a straight propagator to a twisted propagator. This change does not alter the number of vertices V or edges E. However, while the straight propagator formed the edge between two faces, the twisted propagator now represents a twist in one face since we could untwist the propagator to reveal the unravelled face. Hence the number of faces F for a diagram with one twisted propagator while otherwise planar is one less than the corresponding planar diagram. Hence, the Euler characteristic is one less and so this diagram is proportional to N^1. Hence, first order correction graphs here are $\mathcal{O}(1/N)$ when we compare them to the leading order planar diagrams. We display examples of these diagrams in Figure 2.5.

Putting this all together, we expect that the physics of $SO(N)$ gauge theories has a common large-N limit with $\mathcal{O}(1/N)$ corrections if we keep the 't Hooft coupling $\lambda = g^2 N$ constant.

2.3 Large-N orbifold equivalence

We know that $SO(N)$ and $SU(N)$ pure gauge theories have a common large-N limit in their common sector of states [16]. The large-N orbifold equivalence [17–19] goes further to show that we can obtain $SU(\tilde{N})$ QCD from an $SO(2\tilde{N})$ QCD-like theory under certain conditions.

The Lagrangian for a QCD-like theory with gauge group G and N_f flavours of Dirac fermions in Euclidean space is

$$\mathcal{L} = \frac{1}{2g_G^2}\mathrm{tr}(F_{\mu\nu}^G)^2 + \sum_{a=1}^{N_f} \bar{q}_a^G(\gamma^\mu D_\mu^G + m_q + \mu\gamma_0)q_a^G \tag{2.20}$$

where g_G is the coupling, $F_{\mu\nu}^G$ is the field strength, $D_\mu^G = \partial_\mu + iA_\mu^G$, q_a^G is a Dirac fermion in the fundamental representation, m_q is the quark mass, and μ is the quark chemical potential.

We can apply an orbifold projection [20–22] on a parent $SO(2\tilde{N})$ QCD-like theory to obtain a child $SU(\tilde{N})$ QCD theory. To do this, we identify a discrete subgroup of the symmetry group of the parent theory and then set to zero all non-invariant degrees of freedom under the symmetry subgroup, giving us a child theory.

In this case, the parent $SO(2\tilde{N})$ QCD-like theory is

$$\mathcal{L}_{SO(2\tilde{N})} = \frac{1}{2g_{SO(2\tilde{N})}^2}\mathrm{tr}(F_{\mu\nu})^2 + \sum_{a=1}^{N_f} \bar{q}_a(\gamma^\mu D_\mu + m_q + \mu\gamma_0)q_a \tag{2.21}$$

The discrete subgroup of the symmetry group of this parent theory is $\mathbb{Z}_2 \subset SO(2\tilde{N}) \times U(1)_B$. To define the orbifold projection, consider $J = i\sigma_2 \otimes \mathbf{1}_{\tilde{N}} \in SO(2\tilde{N})$, where $\mathbf{1}_{\tilde{N}}$ is an $\tilde{N} \times \tilde{N}$ identity matrix, and $\omega = e^{i\pi/2} \in U(1)_B$. The action of J on A_μ and ω on q_a is

$$\begin{aligned} A_\mu &\to JA_\mu J^T \\ q_a &\to -\omega J q_a \end{aligned} \tag{2.22}$$

and generates a $\mathbb{Z}_2$ subgroup of $SO(2\tilde{N}) \times U(1)_B$. We can write the matrix field A_μ in $\tilde{N} \times \tilde{N}$ blocks

$$A_\mu = i\begin{pmatrix} A_\mu^A + B_\mu^A & C_\mu^A - D_\mu^S \\ C_\mu^A + D_\mu^S & A_\mu^A - B_\mu^A \end{pmatrix} \tag{2.23}$$

where the superscript A/S represents antisymmetric/symmetric matrices. Under the $\mathbb{Z}_2$ symmetry, A_μ^A, D_μ^S are even while B_μ^A, C_μ^A are odd. Under the orbifold projection, we set to zero non-invariant degrees of freedom so that $B_\mu^A = C_\mu^A = 0$. Hence the projected matrix gauge field A_μ^{proj} is

$$A_\mu^{\text{proj}} = i \begin{pmatrix} A_\mu^A & -D_\mu^S \\ D_\mu^S & A_\mu^A \end{pmatrix} \tag{2.24}$$

Consider the following unitary matrix P and use it to diagonalise A_μ^{proj}

$$P = \frac{1}{\sqrt{2}} \begin{pmatrix} \mathbf{1}_{\tilde{N}} & i\mathbf{1}_{\tilde{N}} \\ \mathbf{1}_{\tilde{N}} & -i\mathbf{1}_{\tilde{N}} \end{pmatrix} \qquad \Rightarrow \qquad P A_\mu^{\text{proj}} P^{-1} = \begin{pmatrix} -\mathcal{A}_\mu^T & 0 \\ 0 & \mathcal{A}_\mu \end{pmatrix} \tag{2.25}$$

where $\mathcal{A}_\mu = D_\mu^S + iA_\mu^A$ and is an $U(\tilde{N})$ gauge field. The difference between $U(N)$ and $SU(N)$ is $\mathcal{O}(1/N^2)$ so that the gauge terms converge in the large-N limit. Hence, the gauge component of the new child theory due the orbifold projection $\mathcal{L}_{\text{gauge}}^{\text{proj}}$ is

$$\mathcal{L}_{\text{gauge}}^{\text{proj}} = \frac{2}{2g_{SO(2\tilde{N})}^2} \text{tr}(\mathcal{F}_{\mu\nu})^2 \tag{2.26}$$

where $\mathcal{F}_{\mu\nu}$ is the $SU(\tilde{N})$ field strength tensor in terms of the $SU(\tilde{N})$ gauge field $\mathcal{A}_\mu$. We then take

$$\mathcal{L}_{SO(2\tilde{N})} \to 2\mathcal{L}_{SU(\tilde{N})} \tag{2.27}$$

This factor of two is necessary to match the ground state energies per degree of freedom between the two theories [23, 24] since there are twice as many degrees of freedom in the parent theory than the child theory.

Consider the action of the $\mathbb{Z}_2$ symmetry and P on q_a.

$$P q_a \equiv \begin{pmatrix} \lambda_a^+ \\ \lambda_a^- \end{pmatrix} \to \begin{pmatrix} -\lambda_a^+ \\ \lambda_a^- \end{pmatrix} \tag{2.28}$$

Under the orbifold projection, we set to zero non-invariant degrees of freedom so that $\lambda_a^+ = 0$.

We then conclude that the resulting child theory from this large-N orbifold projection is

$$\mathcal{L}_{SU(\tilde{N})} = \frac{1}{2g_{SU(\tilde{N})}^2} \text{tr}(\mathcal{F}_{\mu\nu})^2 + \sum_{a=1}^{N_f} \bar{\psi}_a (\gamma^\mu \mathcal{D}_\mu + m_q + \mu\gamma_0)\psi_a \tag{2.29}$$

where $\mathcal{A}_\mu = D_\mu^S + A_\mu^A$, $\psi_a = \lambda_a^-$, $\mathcal{D}_\mu = \partial_\mu + i\mathcal{A}_\mu$, and we relate the couplings of the two gauge theories by

$$g_{SU(\tilde{N})}^2 = g_{SO(2\tilde{N})}^2 \tag{2.30}$$

The orbifold projection symmetries link the correlators of particular operators in the two theories in the large-N limit. Define neutral operators to be operators that are invariant under the projection symmetry. Then, colour singlet operators in an $SO(2\tilde{N})$ theory are neutral and the

projection symmetry maps them to $C = +$ operators in an $SU(\tilde{N})$ theory.

For this orbifold equivalence to hold non-perturbatively, the projection symmetry must not spontaneously break. When $\mu \geq m_\pi/2$, baryonic pion condensation breaks down the symmetry $U(1)_B \to \mathbb{Z}_2$, breaking the equivalence. We can add a deformation term to prevent this condensation and protect the projection symmetry [20, 21]. One such choice of deformation term is

$$\mathcal{L}_{SO(2\tilde{N})} \to \mathcal{L}_{SO(2\tilde{N})} + \frac{c^2}{\Lambda^2} \sum_{a,b} S^\dagger_{ab} S_{ab} \tag{2.31}$$

where $S_{ab} = q_a^T C\gamma^5 q_b$ and $C = \gamma_0\gamma_2$ is the charge conjugation matrix.

2.4 QCD fermion sign problem

A reason to consider the physics of $SO(N)$ gauge theories is the fermion sign problem in $SU(N)$ lattice QCD [7]. In a gauge theory at zero chemical potential, the Euclidean massless Dirac operator $\not{D}$ has the property that it is γ_5-Hermitian.

$$\begin{aligned} \not{D} &= \gamma_\mu(\partial_\mu + iA_\mu) \\ \not{D}^\dagger\gamma_5 &= \gamma_5\not{D} \end{aligned} \tag{2.32}$$

Now we consider the $SU(N)$ Dirac operator $D_{SU(N)}(\mu)$ for a quark of mass m at finite chemical potential μ.

$$\begin{aligned} D_{SU(N)}(\mu) &= \not{D}_{SU(N)} + m + \mu\gamma_0 \\ \Rightarrow \gamma_5 D_{SU(N)}(\mu) &= \gamma_5\not{D}_{SU(N)} + m\gamma_5 + \mu\gamma_5\gamma_0 \\ &= (\not{D}^\dagger_{SU(N)} + m - \mu\gamma_0)\gamma_5 \\ &= D^\dagger_{SU(N)}(-\mu^*)\gamma_5 \end{aligned} \tag{2.33}$$

Hence, if we evaluate the determinant of both sides, we find that

$$\det\left(D_{SU(N)}(\mu)\right) = \det\left(D_{SU(N)}(-\mu^*)\right)^* \tag{2.34}$$

This shows that the $SU(N)$ fermion determinant $\det\left(D_{SU(N)}(\mu)\right)$ is complex for real, non-zero μ. In lattice QCD, the fermion determinant acts as a probability weight in importance sampling. However, if it turns complex, it is impossible to use it as a probability weight and hence lattice calculations are impossible. This motivates us to consider equivalences with alternative gauge theories.

Consider now the $SO(2\tilde{N})$ Dirac operator $D_{SO(2\tilde{N})}(\mu)$ for a quark of mass m at finite chemical potential μ [21, 23].

$$\begin{aligned} & D_{SO(2\tilde{N})}(\mu) = \not{D} + m + \mu\gamma_0 \\ \Rightarrow \qquad & (C\gamma_5)D_{SO(2\tilde{N})}(\mu)(C\gamma_5)^{-1} = D^*_{SO(2\tilde{N})}(\mu) \end{aligned} \tag{2.35}$$

where we can consider an alternative conjugacy relation since the fermions are in a real representation. This means that, if ψ satisfies $D\psi = \lambda\psi$, then

$$D_{SO(2\tilde{N})}(\mu)(\gamma_5 C^{-1}\psi^*) = \lambda^*(\gamma_5 C^{-1}\psi^*) \tag{2.36}$$

showing that ψ and $\gamma_5 C^{-1}\psi^*$ are orthogonal. Hence, $D_{SO(2\tilde{N})}(\mu)$ has pairs of eigenvalues (λ, λ^*) so that $\det(D_{SO(2\tilde{N})}(\mu))$ is real and positive-definite, and we can use $\det(D_{SO(2\tilde{N})}(\mu))$ as a probability weight. Hence, there is no sign problem in the $SO(2\tilde{N})$ gauge theory.

2.5 Moving between $SU(N)$ and $SO(N)$ gauge theories

We can combine the ideas from 't Hooft's large-N argument and the large-N orbifold equivalence to suggest a route between $SU(N)$ and $SO(N)$ gauge theories. We know that finite $SU(N)$ gauge theory has $\mathcal{O}(1/N^2)$ corrections to its large-N limit $SU(N \to \infty)$ and similarly that finite $SO(N)$ gauge theory has $\mathcal{O}(1/N)$ corrections to its large-N limit $SO(N \to \infty)$, if we hold the 't Hooft coupling g^2N constant in both cases. Meanwhile, we suspect that the large-N orbifold equivalence leads to equivalent non-perturbative physics between $SU(\tilde{N} \to \infty)$ and $SO(2\tilde{N} \to \infty)$ if we hold $g^2_{SO(2\tilde{N})} = g^2_{SU(\tilde{N})}$. We summarise this process of moving between $SU(\tilde{N})$ and $SO(2\tilde{N})$ gauge theories in Figure 2.6.

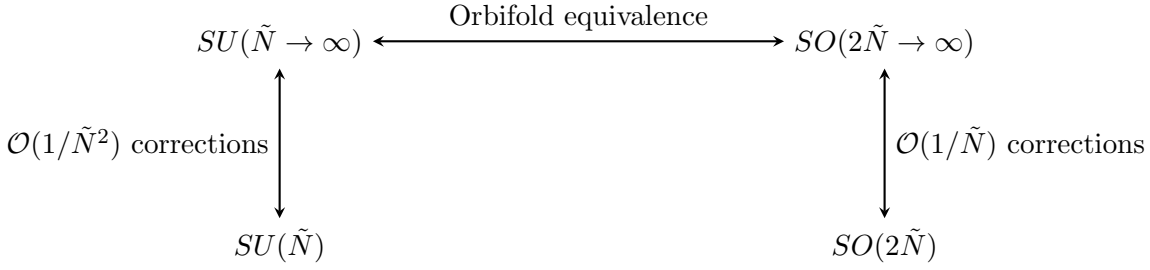

Figure 2.6: Moving between $SU(\tilde{N})$ and $SO(2\tilde{N})$ gauge theories

So if $SU(3)$ is close to $SU(N \to \infty)$ and, for example, $SO(6)$ turns out to be close to $SO(\tilde{N} \to \infty)$, we can imagine doing calculations in the $SO(6)$ theory in order to obtain a good approximation to the physics of $SU(3)$ QCD.

Chapter 3

String tension

In this chapter, we calculate the string tensions of $SO(N)$ gauge theories in $2+1$ dimensions. We start by constructing string tension operators that project well on to the states we are investigating before looking at string tension models. We move on to calculating $SO(N)$ continuum limits for string tensions, which we extrapolate to the large-N limit. We finally compare $SO(N)$ and $SU(N)$ string tensions between group equivalences.

3.1 String tension operators

3.1.1 Polyakov loops

We can calculate the string tension for a gauge theory by considering static charges q and $\bar{q}$ at a distance R apart and the flux tube that joins them together. A gauge invariant operator that projects on to this $q\bar{q}$ state is

$$\phi(t) = \bar{q}(0) \left(\prod U_\mu \right) q(R) \tag{3.1}$$

where we orient the two charges so that they are separated in the spatial μ direction and the product of lattice links $\prod U_\mu$ is the shortest linear path between them.

We can adapt this operator by imagining that we pull the charges apart until they travel around the spatial torus, meet, and annihilate. This leaves behind a non-contractible pure gauge flux loop that winds around the torus. The operator that describes this flux loop is the Polyakov loop. We can construct the Polyakov loop out of link variables

$$\phi_y(x,t) = \mathrm{tr} \prod_{m=1}^{L_s} U_y(x, y + m\hat{y}, t) \tag{3.2}$$

where, in this case, the Polyakov loop winds around the spatial torus in the y-direction.

We can set all the Polyakov loop operators to have zero momentum $p = 0$ by requiring the operators to be translationally invariant. We do this by summing all Polyakov loops starting from points in the orthogonal spatial direction to the direction in which the Polyakov loop winds around. Hence, on a spatial lattice, we choose the normalised Polyakov loop operator to be

$$\phi_y(t) = \frac{1}{L_s^2} \sum_{x=1}^{L_s} \sum_{y=1}^{L_s} \mathrm{tr} \prod_{m=1}^{L_s} U_y(x, y + m\hat{y}, t) \tag{3.3}$$

where, in this case, the operator $\phi_y(t)$ projects on to the Polyakov loop winding in the y-direction. We can similarly define an operator $\phi_x(t)$ winding in the x-direction. We note that we sum over both x and y, so that we can generalise this expression to operators defined on blocking levels, as we go on to explain.

3.1.2 Blocking

We want the operators that we use to project on to the lightest states. However, all the operators we have defined are loops of transverse size $\mathcal{O}(a)$, so they are ultraviolet and they will have an almost equal projection on to all states with any particular quantum numbers. Furthermore, the number of excited states increases as $a \to 0$. Hence, the normalised projection of these operators on to the lightest states decreases as $a \to 0$. This is a problem since we want to calculate the energy of lightest states at lattice spacings close to the continuum limit. We might attempt to solve this problem by considering values at larger t where the lightest states dominate. However, statistical noise also increases at larger t making it significantly more difficult to extract accurate masses.

We can solve this problem by constructing operators that are larger over physical length scales while also being smooth. To do this, we apply an iterative blocking procedure [25,26] that generates larger blocked links that we can use to construct larger operators. At blocking level 0, we define the links $U^0(x)$ to be the standard lattice links $U^0_\mu(x) = U_\mu(x)$. At blocking level $N+1$, we define the links $U^{N+1}(x)$ from the blocked links $U^N(x)$ at blocking level N through the following method. Consider a blocked lattice at level N with sites are $2^N a$ apart and a blocked link $U^N_\mu(x)$ in spatial direction μ and another link $U^N_\nu(x)$ in orthogonal spatial direction ν. Then consider the sum of spatial paths $U^N_\mu U^N_\mu$, $U^N_\nu U^N_\mu U^N_\mu (U^N_\nu)^T$, and $(U^N_\nu)^T U^N_\mu U^N_\mu U^N_\nu$ before projecting this sum back to

the 'nearest' $SO(N)$ matrix. We have then constructed a blocked link U_μ^{N+1} of length $2^{N+1}a$ that is larger and fatter in both spatial directions. This defines the blocking procedure. We can then construct operators from these blocked links at each blocking level. We note that the spatial lattice size L_s need not necessarily be a multiple of the length of a blocked link. We can use links from lower blocking levels along with staples to span the length that we require.

Blocking also increases the number of operators that we can use. The spatial length size L_s sets the number of blocking levels $N_{\text{blocking}} = [\log_2(L_s)] + 1$ where $[\cdots]$ is the floor function. Then we can define Polyakov loop operators at each blocking level so that we use N_{blocking} operators in total.

3.1.3 $\mathbb{Z}_2$ symmetry

In an $SO(2\tilde{N})$ gauge theory, there is a $\mathbb{Z}_2$ symmetry under which the action and measure are invariant. Consider two neighbouring lattice slices in the $x-t$ plane. Then we can transform the lattice links that join these two slices in the y-direction by a non-trivial element of the centre z of the symmetry, which is $z = -I$ for a $\mathbb{Z}_2$ symmetry, so that for y_0 some value of y

$$U_y(x, y_0, t) \to z U_y(x, y_0, t) \ \ \forall x, t \tag{3.4}$$

Under this $\mathbb{Z}_2$ symmetry, a contractible loop such as the plaquette is invariant since it transforms with a factor $z^2 = 1$. However, a Polyakov loop that winds around the spatial torus in the y-direction is not invariant since it transforms with a factor z. Hence, a Polyakov loop operator has no overlap on contractible loops and hence glueball states. Furthermore, the vacuum expectation value for the Polyakov loop operator ϕ must be zero since

$$\langle \phi \rangle = z \langle \phi \rangle \Rightarrow \langle \phi \rangle = 0 \tag{3.5}$$

For the same reason, Polyakov loop operators cannot mix with contractible loop operators since the expectation value of the combination of these two operator types is also zero. These results break down if this symmetry spontaneously breaks such as in the high temperature deconfining phase. These properties may not hold for $SO(2\tilde{N}+1)$ gauge theories since there is no $\mathbb{Z}_2$ symmetry. Hence, we cannot expect that the expectation value $\langle \phi \rangle = 0$ in these cases.

3.2 String tension models

3.2.1 Linear potential

As we will discuss later, we can measure the potential of the flux tube between two static charges by considering how the Polyakov loop mass $m_P(l)$ varies with its length l. Given that the Polyakov loop represents the potential between two static charges, we would expect the lowest energy E_{min} varies linearly with the flux loop length l at large l.

$$\lim_{l\to\infty} E_{\text{min}}(l) = \sigma l \tag{3.6}$$

Here, the proportionality constant σ is the string tension and is the coefficient for linear confinement that we will explore later. We also know the first order correction term is the Lüscher term proportional to $1/l$ [27, 28].

$$\lim_{l\to\infty} E_{\text{min}}(l) = \sigma l - \frac{\pi}{6l} \tag{3.7}$$

3.2.2 Nambu-Goto model

We expect a flux loop to have a width of $\mathcal{O}(1/\sqrt{\sigma})$. For a long flux loop of length l where $l \gg 1/\sqrt{\sigma}$, the flux loop is string-like and the lowest lying excitations are massless modes along the string described by transverse fluctuations. The simplest bosonic string theory is the Nambu-Goto free string theory in flat spacetime. The ground state energy in this theory is given by

$$E(l) = \sigma l \left(1 - \frac{\pi}{3\sigma l^2}\right)^{\frac{1}{2}} \tag{3.8}$$

This expression expands to give (3.7) to $\mathcal{O}(1/l)$. Previous papers on $SU(N)$ gauge theories [29–31] showed that the predictions of this Nambu-Goto model agree well with the calculated energy spectrum, even below the critical length for excited string states at which the expansion of the Nambu-Goto energy in powers of $1/l^2$ diverges and we need to resum the series.

To test whether this is a suitable model for $SO(N)$ string tensions, we consider $SO(8)$ Polyakov loops at fixed $\beta = 84.0$ for volumes $L_s^2 36$ where $12 \leq L_s \leq 36$. We calculate the string tension $a^2\sigma$, which should be independent from L_s, from the Polyakov loop masses using the three expressions above: the Nambu-Goto model (3.8), a linear fit (3.6), and with a Lüscher (3.7) correction. We list the Polyakov loop masses and calculated string tensions in Table 3.1 and we plot the string

tensions $a^2\sigma$ against L_s in Figure 3.1. We see that the string tensions converge to a similar value as L_s increases. However, there are corrections at low L_s. Out of the three models, the string tension from the Nambu-Goto model converges fastest and the corrections at small L_s to the asymptotic value are least.

We therefore use the Nambu-Goto model to extract the string tension from the Polyakov loop masses. We can rearrange (3.8) to give us the string tension $a^2\sigma$ in physical units

$$a^2\sigma = \frac{\frac{\pi}{3} + \sqrt{\frac{\pi^2}{9} + 4a^2L_s^2E^2}}{2L_s^2} \tag{3.9}$$

where $l = aL_s$.

We note that Figure 3.1 also shows us the appropriate scale above which we can obtain accurate string tensions from the Nambu-Goto model. In the case of Table 3.1, we see that the $L_s = 20$ string tension is within errors of the asymptotic value. This scale is equivalent to $l\sqrt{\sigma} \sim 2.7$. Hence, we need $l\sqrt{\sigma} \geq 2.7$ for the Nambu-Goto model to give the correct string tension. For $SO(8)$, we use $l\sqrt{\sigma} = 3.7$. In practice, we use higher $l\sqrt{\sigma}$ values than required to obtain the correct string tension from the Nambu-Goto model because we simultaneously calculate the mass spectrum at the same values. This requires a higher $l\sqrt{\sigma}$ value to avoid torelon mixing with glueball states, as we explain later.

3.3 Continuum limits

3.3.1 Methodology

We are now ready to calculate string tensions. We use the normalised Polyakov loop operators that we defined in (3.3). We then use blocking levels to create a basis of operators. We use the variational method to calculate correlation functions before applying exponential fits to obtain energy estimates. We then use the Nambu-Goto model to obtain the string tensions from the energies.

Having obtained string tensions at different lattice spacings, we then want to obtain the continuum limit. Since g^2 is the only mass scale in the theory, we express the string tension in terms of coupling units $\sqrt{\sigma}/g^2$. In the continuum limit, we expect that

$$\lim_{\beta\to\infty} \frac{\beta a\sqrt{\sigma}}{2N^2} = \frac{\sqrt{\sigma}}{g^2N} \tag{3.10}$$

where we have taken the limit using dimensionless quantities and we express the string tension in 't Hooft coupling units $\sqrt{\sigma}/(g^2N)$.

We can obtain this continuum limit by extrapolating values of $a^2\sigma$ at different lattice spacing values a and adding a correction term.

$$\frac{\beta a\sqrt{\sigma}}{2N^2} = c_0 + \frac{c_1}{\beta} \tag{3.11}$$

Previous papers [32] indicate that the bare lattice coupling does not provide a very good definition of the running coupling since there are large higher order corrections compared to some more physical couplings. An example of one such physical coupling is the mean field improved coupling

$$\beta_I = \beta \left\langle \frac{1}{N}\mathrm{tr}(U_p) \right\rangle \tag{3.12}$$

which previous papers for $SU(N)$ gauge theories have used successfully [2]. Hence, we choose this coupling to obtain the continuum limits so that

$$\frac{\beta_I a\sqrt{\sigma}}{2N^2} = c_0 + \frac{c_1}{\beta_I} \tag{3.13}$$

We can then consider applying fits to obtain the constants c_0 and c_1, and c_0 is the estimate for $\sqrt{\sigma}/(g^2N)$. There may also be higher order corrections for low β values, or equivalently for large lattice spacings a, so we would need to remove the lowest β values systematically until we obtained an acceptable $\bar{\chi}^2_{\mathrm{dof}}$ fit.

3.3.2 $SO(4)$, $SO(6)$, $SO(7)$, $SO(8)$, $SO(12)$, and $SO(16)$

We list the average plaquette values, Polyakov loop masses, and string tensions at different lattice spacings for $SO(4)$, $SO(6)$, $SO(7)$, $SO(8)$, $SO(12)$, and $SO(16)$ in Tables 3.2, 3.3, 3.4, 3.5, 3.6, and 3.7. We display the continuum extrapolation plots in Figures 3.2, 3.3, 3.4, 3.5, 3.6, and 3.7. We list the continuum string tension values in 't Hooft coupling units of $\sqrt{\sigma}/(g^2N)$ in Table 3.8. We see that the string tensions are very accurate with very low errors. We will see that string tensions are some of the most precise calculations we can do on the lattice and we will use them to set a mass scale for other quantities. The continuum extrapolations are all very good with low $\bar{\chi}^2_{\mathrm{dof}}$ values, indicating that (3.13) is the correct model and there are negligible further corrections.

Returning to our earlier statement about the expectation value $\langle\phi\rangle$ in $SO(2\tilde{N}+1)$ theories, the $SO(7)$ calculations indicate that $\langle\phi\rangle \approx 0$ within very small fluctuations.

3.4 Large-N limits

Given 't Hooft's argument that we explained previously, we expect the physics of an $SO(N)$ gauge theory to approach a large-N limit if we hold the 't Hooft coupling g^2N constant. Hence, we expect $\sqrt{\sigma}/(g^2N)$ to converge to a large-N limit.

$$\lim_{N\to\infty} \frac{\sqrt{\sigma}}{g^2N} = \left.\frac{\sqrt{\sigma}}{g^2N}\right|_{SO(N\to\infty)} \tag{3.14}$$

Furthermore, if we apply 't Hooft's $1/N$ argument that we explained previously, we expect the leading correction to this limit at finite $SO(N)$ to be proportional to $1/N$

$$\left.\frac{\sqrt{\sigma}}{g^2N}\right|_{SO(N\to\infty)} = \frac{\sqrt{\sigma}}{g^2N} + \frac{c_1}{N} \tag{3.15}$$

for a constant c_1.

To verify this correction, we fit the string tension data with

$$\left.\frac{\sqrt{\sigma}}{g^2N}\right|_{SO(N\to\infty)} = c_0 + \frac{c_1}{N^\alpha} \tag{3.16}$$

for constants c_0, c_1, and exponent α. In Figure 3.8, we show how the goodness of fit $\bar{\chi}^2_{\text{dof}}$ varies with the power α. Along with free fits for α in (3.16), this indicates that $\alpha = 1.07(5)$ in agreement with a leading $\mathcal{O}(1/N)$ correction. We now assume a leading $\mathcal{O}(1/N)$ correction.

We apply a large-$\tilde{N}$ extrapolation to the $SO(2\tilde{N})$ values since these are the relevant values to compare to the $SU(\tilde{N})$ large-$\tilde{N}$ limit. We also rescale the $SO(2\tilde{N})$ string tension values in terms of $g^2\tilde{N} = g^2N/2$, which is the relevant 't Hooft coupling when comparing to $SU(\tilde{N})$ values as we will see later. We list these rescaled values in Table 3.9. Fitting to the $SO(2\tilde{N})$ values linearly and quadratically, we obtain

$$\begin{aligned}
&\frac{\sqrt{\sigma}}{g^2\tilde{N}} = 0.1985(5) - \frac{0.1563(14)}{\tilde{N}} && \bar{\chi}^2_{\text{dof}} = 0.79 && \tilde{N} \geq 2 \\
&\frac{\sqrt{\sigma}}{g^2\tilde{N}} = 0.1977(8) - \frac{0.1527(8)}{\tilde{N}} && \bar{\chi}^2_{\text{dof}} = 0.29 && \tilde{N} \geq 3 \\
&\frac{\sqrt{\sigma}}{g^2\tilde{N}} = 0.1968(13) - \frac{0.1440(87)}{\tilde{N}} - \frac{0.0185(129)}{\tilde{N}^2} && \bar{\chi}^2_{\text{dof}} = 0.16 && \tilde{N} \geq 2
\end{aligned} \tag{3.17}$$

We see that the fits have low $\bar{\chi}^2_{\text{dof}}$ values and that these values agree well with each other. The slightly larger difference between the quadratic fit and the $\tilde{N} \geq 2$ linear fit when compared to the $\tilde{N} \geq 3$ linear fit indicates that there may be $\mathcal{O}(1/\tilde{N}^2)$ corrections from the $SO(4)$ value. Hence,

we choose the $\tilde{N} \geq 3$ linear fit (3.17) as the $SO(N \to \infty)$ value. We display this plot in Figure 3.9. We also note that the $SO(7)$ string tension value agrees well with the extrapolation.

3.5 Equivalences between $SO(N)$ and $SU(N)$ gauge theories

3.5.1 Lie algebra equivalences

We know that $SO(4)$ and $SU(2) \times SU(2)$ share a Lie algebra so we could ask how the string tensions and couplings $\sqrt{\sigma}/g^2$ compare between $SO(4)$ and $SU(2)$. For the cross product group $SU(2) \times SU(2)$, we expect a contribution from each $SU(2)$ group to the string tension so that

$$\sigma|_{SO(4)} = \sigma|_{SU(2)\times SU(2)} = 2\,\sigma|_{SU(2)} \tag{3.18}$$

As we will see later, the $SO(4)$ and $SU(2)$ mass spectrum $m_G/\sqrt{\sigma}$ indicates that these string tensions are related in this way. We know the $SO(4)$ and $SU(2)$ string tensions [33].

$$\begin{aligned} \frac{\sqrt{\sigma}}{g^2} &= 0.2404(7) \qquad && SO(4) \\ \frac{\sqrt{\sigma}}{g^2} &= 0.3351(8) \qquad && SU(2) \end{aligned} \tag{3.19}$$

Hence, we can use these results to relate the $SO(4)$ and $SU(2)$ couplings.

$$\begin{aligned} \frac{g^2|_{SO(4)}}{g^2|_{SU(2)}} &= \frac{g^2}{\sqrt{\sigma}}\bigg|_{SO(4)} \frac{\sqrt{\sigma}|_{SO(4)}}{\sqrt{\sigma}|_{SU(2)}} \frac{\sqrt{\sigma}}{g^2}\bigg|_{SU(2)} \\ &= \sqrt{2}\frac{\sqrt{\sigma}/g^2|_{SU(2)}}{\sqrt{\sigma}/g^2|_{SO(4)}} \\ &= 1.97(1) \end{aligned} \tag{3.20}$$

This indicates that $g^2|_{SO(4)} = 2\,g^2|_{SU(2)}$.

As we discussed previously, we know that $SO(6)$ and $SU(4)$ share a common Lie algebra so we might ask how the string tensions $\sqrt{\sigma}/g^2$ compare between $SO(6)$ and $SU(4)$. We recall that in $SU(4)$, $4 \otimes 4 = 6 \otimes 10$ where the 6 corresponds to the $k = 2$ antisymmetric representation and maps to the fundamental 6 of $SO(6)$. Hence, we expect that the $SO(6)$ fundamental string tension $\sigma_f|_{SO(6)}$ is equal to the $SU(4)$ $k = 2A$ value $\sigma_{2A}|_{SU(4)}$.

$$\sigma_f|_{SO(6)} = \sigma_{2A}|_{SU(4)} \tag{3.21}$$

We also need to relate the couplings between the two theories. To do this, consider a mixed $SU(4)$

plaquette action with fundamental and $k = 2A$ terms [10]

$$\beta_{\text{mixed}} S_{\text{mixed}} = \beta_f \sum_p \left(1 - \frac{1}{N_f} \text{tr}_f(U_p)\right) + \beta_{2A} \sum_p \left(1 - \frac{1}{N_{2A}} \text{tr}_{2A}(U_p)\right) \tag{3.22}$$

where f represents the fundamental representation, $2A$ represents the $k = 2A$ representation, and $\beta_f = 2N_f/g_f^2$ and $\beta_{2A} = 2N_{2A}/g_{2A}^2$. We use that $\text{tr}_{2A}(U_p) = \frac{1}{2}\left[(\text{tr}_f(U_p))^2 - \text{tr}_f(U_p)^2\right]$ and that $N_f = 4$ and $N_{2A} = 6$ for $SU(4)$ to carry out a weak coupling expansion. By requiring that the coefficients to the $F_{\mu\nu}^2$ terms from the fundamental and $k = 2A$ parts are equal, we expect that

$$g_f^2\big|_{SO(6)} = g_{2A}^2\big|_{SU(4)} = 2\, g_f^2\big|_{SU(4)} \tag{3.23}$$

We know the $SO(6)$ and $SU(4)$ string tensions [2, 33].

$$\begin{aligned} \frac{\sqrt{\sigma}}{g_f^2} &= 0.4402(12) && SO(6) \\ \frac{\sqrt{\sigma_{2A}}}{g_f^2} &= 0.8832(41) && SU(4) \end{aligned} \tag{3.24}$$

Hence, we can use these results to relate the $SO(6)$ and $SU(4)$ couplings.

$$\begin{aligned} \frac{g_f^2\big|_{SO(6)}}{g_f^2\big|_{SU(4)}} &= \left.\frac{g_f^2}{\sqrt{\sigma_f}}\right|_{SO(6)} \frac{\sqrt{\sigma_f}|_{SO(6)}}{\sqrt{\sigma_{2A}}|_{SU(4)}} \left.\frac{\sqrt{\sigma_{2A}}}{g_f^2}\right|_{SU(4)} \\ &= \frac{\sqrt{\sigma_{2A}}/g_f^2\big|_{SU(4)}}{\sqrt{\sigma_f}/g_f^2\big|_{SO(6)}} \\ &= 2.006(15) \end{aligned} \tag{3.25}$$

This agrees very well with our expectation (3.23).

3.5.2 Large-N orbifold equivalence

We showed previously that the large-N orbifold equivalence indicates that the physics of $SO(2\tilde{N})$ and $SU(\tilde{N})$ gauge theories may match at the large-$\tilde{N}$ limit if we set $g_{SO(2\tilde{N})}^2 = g_{SU(\tilde{N})}^2$. We want to see if the continuum string tensions match in the large-N limit.

We also showed that we can obtain a large-N extrapolation from values at finite N if we hold the 't Hooft coupling $\lambda = g^2 N$ constant. Hence, we can compare the continuum string tensions between $SO(2\tilde{N})$ and $SU(\tilde{N})$ gauge theories if we hold constant

$$g^2_{SU(\tilde{N})}\tilde{N} = g^2_{SO(2\tilde{N})}\tilde{N} = g^2_{SO(2\tilde{N})}N/2 \tag{3.26}$$

for $N = 2\tilde{N}$, so that we expect

$$\lim_{N\to\infty} \frac{\sqrt{\sigma}}{g^2_{SU(\tilde{N})}\tilde{N}} = \lim_{\tilde{N}\to\infty} \frac{\sqrt{\sigma}}{g^2_{SO(2\tilde{N})}\tilde{N}} = \lim_{N\to\infty} 2\frac{\sqrt{\sigma}}{g^2_{SO(2\tilde{N})}N} \tag{3.27}$$

This is why we doubled the $SO(2\tilde{N})$ continuum string tensions in Table 3.8, converting $\sqrt{\sigma}/(g^2N)$ to $\sqrt{\sigma}/(g^2\tilde{N}) = 2\sqrt{\sigma}/(g^2N)$. It was because we wanted to compare the $SO(2\tilde{N})$ large-N limit to the $SU(\tilde{N})$ large-$\tilde{N}$ limit.

We list the continuum string tensions for $SO(2\tilde{N})$ and $SU(\tilde{N})$ [34] gauge theories in Table 3.9. We obtain the $SU(\tilde{N})$ large-$\tilde{N}$ string tension by a quadratic fit using a leading $\mathcal{O}(1/\tilde{N}^2)$ correction to the $SU(\tilde{N})$ data and we compare this fit to the $\tilde{N} \geq 3$ linear fit to the $SO(2\tilde{N})$ data in (3.17). We display a plot of the $SO(2\tilde{N})$ and $SU(\tilde{N})$ continuum string tensions against $1/\tilde{N}$ and their large-$\tilde{N}$ extrapolations in Figure 3.9.

The large-$\tilde{N}$ values are

$$\begin{aligned} \lim_{\tilde{N}\to\infty} \frac{\sqrt{\sigma}}{g^2\tilde{N}} &= 0.1977(8) && SO(2\tilde{N}) \\ \lim_{\tilde{N}\to\infty} \frac{\sqrt{\sigma}}{g^2\tilde{N}} &= 0.1974(2) && SU(\tilde{N}) \end{aligned} \tag{3.28}$$

This shows that the rescaled $SO(2\tilde{N} \to \infty)$ and $SU(\tilde{N} \to \infty)$ values agree within errors, validating our expectation from the large-N orbifold equivalence (3.27).

3.6 Data

		String tensions $a^2\sigma$		
L_s	am_P	Nambu-Goto	Linear	Lüscher
12	0.1349(15)	0.01545(12)	0.01124(13)	0.01488(13)
16	0.2366(19)	0.01697(12)	0.01479(12)	0.01683(12)
20	0.3306(19)	0.01789(9)	0.01653(10)	0.01784(10)
24	0.4078(41)	0.01792(17)	0.01699(17)	0.01790(17)
28	0.4834(22)	0.01795(8)	0.01726(8)	0.01793(8)
32	0.5606(19)	0.01804(6)	0.01752(6)	0.01803(6)
36	0.6354(22)	0.01806(6)	0.01765(6)	0.01805(6)

Table 3.1: $SO(8)$ Polyakov loop masses, and string tensions with errors from three different models.

$L_s^2 L_t$	β	$\frac{1}{N}\mathrm{tr}(U_p)$	am_P	$a\sqrt{\sigma}$
$20^2 28$	11.0	0.80135	0.8337(22)	0.2074(3)
$24^2 32$	12.2	0.82295	0.7810(46)	0.1829(5)
$28^2 36$	13.7	0.84402	0.6996(20)	0.1602(2)
$32^2 40$	15.1	0.85955	0.6336(51)	0.1425(6)
$36^2 44$	16.5	0.87223	0.5881(25)	0.1294(3)
$40^2 48$	18.7	0.88808	0.4959(15)	0.1128(2)

Table 3.2: $SO(4)$ average plaquette values, Polyakov loop masses, and string tensions.

$L_s^2 L_t$	β	$\frac{1}{N}\mathrm{tr}(U_p)$	am_P	$a\sqrt{\sigma}$
$16^2 24$	23.0	0.75878	1.2721(140)	0.2856(15)
$20^2 28$	28.0	0.80677	0.9798(18)	0.2243(2)
$24^2 32$	33.0	0.83851	0.7938(27)	0.1844(3)
$28^2 36$	37.0	0.85718	0.7145(21)	0.1618(2)
$32^2 40$	41.0	0.87194	0.6452(25)	0.1438(3)
$36^2 48$	46.0	0.88656	0.5620(19)	0.1266(2)

Table 3.3: $SO(6)$ average plaquette values, Polyakov loop masses, and string tensions.

$L_s^2 L_t$	β	$\frac{1}{N}\mathrm{tr}(U_p)$	am_P	$a\sqrt{\sigma}$
$16^2 24$	35.0	0.78116	1.0714(51)	0.2628(6)
$20^2 28$	42.0	0.82117	0.8572(18)	0.2102(2)
$24^2 32$	49.0	0.84862	0.7144(21)	0.1752(2)
$28^2 36$	57.0	0.87112	0.5921(16)	0.1477(2)
$32^2 40$	64.0	0.88592	0.5249(8)	0.1301(1)
$36^2 44$	70.0	0.89613	0.4832(17)	0.1176(2)

Table 3.4: $SO(7)$ average plaquette values, Polyakov loop masses, and string tensions.

$L_s^2 L_t$	β	$\frac{1}{N}\mathrm{tr}(U_p)$	am_P	$a\sqrt{\sigma}$
$16^2 24$	51.0	0.80206	0.8721(24)	0.2379(3)
$20^2 28$	62.0	0.84000	0.6888(11)	0.1891(1)
$24^2 32$	73.0	0.86561	0.5669(15)	0.1567(2)
$28^2 36$	84.0	0.88409	0.4834(22)	0.1340(3)
$32^2 40$	94.0	0.89696	0.4307(16)	0.1182(2)
$36^2 44$	105.0	0.90815	0.3827(13)	0.1051(2)

Table 3.5: $SO(8)$ average plaquette values, Polyakov loop masses, and string tensions.

$L_s^2 L_t$	β	$\frac{1}{N}\mathrm{tr}(U_p)$	am_P	$a\sqrt{\sigma}$
$16^2 24$	132.0	0.82178	0.7240(29)	0.2176(4)
$20^2 28$	155.0	0.85007	0.6256(23)	0.1806(3)
$24^2 32$	175.0	0.86820	0.5760(14)	0.1579(2)
$28^2 36$	200.0	0.88546	0.4967(28)	0.1357(4)
$32^2 40$	225.0	0.89871	0.4397(26)	0.1194(3)
$36^2 48$	250.0	0.90920	0.3952(16)	0.1067(2)

Table 3.6: $SO(12)$ average plaquette values, Polyakov loop masses, and string tensions.

$L_s^2 L_t$	β	$\frac{1}{N}\mathrm{tr}(U_p)$	am_P	$a\sqrt{\sigma}$
$16^2 24$	247.0	0.82758	0.6971(44)	0.2137(6)
$20^2 28$	302.0	0.86092	0.5428(23)	0.1688(3)
$24^2 32$	353.0	0.88192	0.4627(20)	0.1422(3)
$28^2 36$	408.0	0.89848	0.3940(18)	0.1215(3)
$32^2 40$	456.0	0.90954	0.3524(13)	0.1074(3)
$36^2 48$	512.0	0.91974	0.3113(14)	0.0952(2)

Table 3.7: $SO(16)$ average plaquette values, Polyakov loop masses, and string tensions.

$SO(N)$	$\sqrt{\sigma}/(g^2N)$	$\bar{\chi}^2_{\mathrm{dof}}$
4	0.0601(2)	0.68
6	0.0734(2)	0.34
7	0.0771(1)	1.51
8	0.0798(2)	0.80
12	0.0863(3)	0.56
16	0.0892(3)	1.17

Table 3.8: $SO(N)$ continuum string tensions in g^2N units $\sqrt{\sigma}/(g^2N)$ and extrapolation $\bar{\chi}^2_{\mathrm{dof}}$.

$\tilde{N}$	$SO(2\tilde{N})$	$SU(\tilde{N})$
2	0.1202(4)	0.1675(3)
3	0.1467(4)	0.1839(2)
4	0.1596(3)	0.1902(3)
5		0.1924(3)
6	0.1726(6)	0.1944(3)
8	0.1783(6)	0.1955(3)

Table 3.9: $SO(2\tilde{N})$ and $SU(\tilde{N})$ [34] continuum string tensions in $g^2\tilde{N}$ units $\sqrt{\sigma}/(g^2\tilde{N})$.

3.7 Figures

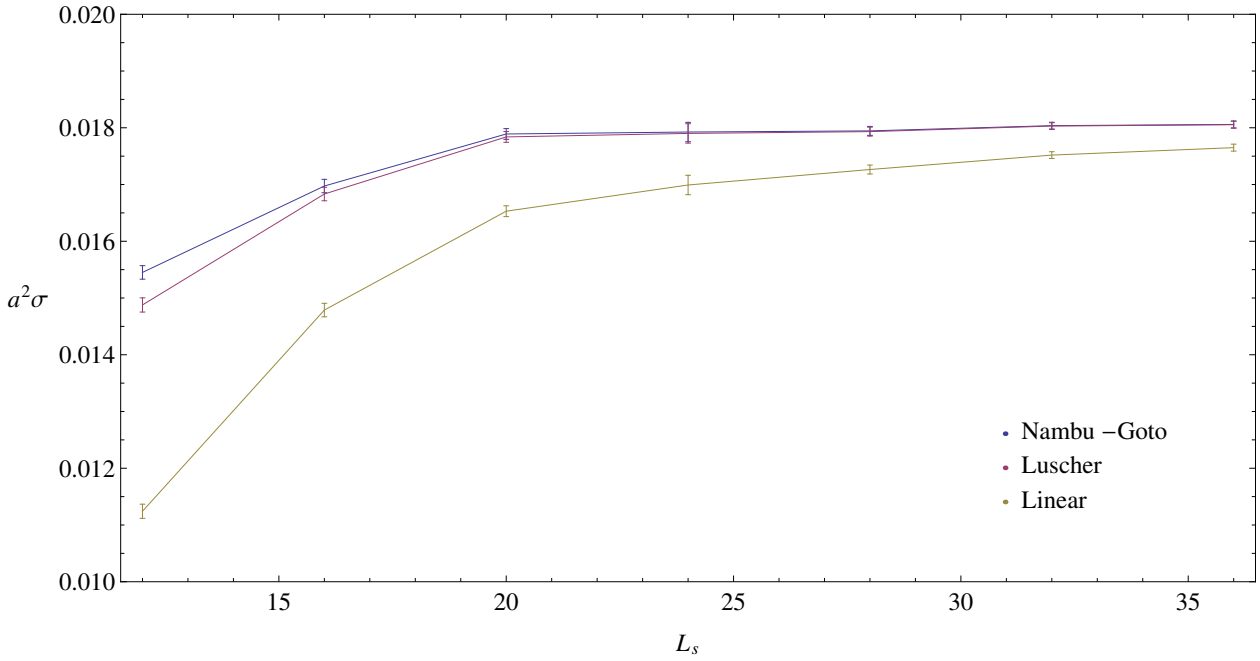

Figure 3.1: $SO(8)$ string tensions calculated from three different string tension models.

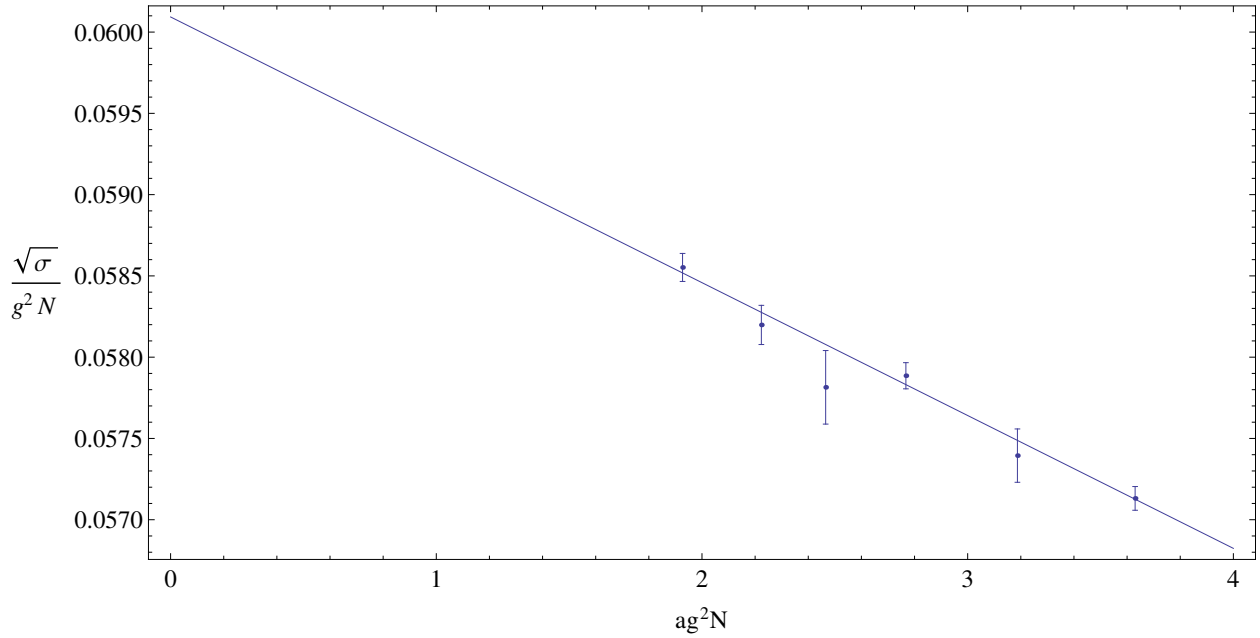

Figure 3.2: Continuum extrapolation of $SO(4)$ string tensions in g^2N units.

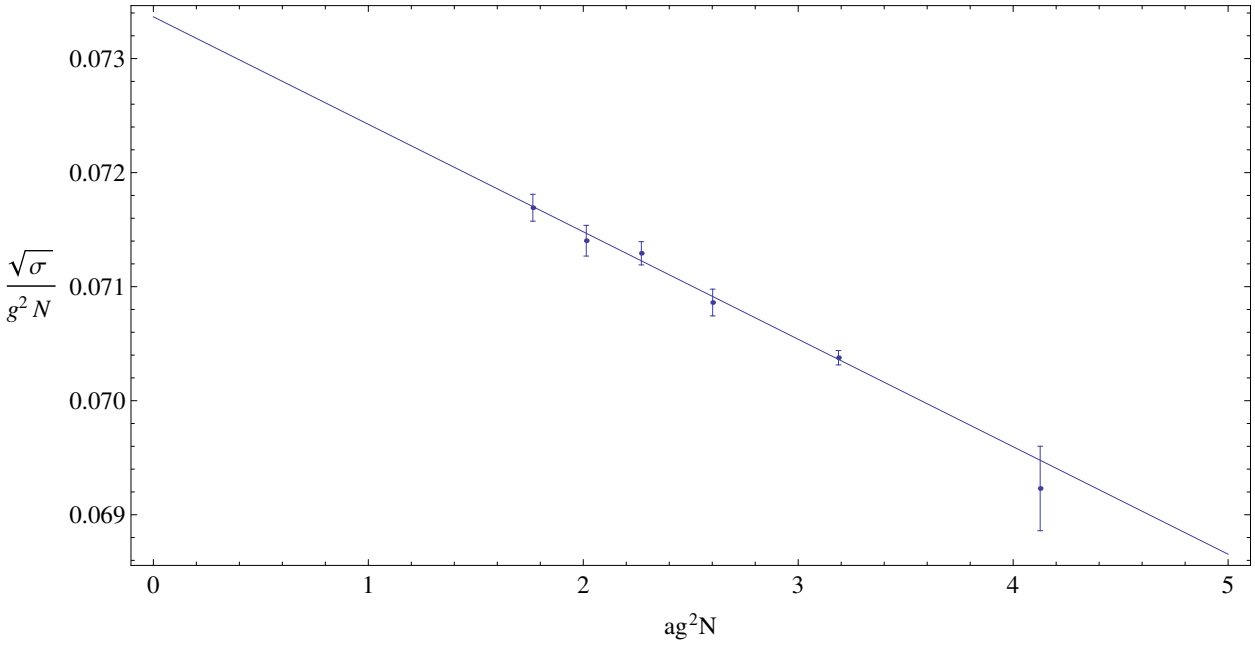

Figure 3.3: Continuum extrapolation of $SO(6)$ string tensions in g^2N units.

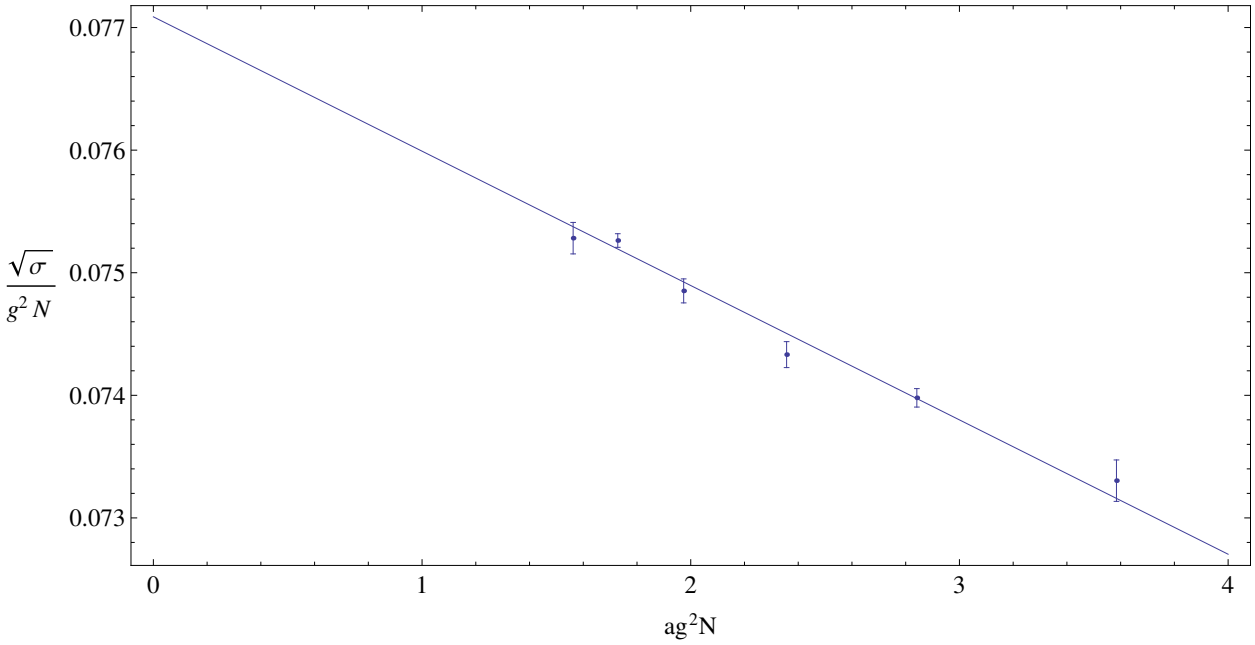

Figure 3.4: Continuum extrapolation of $SO(7)$ string tensions in g^2N units.

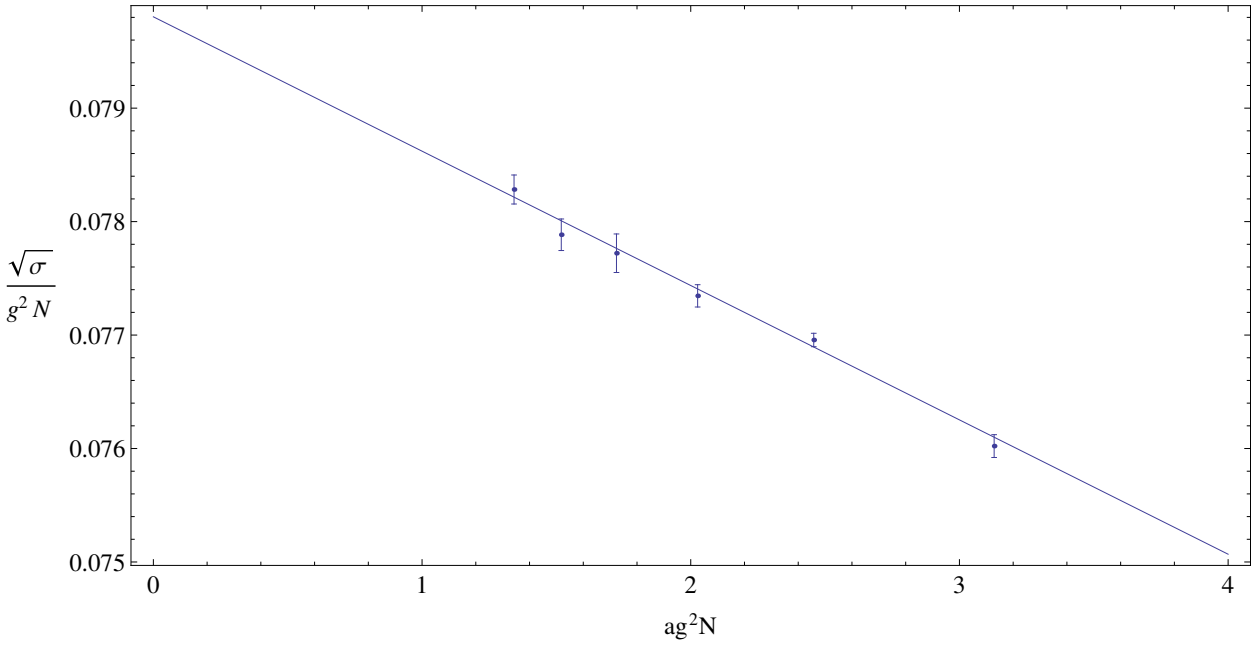

Figure 3.5: Continuum extrapolation of $SO(8)$ string tensions in g^2N units.

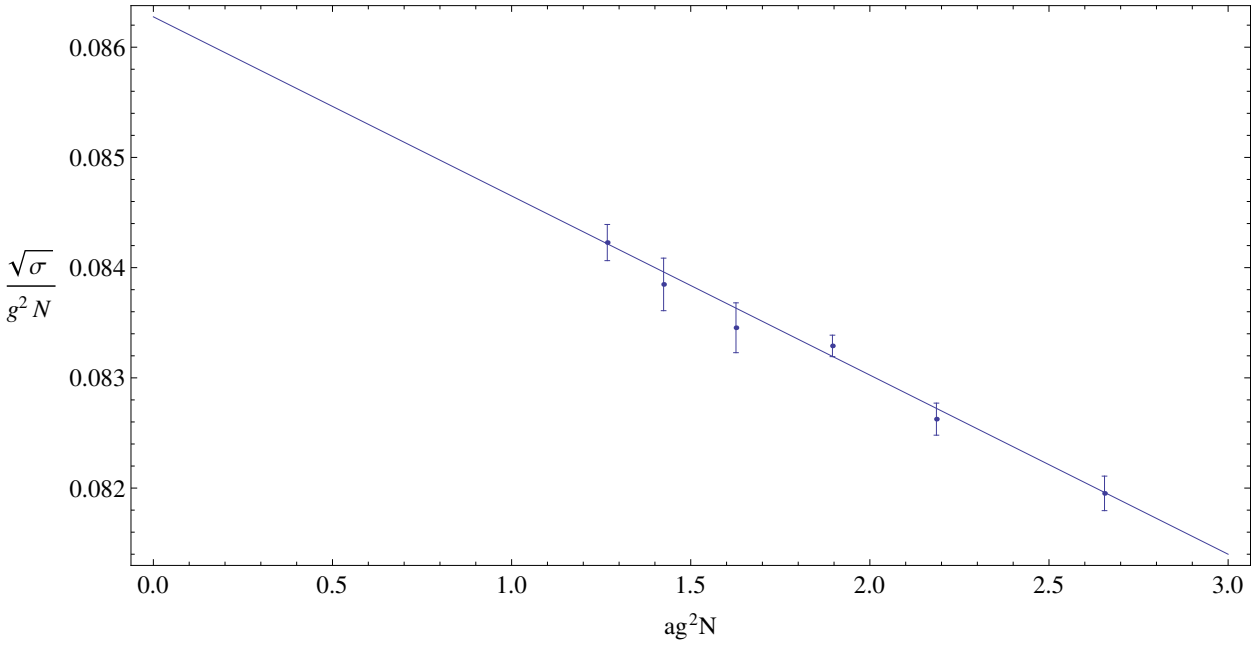

Figure 3.6: Continuum extrapolation of $SO(12)$ string tensions in g^2N units.

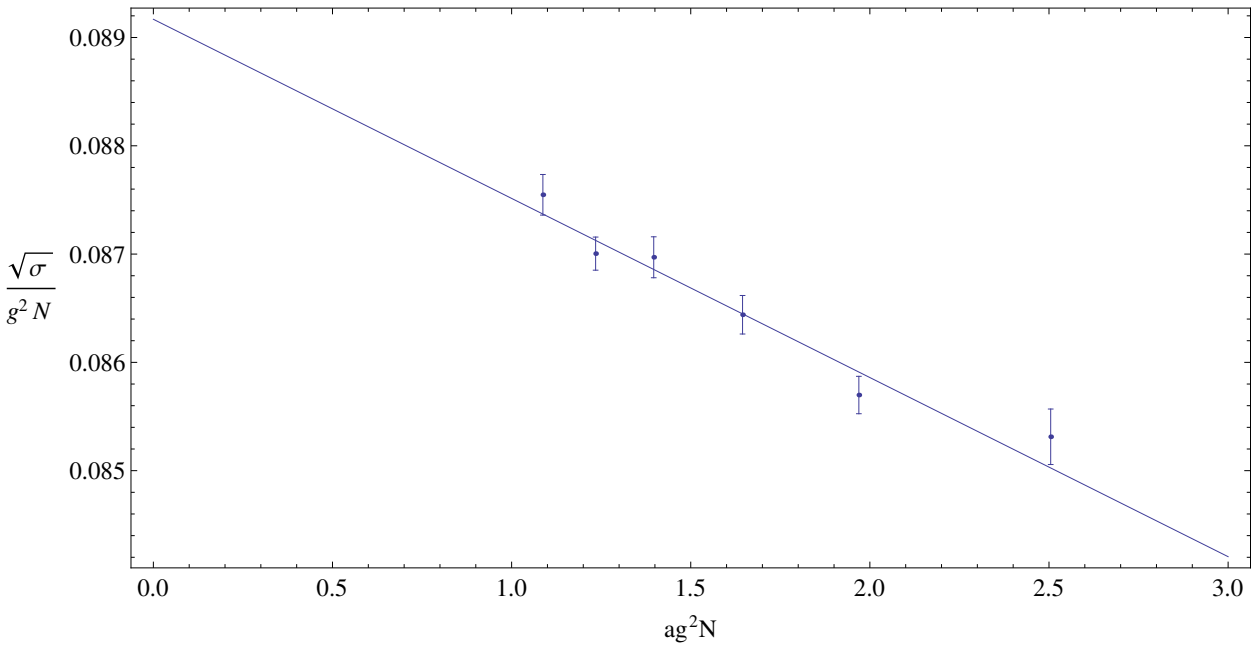

Figure 3.7: Continuum extrapolation of $SO(16)$ string tensions in g^2N units.

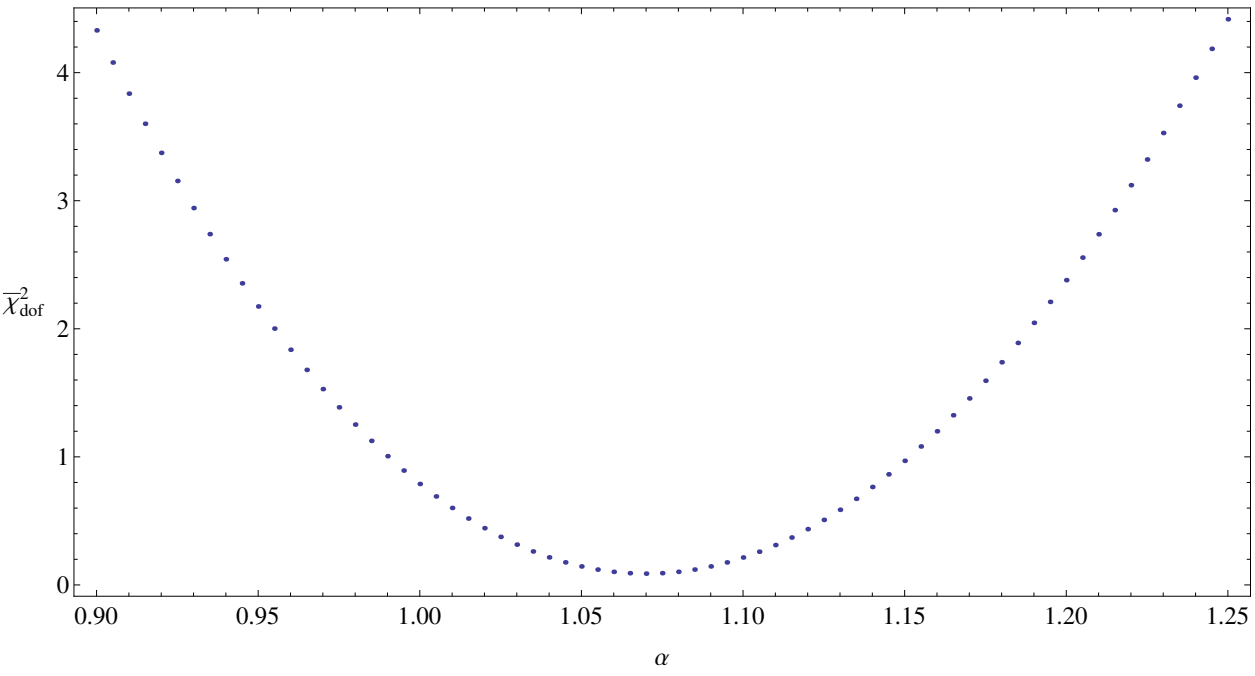

Figure 3.8: $\bar{\chi}^2_{\text{dof}}$ against the power α of the leading large-N correction when fitting $\sqrt{\sigma}/(g^2N) = c_0 + \frac{c_1}{N^\alpha}$. The minimum $\bar{\chi}^2_{\text{dof}}$ of this plot is at $\alpha = 1.07(5)$.

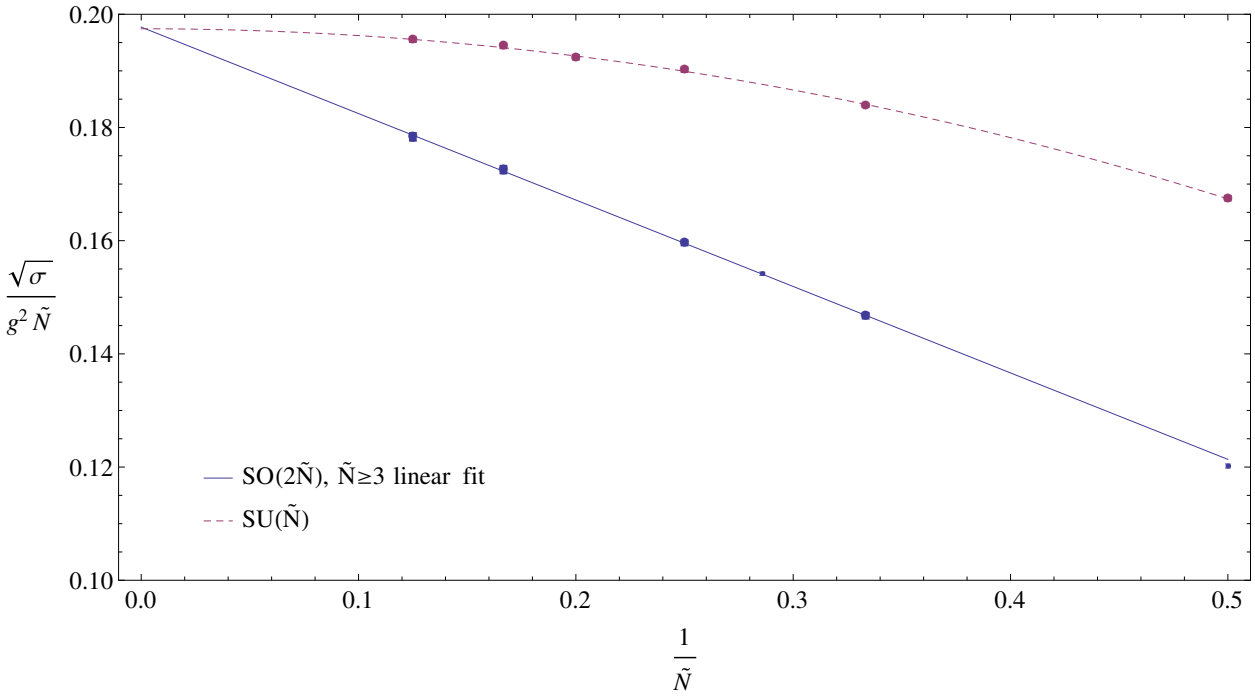

Figure 3.9: Large-$\tilde{N}$ extrapolation of $SO(2\tilde{N} \to \infty)$ and $SU(\tilde{N} \to \infty)$ continuum string tensions in $g^2\tilde{N}$ units. We use only the thick style points in the extrapolation.

Chapter 4

Mass spectrum

In this chapter, we calculate the mass spectrum of $SO(N)$ gauge theories in $2+1$ dimensions. We first consider the operators that project on to glueball states and the finite size corrections that we need to control. We then present our continuum values before extrapolating to the large-N limit. We finally compare $SO(N)$ and $SU(N)$ mass spectra between group equivalences.

4.1 Glueball operators

4.1.1 Quantum numbers

We want to construct colour singlet operators since we assume that the theory is confining. Since traces of closed loops on the lattice are colour singlets, we will construct glueball operators from closed loops. By making our operators translationally invariant, we can set all operators to have zero momentum $p = 0$. We do this by summing configurations of closed loops over all points on a spatial lattice. We want the operators to project on to J^P glueball states with spin J and parity P. We can do this by constructing glueball operators ϕ that use link variable products of rotations and translations of a closed curve $\mathcal{C}$. In particular, if $U_{\mathcal{C}}$ is the ordered link variable product on an arbitrary closed curve $\mathcal{C}$, then we can construct an operator ϕ from the following linear combination [2].

$$\phi(t) = \sum_{\mathbf{x}} \sum_{n} e^{ij\theta_n} \mathrm{tr}\big\{U_{R(\theta_n)\mathcal{C}} \pm U_{PR(\theta_n)\mathcal{C}}\big\} \tag{4.1}$$

Here, $\theta_n = \frac{n\pi}{2}$ where $n \in \mathbb{Z}$, $R(\theta_n)$ is a rotation by angle θ_n, P is the parity transformation, and the sum $\sum_{\mathbf{x}}$ is over points on the spatial slice at time t. This operator then projects on to a state with spin $J = j$ and parity $P = \pm$. We note that since all $SO(N)$ traces are real, these glueball

operators will necessarily project on to states with charge conjugation $C = +$. For $J = 1$ states, we take the real part of the correlation function $\langle \phi(t)\phi^\dagger(0)\rangle$ to ensure that the operators are real.

$$\mathrm{Re}\left(\left\langle \phi_i \phi_j^\dagger \right\rangle\right) = \langle \mathrm{Re}\,(\phi_i)\,\mathrm{Re}\,(\phi_j)\rangle + \langle \mathrm{Im}\,(\phi_i)\,\mathrm{Im}\,(\phi_j)\rangle \tag{4.2}$$

There is some uncertainty over the value of J from our expression in (4.1). This occurs because we construct operators on a cubic lattice, breaking the continuum symmetry by discrete rotations of $\pi/2$. Hence, the state we label with spin $J = 0$ actually contains projections on to states with spin $J = 0, 4, 8, \ldots$, and similarly for states with spin $J = 1, 5, 9, \ldots$ and $2, 6, 10, \ldots$. We also note that parity doubling implies that we construct a state $|j, \pm\rangle = |j\rangle \pm P\,|j\rangle$ with spin $J = j$ and parity $P = \pm$ from two states $|j\rangle$ and $P\,|j\rangle$ with spins $J = j$ and $J = -j$ respectively. Hence, the state we label with spin $J = 1$ includes states with spin $J = -1$ and hence states with spins $J = 3, 7, 11, \ldots$. So the state $J = 1$ includes all states with odd spins.

For most states, we assume that the state with lowest positive spin has lowest mass and we use this assumption to label the lightest states for each respective spin. We will see that there is some evidence to show that this may not be true for some states.

4.1.2 Curves

We use a range of closed curves $\mathcal{C}$ to construct operators to project on to glueball states. The simplest such curves are the 1×1 plaquette, and the 1×2, $1 \times 3, \ldots$ rectangles. The square plaquette is invariant under $\pi/2$ rotations and so will only project on to $J = 0$ states while the rectangles are invariant under π rotations and so will only project on to $J = 0$ and $J = 2$ states. These curves are also invariant under parity and so will only project on to $P = +$ states. Hence, we need to consider more complicated curves to project on to $J = 1$ and $P = -$ states. To do this, we consider curves constructed from squares and rectangles that have no rotational or reflectional symmetry. We show four such curves in Figure 4.1.

We use twelve such curves to build, by rotations and reflections, a basis for each J^P state of twelve operators using (4.1). We also use two rectangle-based operators for 0^+ and 2^+ states and the plaquette for the 0^+ state. This means that we have a basis of fifteen operators for the 0^+ state and a basis of fourteen operators for the 2^+ state.

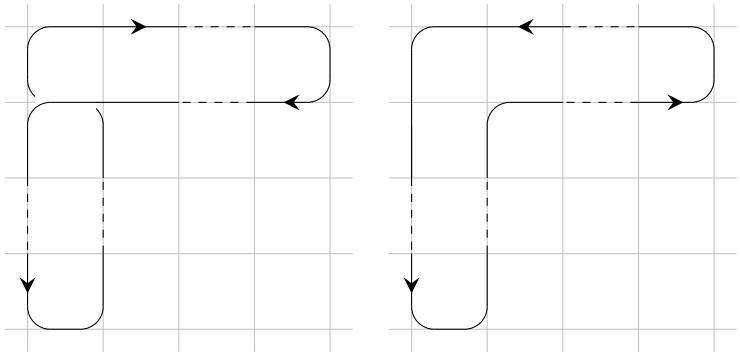

(a) Curve 1

(b) Curve 2

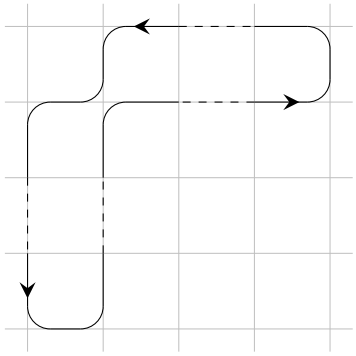

(c) Curve 3

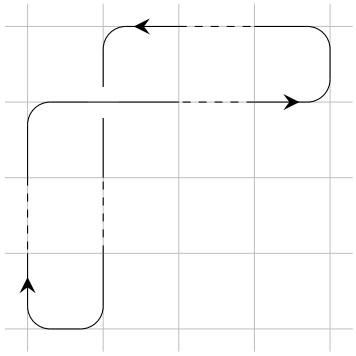

(d) Curve 4

Figure 4.1: We can construct asymmetric curves for glueball operators from rectangles. We can extend each rectangle arbitrarily, providing the curve has no overall rotational or reflectional symmetry.

4.1.3 Blocking

We use the same blocking procedure as for string tension operators to increase the basis of operators that we can use. As with the string tension operators, the spatial length size L_s sets the number of blocking levels $N_{\text{blocking}} = [\ln_2(L_s)] + 1$ where $[\cdots]$ is the floor function. Then we can use the basis operators at each blocking level so that we multiply the number of basic operators in the operator basis by N_{blocking}.

4.2 Finite volume effects

We need to control finite volume corrections to ensure that they do not affect the calculations. The two main sources of these corrections are from torelon mixing and glueball emission. We need the volumes to be sufficiently large that these finite volume corrections do not affect our results. To test how large the volumes need to be, we calculate values at different volumes until the differences are so small that the values are within errors of the infinite volume limit.

4.2.1 Finite volume study

To test these finite size corrections, we calculate $SO(8)$ glueball masses at fixed $\beta = 84.0$ for several different volumes, ranging from $12^2 36$ to $36^2 36$. We list the mass spectrum for each volume in Table 4.1 and plot the values in Figure 4.2. Here, an effective scale for the volume size is $l\sqrt{\sigma}$, which ranges from 1.5 to 4.8 in our results.

We make several observations from our data. Firstly, as we decrease L_s, there are indeed finite size corrections. These particularly affect the excited 0^+ states and all $2^\pm$ states. As we increase L_s, these mass values stabilise, indicating that finite size corrections are no longer significant beyond $L_s \geq 28$. Secondly, we can see that parity doubling breaks down at smaller L_s, and there are finite size corrections to the $2^\pm$ states. As we stated previously, we expect this since the periodic boundary conditions break the continuous rotational symmetry down to $\pi/2$ rotations. This breaks the argument for the $2^\pm$ degeneracy but not for the $1^\pm$ case as we see in our results. Again, as we increase L_s, parity doubling restores until there are no noticeable corrections at the volume $28^2 36$. Thirdly, we see that that the 0^+ and 2^+ states show significant finite size corrections when the asymptotic glueball mass is roughly equal to twice the Polyakov loop mass $2am_P(L_s) \approx am_G|_{L_s \to \infty}$. These corrections affect the 2^+ state more than the 0^+ state. This is because the 0^+ state is lighter than the 2^+ state and m_P increases as L_s increases so that the 0^+ state is volume independent at smaller L_s than the 2^+ state. These specific corrections are due to torelon mixing as we go on to describe.

4.2.2 Torelon mixing

Consider an operator made from two Polyakov loops $l_P l_P^T$. As with string tension operators, we can sum this operator over lattice sites $\mathbf{x}$ to create a zero momentum operator known as the torelon [2, 35]. This torelon state is a colour singlet and is made from contractible loops so that it can mix with glueball states. For very large L_s, this torelon state would couple to a state of two flux loops and so it would have a mass of $2am_P(L_s)$. Just as with glueball states, we can form torelon states with specific quantum numbers such as a 0^+ torelon state $l_x l_x^T + l_y l_y^T$ and a 2^+ torelon state $l_x l_x^T - l_y l_y^T$, which again have mass $2am_P(L_s)$ at large volumes. However, these torelon states can mix with glueball states at smaller volumes, contributing states with anomalously low 'masses' to appear in the spectrum. This is what we see at small volumes in Figure 4.2 when the lightest 0^+ and 2^+ states involve torelon states. Hence, we need

$$2am_P(L_s) > am_{2^+}|_{L_s\to\infty} \tag{4.3}$$

to ensure that we isolate the correct states in the mass calculations.

We can show that the mixing between glueball and torelon states decreases with N, following the argument in [14]. Consider gauge invariant local operators made from gauge fields $O_1, \ldots, O_m$ and the correlation function $\langle O_1 \ldots O_m \rangle$. Then we can construct a generating functional W in the usual way by adding source terms to the action $S \to S + N\sum_i c_i O_i$ for some numbers c_i and N corresponding to $SO(N)$. Then we can evaluate the correlation function in terms of the generating functional $\langle O_1 \ldots O_m \rangle \sim N^{-m} \frac{\partial^m W}{\partial c_1 \ldots \partial c_m}\Big|_{c_i=0}$. Given that the leading graphs are planar graphs and proportional to N^2, this implies that $\langle O_1 \ldots O_m \rangle \sim N^{2-m}$. Let O_P represent a single trace Polyakov loop operator. Since torelon operators O_T are double trace $O_T \sim O_P O_P$ and glueball operators O_G are single trace then a correlation function mixing glueball and torelon operators $\langle O_T O_G \rangle \sim \langle O_P O_P O_G \rangle$ would be $\mathcal{O}(1/N)$ compared to a correlation function with only glueball operators. Hence, we expect that mixing between glueball and torelon states decreases as N increases. Previous studies on the $SU(N)$ mass spectrum [35] have validated this expectation.

4.2.3 Glueball emission on a finite volume

Finite size corrections to the mass spectrum can arise from a glueball emitting another glueball that winds around the volume that is then reabsorbed [36]. On a finite spatial volume l^2 in an effective theory with mass gap m, the leading finite size corrections of this sort are $\mathcal{O}(e^{-cml})$ for some constant $c \sim \mathcal{O}(1)$. Hence, if the change in mass between two volumes is small, we can conclude that these values have small finite size corrections to the limit $l \to \infty$. Hence, we can effectively eliminate finite size corrections by measuring masses on sufficiently large lattices. In our case, we find in our calculations that $m/\sqrt{\sigma} > 3.6$ so that, if we set $l\sqrt{\sigma} > 3.5$, then $cml > 12.5$ and these corrections will be negligible.

4.2.4 Multi-glueball states

There are further corrections from multi-glueball states [37]. The glueball operators we use project on to all states with the corresponding quantum numbers. It is then possible for these operators to project on to multi-glueball states. For example, two 0^+ states with opposite momenta could appear in our calculations from the 0^+ operator. At small N, multitrace operators can appear corresponding to these multi-glueball states. At large-N, single trace operators dominate for the

same reasons as we described for torelon states above so that we only detect single particle states. Hence, this scattering is suppressed by at least $1/N$.

It is also possible that heavy glueball states are unstable at small N, and decay into multi-glueball states. This occurs when the mass of the heavy glueball exceeds twice the mass of the lightest glueballs. For example, an excited 2^+ glueball could decay into a lighter 2^+ and 0^+ glueballs or two 0^+ glueball with relative angular momentum $J = 2$. We could detect this through missing heavy states or new lighter states in the glueball spectrum. This decay is suppressed by $1/N$ so we do not expect to see it at large N.

In practice, we do not seem to detect these multi-glueball states in our results so it appears that both of these corrections do not appear even at small N.

4.2.5 Setting the scale

We hence want to set the scale to eliminate finite size corrections from our results. We showed above that the Polyakov loop mass $m_P(l) \approx l\sigma$ is the relevant value to consider torelon corrections. Since we will consider dimensionless mass ratios in string tension units $m_G/\sqrt{\sigma}$, we can set the correct scale for our calculations by ensuring that $m_P/\sqrt{\sigma} \approx l\sigma/\sqrt{\sigma} = l\sqrt{\sigma}$ is sufficiently large. To do this, we choose a specific β value on a given lattice volume corresponding to the desired value for $l\sqrt{\sigma}$ so that we should extract the correct $SO(N)$ mass spectrum without finite size corrections. Given the equivalence between $SO(N)$ and $SU(N)$ gauge theories, we use similar values for $l\sqrt{\sigma}$ that the $SU(N)$ papers used [2, 33]. As an example, consider the case of $SO(8)$. We will show later that, for $SO(8)$, $m_{2^+}/\sqrt{\sigma}|_{L_s\to\infty} \sim 6.5$ so that we need $l\sqrt{\sigma} > 3.25$, which corresponds to $L_s > 24$. In this case, we choose $l\sqrt{\sigma} = 3.7$. We list these $l\sqrt{\sigma}$ values for $SO(N \geq 6)$ in Table 4.2. These values also ensure that the corrections from glueball emission are negligible. For $SO(4)$, its Lie algebra equivalences suggest that we need to adapt our approach. We know that $SU(2) \times SU(2)$ and $SO(4)$ share a common Lie algebra. Hence, for the cross product group $SU(2) \times SU(2)$, we expect a contribution from each $SU(2)$ group to the string tension so that $\sigma|_{SO(4)} = \sigma|_{SU(2)\times SU(2)} = 2\,\sigma|_{SU(2)}$. Hence, we expect that

$$\left.\frac{m_P}{\sqrt{\sigma}}\right|_{SO(4)} = l\sqrt{\sigma}|_{SO(4)} = \left.l\sqrt{2\sigma}\right|_{SU(2)} = \left.\frac{\sqrt{2}m_P}{\sqrt{\sigma}}\right|_{SU(2)} \tag{4.4}$$

Hence, to avoid finite size corrections from torelon mixing, (4.3) implies that we need

$$l\sqrt{\sigma}|_{SO(4)} > \frac{1}{\sqrt{2}} \frac{m_{2^{++}}}{\sqrt{\sigma}}\Big|_{SU(2)} \tag{4.5}$$

Since the $SU(2)$ 2^{++} mass is $m_{2^{++}}/\sqrt{\sigma} = 7.81(6)$ [33], this indicates that glueball-torelon mixing occurs at $l\sqrt{\sigma} \sim 5.5$ in $SO(4)$. Since we are less protected from this mixing at lower N, we choose $l\sqrt{\sigma} = 7.0$ in $SO(4)$. Finally, we note that torelon mixing could affect excited states such as 2^{+*}. It is possible that there are $P = -$ torelon states in the mass spectrum, and we would need to extend the operator basis to include $P = \pm$ torelon operators to exclude this case explicitly [37]. However, we note that torelon operators made from straight flux loops are intrinsically $P = +$, as they are parity invariant. Hence, negative parity flux loops are much heavier since we need to add additional excitations to create operators that project on to $P = -$ states.

4.3 Continuum limits

4.3.1 Methodology

We can now calculate the continuum limits. For a glueball state with quantum numbers J^P, we use the appropriate operator and evaluate this on the lattice. We then use the variational method to calculate correlation functions before applying exponential fits to obtain mass estimates (in lattice units). We also calculate the Polyakov loop mass for the same coupling to obtain the string tension and then express the glueball mass in string tension units $m_G/\sqrt{\sigma}$ since the string tension is the most accurate quantity we calculate. We could instead use the coupling g^2 or another mass m'_G.

After calculating masses on different volumes, we can obtain the continuum limit by taking the limit $a \to 0$. Since we consider the ratio between two masses, we expect the leading correction to be $\mathcal{O}(a^2)$ [1]. Hence, for some constant c,

$$\frac{m_G}{\sqrt{\sigma}}(a) = \frac{m_G}{\sqrt{\sigma}}(a=0) + ca^2\sigma + \cdots \tag{4.6}$$

4.3.2 $SO(4)$

For the $SO(4)$ theory, we calculate masses for β values from 11.0 to 18.7. Here, we set $l\sqrt{\sigma} \sim 7.0$. We list the glueball masses am_G and Polyakov loop masses am_P in Table 4.3.

We find that the errors for the 0^{+***} and 0^{+****} masses for $\beta = 11.0$ are large compared to other values so we choose to discard this data for the 0^{+***} and 0^{+****} continuum extrapolations. We apply the linear extrapolation (4.6) to the data to obtain the continuum limits. We display the

continuum extrapolations in Figure 4.3. We list the continuum values, extrapolation range, and extrapolation $\bar{\chi}^2_{\text{dof}}$ in Table 4.4. We see that the fits are good with low $\bar{\chi}^2_{\text{dof}}$.

There is a clear mass hierarchy of 0^+ states up to the fourth excited state. The third and fourth excited 0^+ states appear to be degenerate. The $1^\pm$, $2^\pm$, and $2^{\pm *}$ states also seem to be degenerate as we would expect by parity doubling.

4.3.3 $SO(6)$

For the $SO(6)$ theory, we calculate masses for β values from 23.0 to 46.0, setting $l\sqrt{\sigma} \sim 4.5$. We list the glueball masses am_G and Polyakov loop masses am_P in Table 4.5.

We find that the errors for $\beta = 23.0$ are large compared to other volumes, especially for heavier masses, so we choose to discard this data for the continuum extrapolations. We apply the linear extrapolation (4.6) to the remaining data to obtain the continuum limits. We display the continuum extrapolations in Figure 4.4. We list the continuum values and extrapolation $\bar{\chi}^2_{\text{dof}}$ in Table 4.6. We see that the fits are good with low $\bar{\chi}^2_{\text{dof}}$. Despite the large errors for $\beta = 23.0$, we see that the data agrees with the extrapolations.

There is a clear mass hierarchy of 0^+ states up to the fourth excited state. Here, the 0^{+****} and 0^- states appear to be degenerate. This may imply that the states are actually $4^\pm$ states and that we see parity doubling. Previous papers on the $SU(N)$ mass spectrum [38] showed that the lightest 0^- state was actually the 4^- state, so our results seem to agree with the $SU(N)$ case. The $1^\pm$, $2^\pm$, and $2^{\pm *}$ states also seem to be degenerate as we would expect by parity doubling.

4.3.4 $SO(7)$

For the $SO(7)$ theory, we calculate masses for β values from 35.0 to 70.0, setting $l\sqrt{\sigma} \sim 4.2$. We list the glueball masses am_G and Polyakov loop masses am_P in Table 4.7. For $SO(7)$, there is no $\mathbb{Z}_2$ symmetry to prevent a flux loop interacting with the vacuum so that this may allow a non-zero Polyakov loop vacuum expectation value $\langle l_P \rangle$. However, our calculations indicate that $\langle l_P \rangle = 0$ so there are no correction terms arising from mixing with Polyakov loops.

We find that the errors for the $1^\pm$ masses for $\beta = 35.0$ are large compared to other values so we choose to discard this data for the $1^\pm$ continuum extrapolations. We apply the linear extrapolation (4.6) to the remaining data to obtain the continuum limits. We display the continuum extrapolations in Figure 4.5. We list the continuum values, extrapolation range, and extrapolation $\bar{\chi}^2_{\text{dof}}$ in Table 4.8. We see that the fits are good with low $\bar{\chi}^2_{\text{dof}}$.

There is a clear mass hierarchy of 0^+ states up to the fourth excited state. We note that the second and third excited 0^+ states have very similar masses, which indicates a possible degeneracy. Again, the 0^{+****} and 0^- states appear to be degenerate implying they may be the degenerate $4^\pm$ states. The $1^\pm$, $2^\pm$, and $2^{\pm *}$ states also seem to be degenerate as we would expect by parity doubling.

4.3.5 $SO(8)$, $SO(12)$, and $SO(16)$

For the $SO(8)$ theory, we calculate masses for β values from 51.0 to 105.0, setting $l\sqrt{\sigma} \sim 3.7$. For the $SO(12)$ theory, we calculate masses for β values from 132.0 to 250.0, setting $l\sqrt{\sigma} \sim 3.5$. For the $SO(16)$ theory, we calculate masses for β values from 302.0 to 512.0, setting $l\sqrt{\sigma} \sim 3.5$. We list the glueball masses am_G and Polyakov loop masses am_P for $SO(8)$ in Table 4.9, $SO(12)$ in Table 4.11, and $SO(16)$ in Table 4.13.

Again, we find that the errors for some masses are large compared to other values so we choose to discard this data for the continuum extrapolations. For $SO(8)$ this applies to all data for $\beta = 51.0$, for $SO(12)$ this applies to all data for $\beta = 132.0$ except for the 0^+, 0^{+*},and $2^\pm$ states, and for $SO(16)$ this applies to all data for $\beta = 302.0$. We apply the linear extrapolation (4.6) to the remaining data to obtain the continuum limits. We display the continuum extrapolations for $SO(8)$ in Figure 4.6, for $SO(12)$ in Figure 4.7, and for $SO(16)$ in Figure 4.8. We list the continuum values, extrapolation range, and extrapolation $\bar{\chi}^2_{\text{dof}}$ for $SO(8)$ in Table 4.10, for $SO(12)$ in Table 4.12, and for $SO(16)$ in Table 4.14. We see that the fits are good with low $\bar{\chi}^2_{\text{dof}}$.

In these three cases, there is a clear mass hierarchy for 0^+ states up to the fourth excited state although we again see that occasionally the second and third excited 0^+ states have very similar masses, which indicates a possible degeneracy. Again, the 0^{+****} and 0^- states appear to be degenerate implying they may be the degenerate $4^\pm$ states. The $1^\pm$, $2^\pm$, and $2^{\pm *}$ states also seem to be degenerate as we would expect by parity doubling.

4.4 Large-N limits

We can now calculate the mass spectra in the $SO(N)$ large-N limit. Given 't Hooft's argument that we explained previously, we expect the physics of $SO(N)$ gauge theories to approach a large-N limit if we hold the 't Hooft coupling g^2N, or equivalently the string tension $\sqrt{\sigma}$ constant. Hence, we expect $m_G/\sqrt{\sigma}$ to converge to a large-N limit.

$$\lim_{N\to\infty}\frac{m_G}{\sqrt{\sigma}} = \frac{m_G}{\sqrt{\sigma}}\bigg|_{SO(N\to\infty)} \tag{4.7}$$

Furthermore, if we apply 't Hooft's $1/N$ argument that we explained previously, we expect the leading correction to this limit at finite N to be $\mathcal{O}(1/N)$.

$$\frac{m_G}{\sqrt{\sigma}}\bigg|_{SO(N\to\infty)} = \frac{m_G}{\sqrt{\sigma}} + \frac{c_1}{N} \tag{4.8}$$

for a constant c_1.

We list the $SO(N)$ mass spectra in Table 4.15. We extrapolate the $SO(2\tilde{N})$ values to obtain the large-$\tilde{N}$ limits because we will later compare this to the large-$\tilde{N}$ limits of $SU(\tilde{N})$ gauge theories. We next decide how to apply extrapolation fits to the data. We know that the next correction term in (4.8) is a quadratic term in $1/N^2$ so we need to decide how far the linear fit is suitable. To do this, we consider linear fits to selected $SO(N)$ data for $\tilde{N} \geq 2$ and $\tilde{N} \geq 3$ and a quadratic fit for $\tilde{N} \geq 2$. We consider the lowest masses since they are the most accurate and we list the large-$\tilde{N}$ extrapolations in Table 4.16. We see that the fits all have low $\bar{\chi}^2_{\text{dof}}$. Most large-$\tilde{N}$ values from the $\tilde{N} \geq 3$ linear fit are closer to those of the quadratic fit than the $\tilde{N} \geq 2$ linear fit. The 2^+ mass from the quadratic fit is about one standard deviation from the $\tilde{N} \geq 3$ linear fit value whereas it is 1.5σ is from the $\tilde{N} \geq 2$ linear fit value. The $\tilde{N} \geq 3$ linear fit errors are larger than the $\tilde{N} \geq 2$ linear fit but reflect the $\mathcal{O}(1/N^2)$ correction. Finally, we note that some of the heavier $SO(4)$ masses such as the $1^\pm$ and 0^{+****} states are inconsistent with the $\tilde{N} \geq 3$ linear fit, which may indicate significant $\mathcal{O}(1/\tilde{N}^2)$ corrections for the $SO(4)$ data. We therefore choose to use the $\tilde{N} \geq 3$ linear fit for the large-$\tilde{N}$ extrapolation. We also note that the good agreement between the $\tilde{N} \geq 3$ linear extrapolation and quadratic extrapolation shows that we can choose the $\mathcal{O}(1/N)$ linear correction in (4.8) to minimise the fit errors. We display the plot of these large-$\tilde{N}$ extrapolations in Figure 4.9, and list the resulting $SO(2\tilde{N} \to \infty)$ values in Table 4.17. We see that these fits are good with low $\bar{\chi}^2_{\text{dof}}$.

We see that the apparent degeneracies of the mass spectra at finite $SO(N)$ carry through to the large-N limit. We see that the 0^{+****} and 0^- states are degenerate, which we suspect are actually $4^\pm$ states, consistent with the $D = 2+1$ $SU(N)$ mass spectrum [38]. The $1^\pm$, $2^\pm$, and $2^{\pm *}$ states are degenerate as we expect due to parity doubling. We also see that the 0^{+**} and 0^{+***} seem to be degenerate. Finally, we see in Figure 4.9 that the $SO(7)$ values agree well with the large-N extrapolations.

4.5 Equivalences between $SO(N)$ and $SU(N)$ gauge theories

4.5.1 Lie algebra equivalences

We know that $SO(4)$ and $SU(2) \times SU(2)$ so we could ask how the mass spectrum compares between $SO(4)$ and $SU(2)$. As we have seen previously, for the cross product group $SU(2) \times SU(2)$, we expect a contribution from each $SU(2)$ group to the string tension so that $\sigma|_{SO(4)} = 2\,\sigma|_{SU(2)}$. Hence, we expect that the $SO(4)$ and $SU(2)$ mass spectra are related by

$$\left.\frac{m_G}{\sqrt{\sigma}}\right|_{SO(4)} = \frac{1}{\sqrt{2}} \left.\frac{m_G}{\sqrt{\sigma}}\right|_{SU(2)} \tag{4.9}$$

We can compare the $SO(4)$ and $SU(2)$ mass spectra in the appropriate string tension units [2, 33]. We list these values in Table 4.18. We see that the lighter masses such as the $0^{\pm}$ and $2^{\pm}$ states agree within errors consistent with (4.9) although there are greater differences for heavier masses. This may indicate that we should reexamine these values in the future. However, the agreement between the lighter masses is consistent with our expectation (4.9).

We know that $SO(6)$ and $SU(4)$ share a common Lie algebra so we could ask how the mass spectrum compares between $SO(6)$ and $SU(4)$. As we have seen previously, the $SO(6)$ fundamental string tension is equivalent to the $SU(4)$ $k = 2A$ string tension. To compare between the $SO(6)$ and $SU(4)$ mass spectra, which are both given in terms of their fundamental string tensions, we use the ratio of the $SU(4)$ $k = 2A$ and fundamental string tensions in $D = 2{+}1$ $\sigma_{2A}/\sigma_f|_{SU(4)} = 1.355(9)$ [9]. Hence, we expect to relate the $SO(6)$ and $SU(4)$ mass spectra by

$$\left.\frac{m_G}{\sqrt{\sigma_f}}\right|_{SO(6)} = \left.\frac{m_G}{\sqrt{\sigma_{2A}}}\right|_{SU(4)} = \sqrt{1.355}\left.\frac{m_G}{\sqrt{\sigma_f}}\right|_{SU(4)} \tag{4.10}$$

We can compare the $SO(6)$ and $SU(4)$ mass spectra in the appropriate string tension units [2, 33]. We list these values in Table 4.19. We see that most of these values agree within errors. However, there are some values that do not agree within errors such as the 0^{+**} and 1^{+} states. This may indicate that we should reexamine these values in the future. In particular, we note that the $SU(4)$ values do not show $J = 1$ parity doubling whereas the $SO(6)$ values do. Nonetheless, the agreement over many values is consistent with our expectation (4.10).

4.5.2 Large-N orbifold equivalence

We now compare the large-N limits of the $SO(2\tilde{N})$ and $SU(\tilde{N})$ mass spectra. From the large-N equivalence, we expect that

$$\left.\frac{m_G}{\sqrt{\sigma}}\right|_{SO(2\tilde{N}\to\infty)} = \left.\frac{m_G}{\sqrt{\sigma}}\right|_{SU(\tilde{N}\to\infty)} \tag{4.11}$$

for all mass spectrum values $m_G/\sqrt{\sigma}$.

Since the orbifold equivalence only holds in a common sector of states that are charge conjugation $C = +$, we only compare $C = +$ states between the two gauge theories. We list the large-N mass spectrum in Table 4.20 [2, 33]. We see that many values agree within one standard deviation. We note that the 0^{+*} values do not agree within errors so this may indicate that we should reexamine this value in the future. Nonetheless, the agreement over many values verifies our expectation from the large-N orbifold equivalence (4.11).

4.6 Data

$L_s^2 L_t$	$12^2 36$	$16^2 36$	$20^2 36$	$24^2 36$	$28^2 36$	$32^2 36$	$36^2 36$
am_P	0.135(2)	0.237(2)	0.331(2)	0.408(4)	0.483(2)	0.561(2)	0.635(2)
$l\sqrt{\sigma}$	1.492(6)	2.085(7)	2.675(7)	3.213(15)	3.751(8)	4.298(7)	4.838(8)
0^+	0.247(10)	0.447(5)	0.494(9)	0.492(9)	0.506(2)	0.514(4)	0.511(3)
0^{+*}	0.252(11)	0.508(26)	0.675(17)	0.737(16)	0.769(4)	0.789(8)	0.773(7)
0^{+**}	0.489(29)	0.558(23)	0.836(38)	0.935(21)	0.968(30)	1.021(14)	0.994(11)
0^{+***}	0.482(29)	0.854(29)	0.883(19)	0.996(33)	0.992(10)	1.021(6)	1.028(12)
0^{+****}	0.523(25)	0.947(7)	1.005(20)	1.091(35)	1.098(11)	1.124(18)	1.088(17)
2^+	0.228(6)	0.385(31)	0.874(11)	0.875(8)	0.859(7)	0.857(8)	0.850(8)
2^{+*}	0.668(34)	0.681(46)	0.899(18)	1.031(26)	1.058(10)	1.040(15)	1.054(13)
2^-	0.471(10)	0.769(11)	0.854(12)	0.892(21)	0.852(5)	0.837(17)	0.869(4)
2^{-*}	0.783(19)	0.824(11)	1.035(24)	1.001(25)	1.052(8)	1.073(15)	1.071(15)
0^-	1.124(7)	1.126(24)	1.117(22)	1.134(38)	1.095(11)	1.110(7)	1.118(19)
1^+	1.308(33)	1.322(36)	1.277(36)	1.260(43)	1.252(14)	1.280(20)	1.265(23)
1^-	1.286(26)	1.225(24)	1.274(33)	1.295(48)	1.270(12)	1.237(25)	1.246(20)

Table 4.1: $SO(8)$ glueball am_G and Polyakov loop masses am_P at fixed $\beta = 84$.

N	$l\sqrt{\sigma}$
4	7.0
6	4.5
7	4.2
8	3.7
12	3.5
16	3.5

Table 4.2: Approximate values of $l\sqrt{\sigma}$ for $SO(N)$ mass spectrum calculations.

$L_s^2 L_t$	$34^2 42$	$38^2 46$	$44^2 52$	$48^2 56$	$54^2 62$	$62^2 70$
β	11.0	12.2	13.7	15.1	16.5	18.7
am_P	1.513(8)	1.290(7)	1.144(4)	0.993(4)	0.895(8)	0.791(5)
$l\sqrt{\sigma}$	7.209(19)	7.039(18)	7.131(13)	6.941(13)	6.990(31)	7.039(23)
0^+	0.690(5)	0.618(1)	0.540(2)	0.480(4)	0.433(2)	0.379(2)
0^{+*}	1.045(10)	0.914(9)	0.801(3)	0.712(6)	0.640(5)	0.578(4)
0^{+**}	1.278(25)	1.151(6)	1.030(5)	0.925(11)	0.803(20)	0.736(5)
0^{+***}	1.464(46)	1.260(39)	1.099(26)	1.020(19)	0.947(7)	0.826(4)
0^{+****}	1.646(72)	1.297(42)	1.143(23)	1.028(19)	0.955(14)	0.841(12)
2^+	1.189(4)	1.018(13)	0.908(9)	0.820(6)	0.734(13)	0.645(5)
2^{+*}	1.455(11)	1.290(10)	1.091(19)	1.029(42)	0.914(13)	0.804(8)
2^-	1.186(4)	1.039(15)	0.900(9)	0.816(4)	0.738(7)	0.643(5)
2^{-*}	1.421(9)	1.244(9)	1.090(22)	0.992(19)	0.923(14)	0.804(10)
0^-	1.528(14)	1.344(11)	1.195(9)	1.043(8)	0.908(15)	0.837(10)
1^+	1.729(24)	1.409(71)	1.404(15)	1.180(26)	1.067(19)	0.968(11)
1^-	1.722(23)	1.426(68)	1.371(14)	1.176(27)	1.106(20)	0.941(11)

Table 4.3: $SO(4)$ glueball am_G and Polyakov loop masses am_P.

J^P	$m_G/\sqrt{\sigma}$	Extrapolation range	$\bar{\chi}^2_{\rm dof}$
0^+	3.36(2)	$\beta \geq 11.0$	1.72
0^{+*}	5.04(4)	$\beta \geq 11.0$	2.14
0^{+**}	6.66(7)	$\beta \geq 11.0$	0.84
0^{+***}	7.65(12)	$\beta \geq 12.2$	1.69
0^{+****}	7.71(19)	$\beta \geq 12.2$	0.39
2^+	5.70(5)	$\beta \geq 11.0$	0.95
2^{+*}	7.14(9)	$\beta \geq 11.0$	1.23
2^-	5.69(4)	$\beta \geq 11.0$	0.67
2^{-*}	7.18(10)	$\beta \geq 11.0$	1.51
0^-	7.31(8)	$\beta \geq 11.0$	2.88
1^+	8.64(12)	$\beta \geq 11.0$	4.39
1^-	8.48(12)	$\beta \geq 11.0$	2.32

Table 4.4: $SO(4)$ continuum glueball masses in string tension units $m_G/\sqrt{\sigma}$, extrapolation range, and extrapolation $\bar{\chi}^2_{\rm dof}$.

$L_s^2 L_t$	$16^2 24$	$20^2 28$	$24^2 32$	$28^2 36$	$32^2 40$	$36^2 44$
β	23.0	28.0	33.0	37.0	41.0	46.0
am_P	1.272(14)	0.980(2)	0.794(3)	0.715(2)	0.645(3)	0.562(2)
$l\sqrt{\sigma}$	4.570(25)	4.486(4)	4.425(7)	4.532(6)	4.602(9)	4.557(8)
0^+	1.050(3)	0.818(2)	0.671(3)	0.589(2)	0.530(4)	0.457(3)
0^{+*}	1.586(3)	1.243(5)	1.023(8)	0.890(9)	0.795(13)	0.695(7)
0^{+**}	2.003(7)	1.553(15)	1.283(12)	1.139(8)	1.009(10)	0.891(19)
0^{+***}	2.042(59)	1.625(22)	1.375(20)	1.183(10)	1.062(10)	0.920(19)
0^{+****}	2.248(12)	1.733(32)	1.490(23)	1.227(43)	1.134(12)	1.014(7)
2^+	1.716(19)	1.373(9)	1.136(10)	1.008(6)	0.892(6)	0.788(6)
2^{+*}	2.040(60)	1.651(23)	1.381(16)	1.225(11)	1.099(12)	0.966(7)
2^-	1.758(19)	1.372(11)	1.132(9)	1.000(5)	0.875(6)	0.777(4)
2^{-*}	2.118(62)	1.665(25)	1.393(16)	1.207(11)	1.094(11)	0.970(22)
0^-	2.258(10)	1.781(31)	1.491(24)	1.238(50)	1.148(15)	1.003(9)
1^+	2.718(231)	1.916(52)	1.689(41)	1.488(18)	1.327(17)	1.167(8)
1^-	2.354(163)	2.009(54)	1.652(35)	1.474(20)	1.328(16)	1.158(10)

Table 4.5: $SO(6)$ glueball am_G and Polyakov loop masses am_P.

J^P	$m_G/\sqrt{\sigma}$	$\bar{\chi}^2_{\rm dof}$
0^+	3.63(2)	1.69
0^{+*}	5.49(6)	0.16
0^{+**}	7.12(9)	0.14
0^{+***}	7.41(11)	0.85
0^{+****}	8.08(10)	1.76
2^+	6.29(5)	0.25
2^{+*}	7.78(9)	0.09
2^-	6.14(5)	1.13
2^{-*}	7.67(13)	0.77
0^-	7.91(11)	0.72
1^+	9.48(13)	0.83
1^-	9.30(15)	0.34

Table 4.6: $SO(6)$ continuum glueball masses in string tension units $m_G/\sqrt{\sigma}$, and extrapolation $\bar{\chi}^2_{\rm dof}$ for $\beta \geq 28.0$.

$L_s^2 L_t$	$16^2 24$	$20^2 28$	$24^2 32$	$28^2 36$	$32^2 40$	$36^2 44$
β	35.0	42.0	49.0	57.0	64.0	70.0
am_P	1.071(5)	0.857(2)	0.714(2)	0.592(2)	0.525(1)	0.483(2)
$l\sqrt{\sigma}$	4.204(10)	4.204(4)	4.204(6)	4.137(5)	4.163(3)	4.234(7)
0^+	0.980(3)	0.786(2)	0.658(2)	0.552(2)	0.484(2)	0.440(1)
0^{+*}	1.478(15)	1.198(8)	1.002(9)	0.833(6)	0.733(2)	0.677(2)
0^{+**}	1.930(44)	1.512(27)	1.262(14)	1.073(8)	0.953(6)	0.873(6)
0^{+***}	1.961(66)	1.546(23)	1.301(15)	1.123(8)	0.978(5)	0.888(5)
0^{+****}	2.039(80)	1.667(30)	1.381(24)	1.187(9)	1.052(7)	0.956(9)
2^+	1.623(19)	1.310(13)	1.096(9)	0.933(5)	0.823(3)	0.750(4)
2^{+*}	1.977(70)	1.594(24)	1.356(15)	1.154(11)	1.000(4)	0.912(6)
2^-	1.628(29)	1.293(10)	1.103(8)	0.927(4)	0.824(4)	0.743(4)
2^{-*}	2.040(70)	1.573(24)	1.330(16)	1.125(12)	1.011(4)	0.924(6)
0^-	1.986(96)	1.655(27)	1.389(14)	1.202(13)	1.044(5)	0.950(8)
1^+	2.313(186)	1.969(58)	1.649(31)	1.375(9)	1.184(23)	1.101(9)
1^-	2.158(146)	1.904(60)	1.604(32)	1.383(12)	1.195(8)	1.089(10)

Table 4.7: $SO(7)$ glueball am_G and Polyakov loop masses am_P.

J^P	$m_G/\sqrt{\sigma}$	Extrapolation range	$\bar{\chi}^2_{\rm dof}$
0^+	3.74(1)	$\beta \geq 35.0$	1.21
0^{+*}	5.70(2)	$\beta \geq 35.0$	5.77
0^{+**}	7.40(6)	$\beta \geq 35.0$	1.46
0^{+***}	7.61(6)	$\beta \geq 35.0$	1.02
0^{+****}	8.20(8)	$\beta \geq 35.0$	0.20
2^+	6.40(3)	$\beta \geq 35.0$	0.39
2^{+*}	7.76(6)	$\beta \geq 35.0$	1.02
2^-	6.38(4)	$\beta \geq 35.0$	0.83
2^{-*}	7.91(6)	$\beta \geq 35.0$	1.63
0^-	8.17(8)	$\beta \geq 35.0$	0.63
1^+	9.30(15)	$\beta \geq 42.0$	0.74
1^-	9.26(14)	$\beta \geq 42.0$	1.22

Table 4.8: $SO(7)$ continuum glueball masses in string tension units $m_G/\sqrt{\sigma}$, extrapolation range, and extrapolation $\bar{\chi}^2_{\rm dof}$.

$L_s^2 L_t$	$16^2 24$	$20^2 28$	$24^2 32$	$28^2 36$	$32^2 40$	$36^2 44$
β	51.0	62.0	73.0	84.0	94.0	105.0
am_P	0.872(2)	0.689(1)	0.567(2)	0.483(2)	0.431(2)	0.383(1)
$l\sqrt{\sigma}$	3.806(5)	3.783(3)	3.760(5)	3.751(8)	3.784(7)	3.783(6)
0^+	0.901(4)	0.716(2)	0.595(3)	0.506(2)	0.449(2)	0.397(2)
0^{+*}	1.370(3)	1.084(8)	0.914(3)	0.769(4)	0.690(4)	0.605(5)
0^{+**}	1.681(39)	1.387(17)	1.132(10)	0.968(30)	0.870(6)	0.767(4)
0^{+***}	1.819(51)	1.433(22)	1.175(12)	0.992(10)	0.898(8)	0.801(5)
0^{+****}	1.861(69)	1.562(29)	1.281(16)	1.098(11)	0.946(19)	0.856(14)
2^+	1.502(20)	1.209(11)	1.007(9)	0.859(7)	0.756(5)	0.683(3)
2^{+*}	1.748(58)	1.434(27)	1.197(12)	1.058(10)	0.931(7)	0.823(12)
2^-	1.491(20)	1.202(12)	0.994(7)	0.852(5)	0.746(7)	0.665(6)
2^{-*}	1.861(55)	1.433(27)	1.206(16)	1.052(8)	0.931(15)	0.836(14)
0^-	1.760(69)	1.537(36)	1.249(14)	1.095(11)	0.946(23)	0.862(11)
1^+	2.171(130)	1.790(49)	1.456(23)	1.252(14)	1.113(8)	0.984(7)
1^-	2.293(162)	1.760(61)	1.469(20)	1.270(12)	1.114(10)	0.993(8)

Table 4.9: $SO(8)$ glueball am_G and Polyakov loop masses am_P.

J^P	$m_G/\sqrt{\sigma}$	$\bar{\chi}^2_{\rm dof}$
0^+	3.79(2)	0.47
0^{+*}	5.83(5)	3.87
0^{+**}	7.34(7)	0.91
0^{+***}	7.64(8)	1.87
0^{+****}	8.07(16)	0.32
2^+	6.50(5)	1.42
2^{+*}	8.08(11)	1.08
2^-	6.32(7)	0.13
2^{-*}	8.12(14)	0.09
0^-	8.27(15)	0.95
1^+	9.39(13)	0.24
1^-	9.50(14)	0.14

Table 4.10: $SO(8)$ continuum glueball masses in string tension units $m_G/\sqrt{\sigma}$, and extrapolation $\bar{\chi}^2_{\rm dof}$ for $\beta \geq 62.0$.

$L_s^2 L_t$	$16^2 24$	$20^2 28$	$24^2 32$	$28^2 36$	$32^2 40$	$36^2 44$
β	132.0	155.0	175.0	200.0	225.0	250.0
am_P	0.724(3)	0.626(2)	0.576(1)	0.497(3)	0.440(3)	0.395(2)
$l\sqrt{\sigma}$	3.481(7)	3.612(6)	3.789(4)	3.800(10)	3.821(11)	3.842(7)
0^+	0.849(6)	0.704(4)	0.619(2)	0.529(4)	0.470(7)	0.413(3)
0^{+*}	1.269(18)	1.081(12)	0.944(7)	0.813(8)	0.721(3)	0.646(3)
0^{+**}	1.712(77)	1.362(10)	1.207(5)	1.050(13)	0.920(9)	0.813(6)
0^{+***}	1.678(64)	1.407(27)	1.228(19)	1.053(14)	0.925(4)	0.829(6)
0^{+****}	1.674(95)	1.493(53)	1.317(31)	1.171(21)	0.997(14)	0.916(10)
2^+	1.412(29)	1.187(17)	1.036(11)	0.871(10)	0.783(6)	0.708(5)
2^{+*}	1.785(71)	1.461(7)	1.284(20)	1.103(16)	0.965(12)	0.866(8)
2^-	1.460(35)	1.112(47)	1.045(4)	0.886(9)	0.787(8)	0.707(7)
2^{-*}	1.820(99)	1.456(8)	1.277(20)	1.115(6)	0.974(11)	0.873(8)
0^-	1.728(101)	1.486(44)	1.363(30)	1.158(21)	0.987(10)	0.909(7)
1^+	2.310(229)	1.672(100)	1.481(37)	1.299(26)	1.143(13)	1.021(9)
1^-	2.058(182)	1.693(82)	1.475(37)	1.295(23)	1.139(17)	1.028(10)

Table 4.11: $SO(12)$ glueball am_G and Polyakov loop masses am_P.

J^P	$m_G/\sqrt{\sigma}$	Extrapolation range	$\bar{\chi}^2_{\rm dof}$
0^+	3.90(3)	$\beta \geq 132.0$	0.73
0^{+*}	6.11(4)	$\beta \geq 132.0$	0.20
0^{+**}	7.72(8)	$\beta \geq 155.0$	1.20
0^{+***}	7.73(10)	$\beta \geq 155.0$	0.07
0^{+****}	8.67(19)	$\beta \geq 155.0$	1.04
2^+	6.61(6)	$\beta \geq 132.0$	1.45
2^{+*}	8.12(10)	$\beta \geq 132.0$	0.06
2^-	6.57(8)	$\beta \geq 155.0$	1.25
2^{-*}	8.29(8)	$\beta \geq 155.0$	0.41
0^-	8.48(15)	$\beta \geq 155.0$	2.30
1^+	9.72(21)	$\beta \geq 155.0$	0.08
1^-	9.81(22)	$\beta \geq 155.0$	0.08

Table 4.12: $SO(12)$ continuum glueball masses in string tension units $m_G/\sqrt{\sigma}$, extrapolation range, and extrapolation $\bar{\chi}^2_{\rm dof}$.

$L_s^2 L_t$	$20^2 28$	$24^2 32$	$28^2 36$	$32^2 40$	$36^2 44$
β	302.0	353.0	408.0	456.0	512.0
am_P	0.543(2)	0.463(2)	0.394(2)	0.352(1)	0.311(1)
$l\sqrt{\sigma}$	3.375(7)	3.412(7)	3.401(7)	3.437(6)	3.427(7)
0^+	0.654(9)	0.567(3)	0.483(2)	0.427(2)	0.378(2)
0^{+*}	0.961(34)	0.852(11)	0.740(3)	0.657(2)	0.579(4)
0^{+**}	1.079(69)	1.068(19)	0.959(11)	0.813(6)	0.725(5)
0^{+***}	1.233(26)	1.111(62)	0.960(5)	0.858(4)	0.757(5)
0^{+****}	1.390(37)	1.230(27)	1.073(17)	0.932(9)	0.830(7)
2^+	1.124(17)	0.935(14)	0.804(6)	0.718(6)	0.640(4)
2^{+*}	1.353(31)	1.151(26)	0.987(12)	0.869(9)	0.783(6)
2^-	1.120(17)	0.953(5)	0.806(6)	0.710(6)	0.641(5)
2^{-*}	1.387(9)	1.149(20)	1.003(12)	0.872(8)	0.795(7)
0^-	1.480(34)	1.227(26)	1.025(12)	0.924(13)	0.819(6)
1^+	1.594(60)	1.356(32)	1.169(17)	1.026(10)	0.911(21)
1^-	1.693(74)	1.360(30)	1.173(17)	1.044(13)	0.905(21)

Table 4.13: $SO(16)$ glueball am_G and Polyakov loop masses am_P.

J^P	$m_G/\sqrt{\sigma}$	$\bar{\chi}^2_{\rm dof}$
0^+	3.95(4)	0.03
0^{+*}	6.17(8)	0.71
0^{+**}	7.53(14)	5.00
0^{+***}	8.09(15)	0.57
0^{+****}	8.70(19)	0.55
2^+	6.86(11)	0.06
2^{+*}	8.34(17)	0.55
2^-	6.65(8)	2.00
2^{-*}	8.43(17)	2.02
0^-	8.68(18)	0.86
1^+	9.55(32)	0.09
1^-	9.70(33)	0.43

Table 4.14: $SO(16)$ continuum glueball masses in string tension units $m_G/\sqrt{\sigma}$, extrapolation range, and extrapolation $\bar{\chi}^2_{\rm dof}$ for $\beta \geq 353.0$.

J^P	$SO(4)$	$SO(6)$	$SO(7)$	$SO(8)$	$SO(12)$	$SO(16)$
0^+	3.36(2)	3.63(2)	3.74(1)	3.79(2)	3.90(3)	3.95(4)
0^{+*}	5.04(4)	5.49(6)	5.70(2)	5.83(5)	6.11(4)	6.17(8)
0^{+**}	6.66(7)	7.12(9)	7.40(6)	7.34(7)	7.72(8)	7.53(14)
0^{+***}	7.65(12)	7.41(11)	7.61(6)	7.64(8)	7.73(10)	8.09(15)
0^{+****}	7.71(19)	8.08(10)	8.20(8)	8.07(16)	8.67(19)	8.70(19)
2^+	5.70(5)	6.29(5)	6.40(3)	6.50(5)	6.61(6)	6.86(11)
2^{+*}	7.14(9)	7.78(9)	7.76(6)	8.08(11)	8.12(10)	8.34(17)
2^-	5.69(4)	6.14(5)	6.38(4)	6.32(7)	6.57(8)	6.65(8)
2^{-*}	7.18(10)	7.67(13)	7.91(6)	8.12(14)	8.29(8)	8.43(17)
0^-	7.31(8)	7.91(11)	8.17(8)	8.27(15)	8.48(15)	8.68(18)
1^+	8.64(12)	9.48(13)	9.30(15)	9.39(13)	9.72(21)	9.55(32)
1^-	8.48(12)	9.30(15)	9.26(14)	9.50(14)	9.81(22)	9.70(33)

Table 4.15: Continuum $SO(N)$ glueball masses in string tension units $m_G/\sqrt{\sigma}$.

	$\tilde{N} \geq 2$ linear		$\tilde{N} \geq 3$ linear		$\tilde{N} \geq 2$ quadratic	
J^P	$m_G/\sqrt{\sigma}$	$\bar{\chi}^2_{\rm dof}$	$m_G/\sqrt{\sigma}$	$\bar{\chi}^2_{\rm dof}$	$m_G/\sqrt{\sigma}$	$\bar{\chi}^2_{\rm dof}$
0^+	4.18(3)	0.40	4.16(4)	0.49	4.13(7)	0.34
0^{+*}	6.62(5)	0.65	6.67(8)	0.61	6.70(16)	0.82
2^+	7.21(7)	1.68	7.06(11)	0.87	6.89(19)	0.99
2^-	6.99(7)	0.10	6.96(11)	0.11	6.95(18)	0.13

Table 4.16: Large-$\tilde{N}$ extrapolation fits to selected continuum $SO(2\tilde{N})$ masses in string tension units $m_G/\sqrt{\sigma}$ with extrapolation $\bar{\chi}^2_{\rm dof}$.

J^P	$m_G/\sqrt{\sigma}$	$\bar{\chi}^2_{\rm dof}$
0^+	4.16(4)	0.49
0^{+*}	6.67(8)	0.61
0^{+**}	8.12(15)	2.17
0^{+***}	8.26(18)	1.08
0^{+****}	9.06(25)	1.36
2^+	7.06(11)	0.87
2^{+*}	8.56(17)	0.68
2^-	6.96(11)	0.11
2^{-*}	8.90(18)	0.41
0^-	9.11(22)	0.09
1^+	9.68(33)	0.69
1^-	10.15(35)	0.15

Table 4.17: Large-$\tilde{N}$ extrapolation of continuum $SO(2\tilde{N})$ mass spectrum in string tension units $m_G/\sqrt{\sigma}$ for $\tilde{N} \geq 3$, and extrapolation $\bar{\chi}^2_{\rm dof}$.

J^P	$SO(4)$	$SU(2)$
0^+	3.36(2)	3.33(1)
0^{+*}	5.04(4)	4.79(5)
0^{+**}	6.66(7)	5.71(7)
2^+	5.70(8)	5.53(10)
2^-	5.69(4)	5.56(10)
0^-	7.31(8)	7.04(23)
1^+	8.64(12)	7.37(24)
1^-	8.48(12)	7.87(30)

Table 4.18: Continuum mass spectrum of $SO(4)$ and $SU(2)$ [2,33] gauge theories in the appropriate string tension units $m_G/\sqrt{\tilde{\sigma}}$ where we use the $SO(4)$ string tension and $\sqrt{\tilde{\sigma}} = 1/\sqrt{2\sigma}$ where σ is the $SU(2)$ string tension.

J^P	$SO(6)$	$SU(4)$
0^+	3.63(2)	3.64(1)
0^{+*}	5.49(6)	5.48(2)
0^{+**}	7.12(9)	6.81(8)
2^+	6.29(5)	6.16(9)
2^-	6.14(5)	5.89(17)
0^-	7.91(11)	8.00(27)
1^+	9.48(13)	8.51(34)
1^-	9.30(15)	9.32(51)

Table 4.19: Continuum mass spectrum of $SO(6)$ and $SU(4)$ [2,33] gauge theories in the appropriate string tension units $m_G/\sqrt{\tilde{\sigma}}$ where we use the fundamental $SO(6)$ string tension and the $k = 2A$ $SU(4)$ string tension.

J^P	$SO(2\tilde{N} \to \infty)$	$SU(\tilde{N} \to \infty)$
0^+	4.16(4)	4.11(2)
0^{+*}	6.67(8)	6.21(5)
0^{+**}	8.12(15)	8.35(20)
2^+	7.06(11)	6.88(6)
2^{+*}	8.56(17)	9.22(32)
2^-	6.96(11)	6.89(21)
0^-	9.11(22)	9.02(30)
1^+	9.68(33)	9.98(25)
1^-	10.15(35)	10.06(40)

Table 4.20: Large-$\tilde{N}$ extrapolation of continuum $SO(2\tilde{N})$ and $SU(\tilde{N})$ [2, 33] mass spectrum in string tension units $m_G/\sqrt{\sigma}$.

4.7 Figures

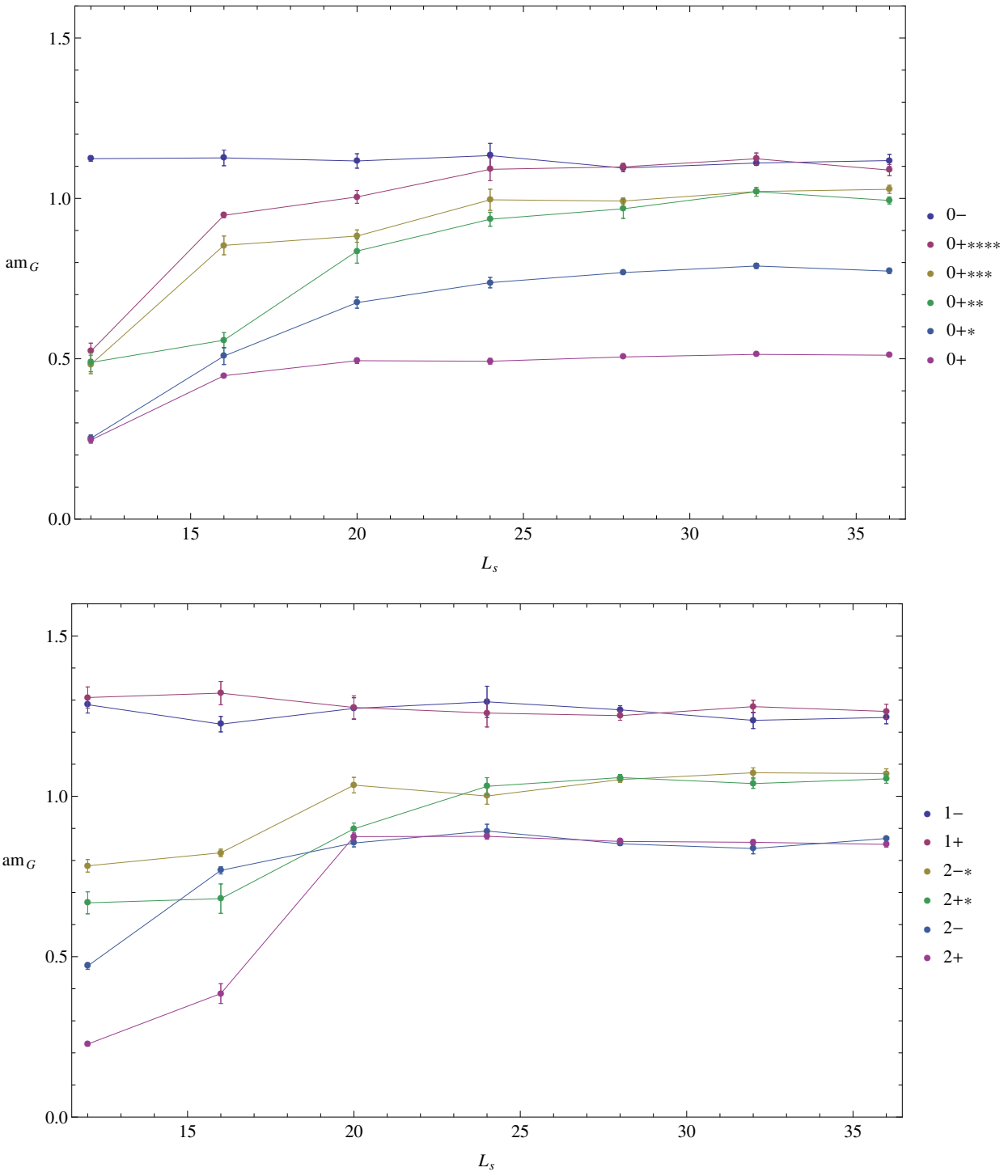

Figure 4.2: $SO(8)$ mass spectrum at different volumes $L_s^2 36$ for fixed $\beta = 84$.

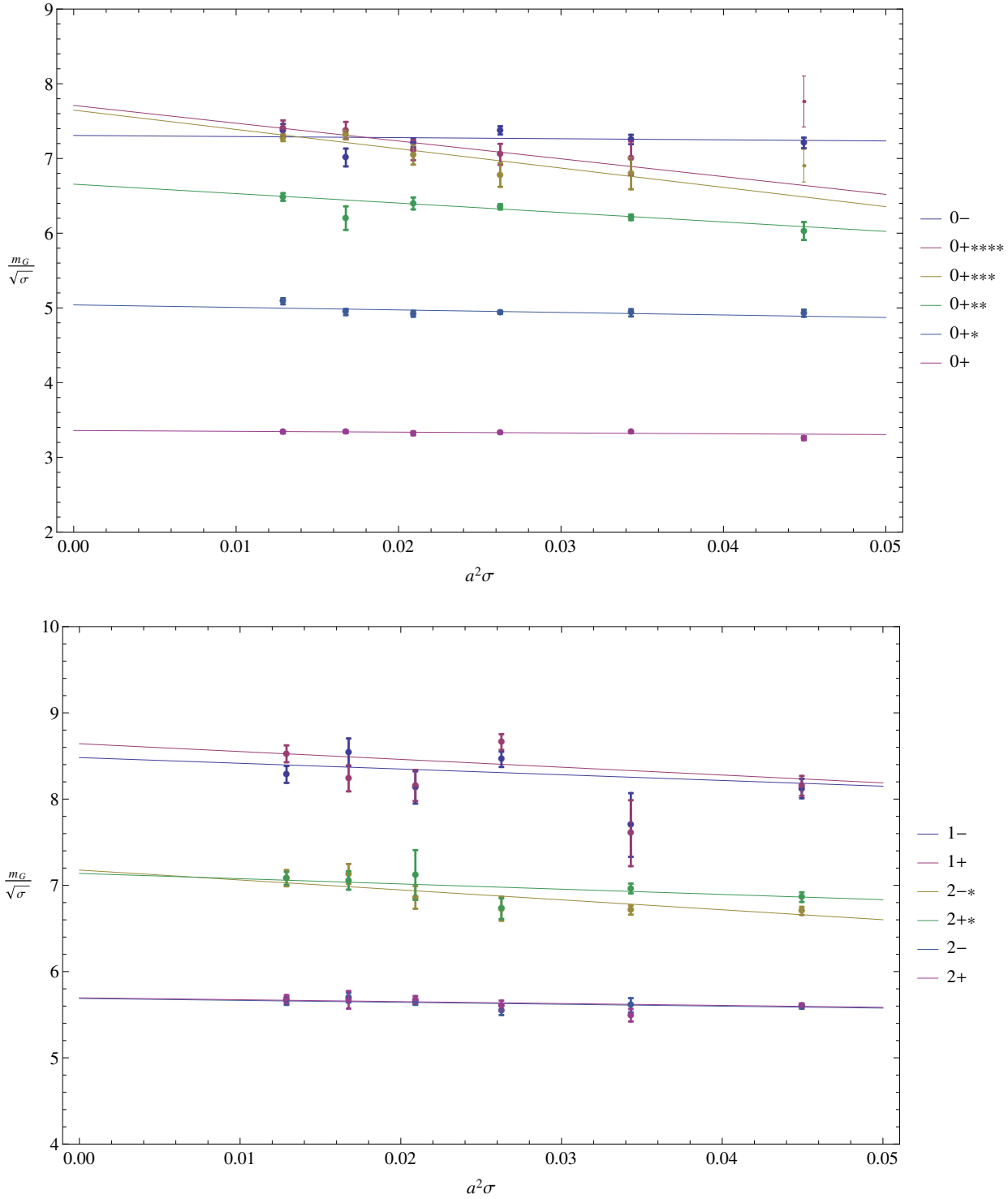

Figure 4.3: Continuum extrapolation of $SO(4)$ glueball mass spectrum in string tension units. We use only the thick style points in the extrapolations.

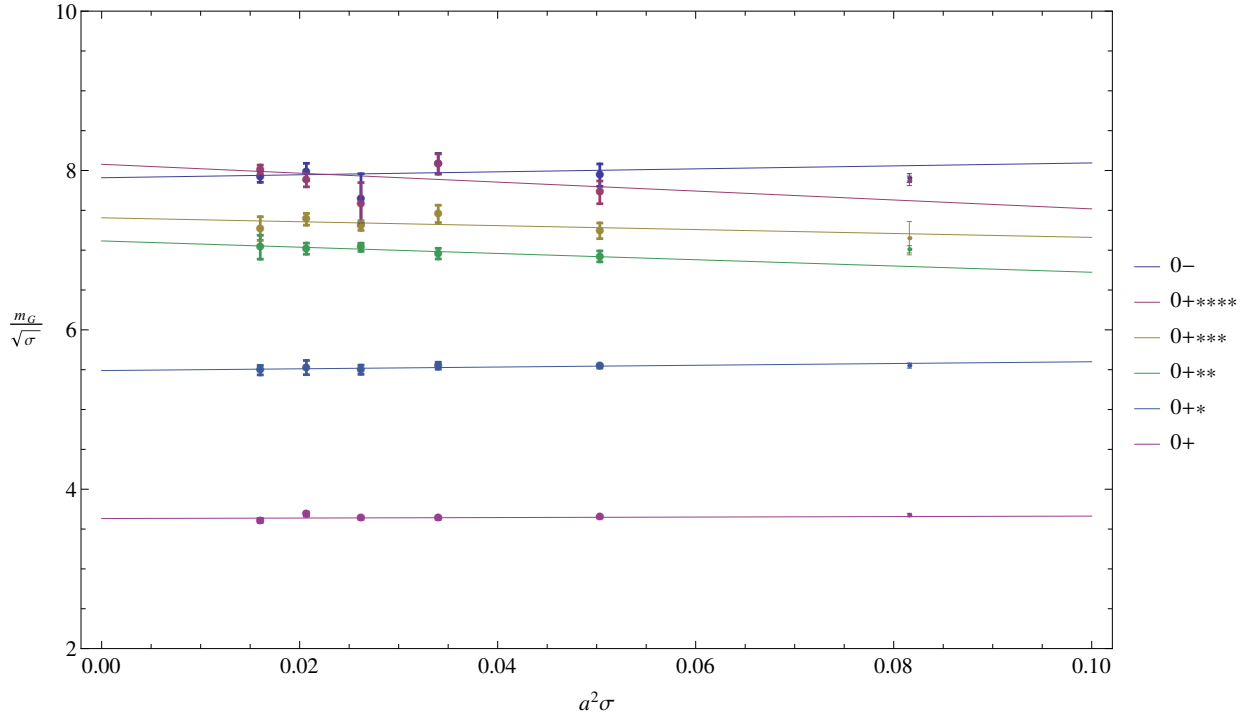

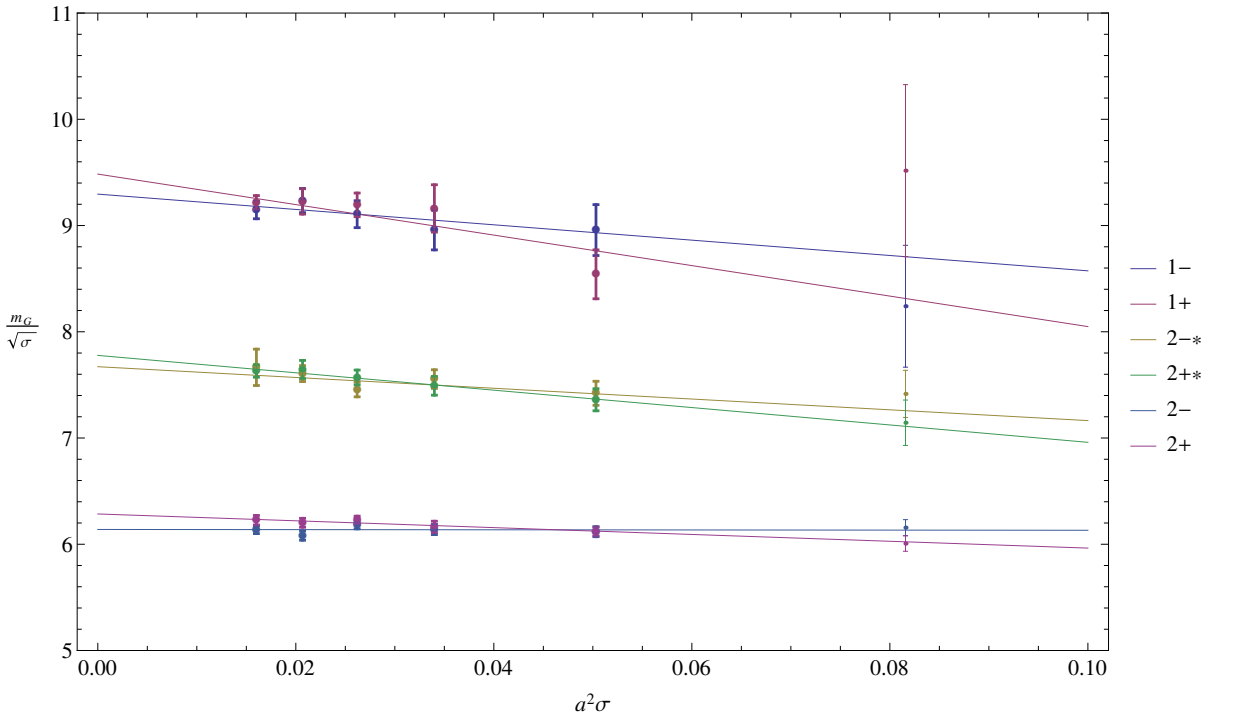

Figure 4.4: Continuum extrapolation of $SO(6)$ glueball mass spectrum in string tension units. We use only the thick style points in the extrapolations.

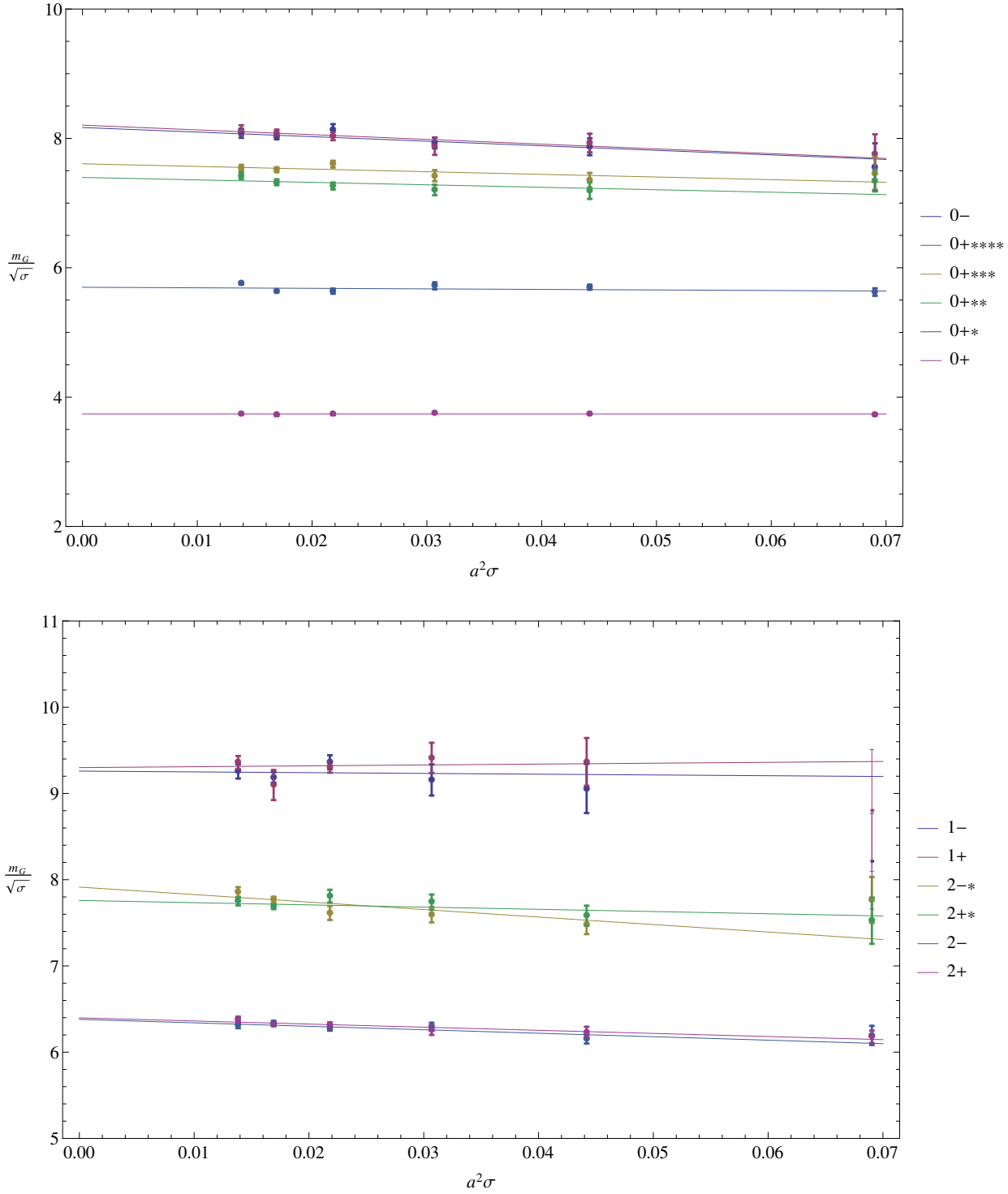

Figure 4.5: Continuum extrapolation of $SO(7)$ glueball mass spectrum in string tension units. We use only the thick style points in the extrapolations.

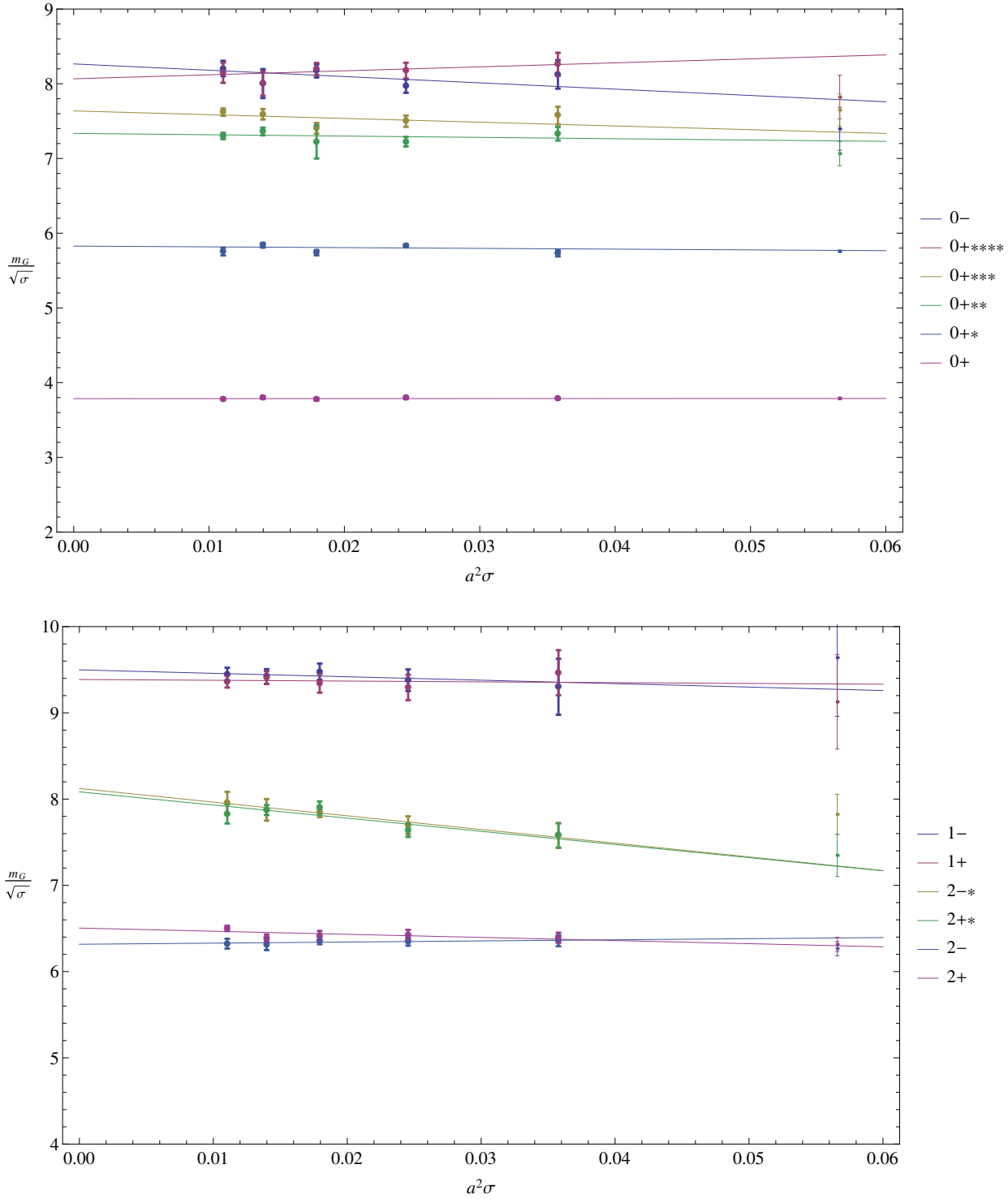

Figure 4.6: Continuum extrapolation of $SO(8)$ glueball mass spectrum in string tension units. We use only the thick style points in the extrapolations.

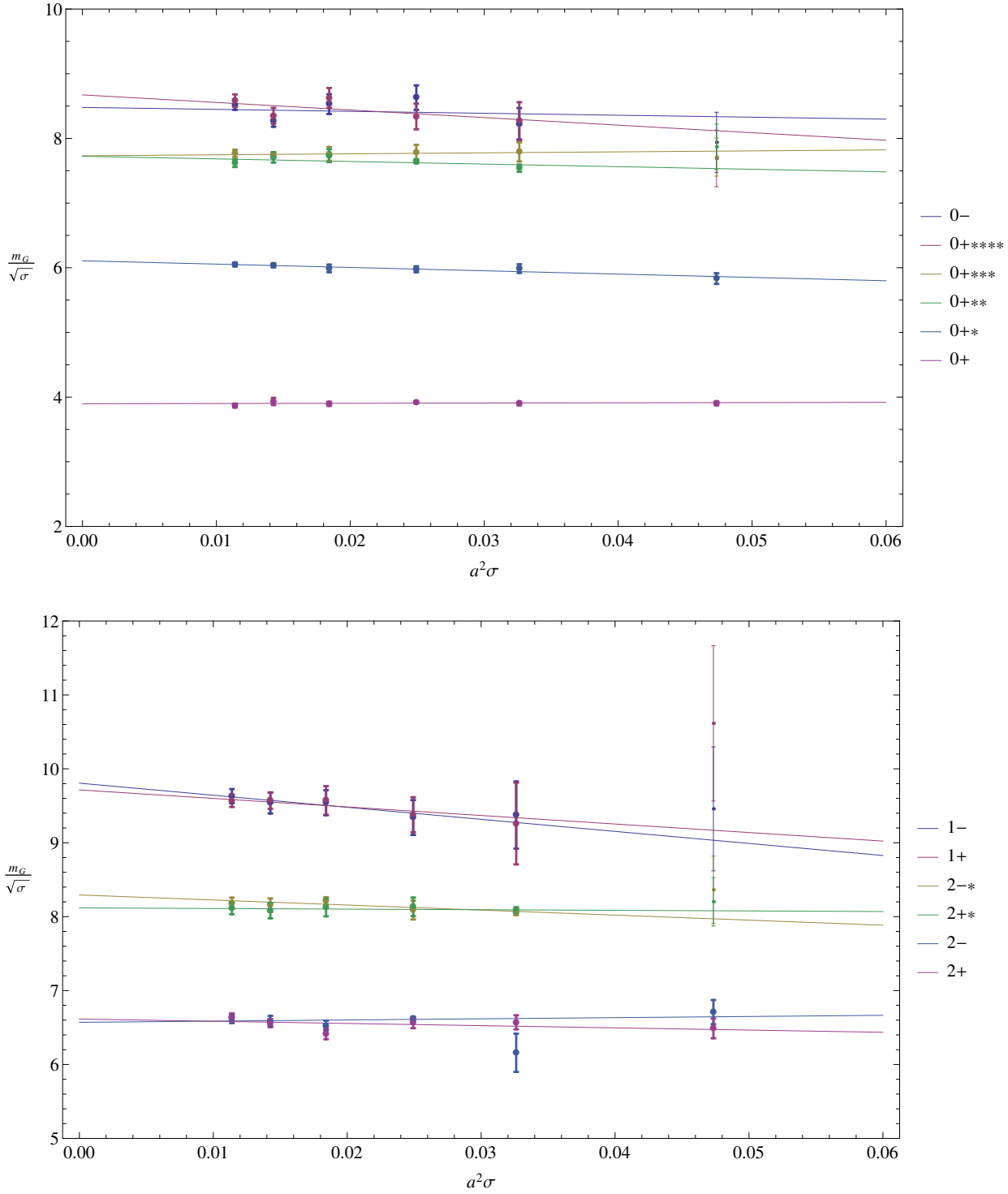

Figure 4.7: Continuum extrapolation of $SO(12)$ glueball mass spectrum in string tension units. We use only the thick style points in the extrapolations.

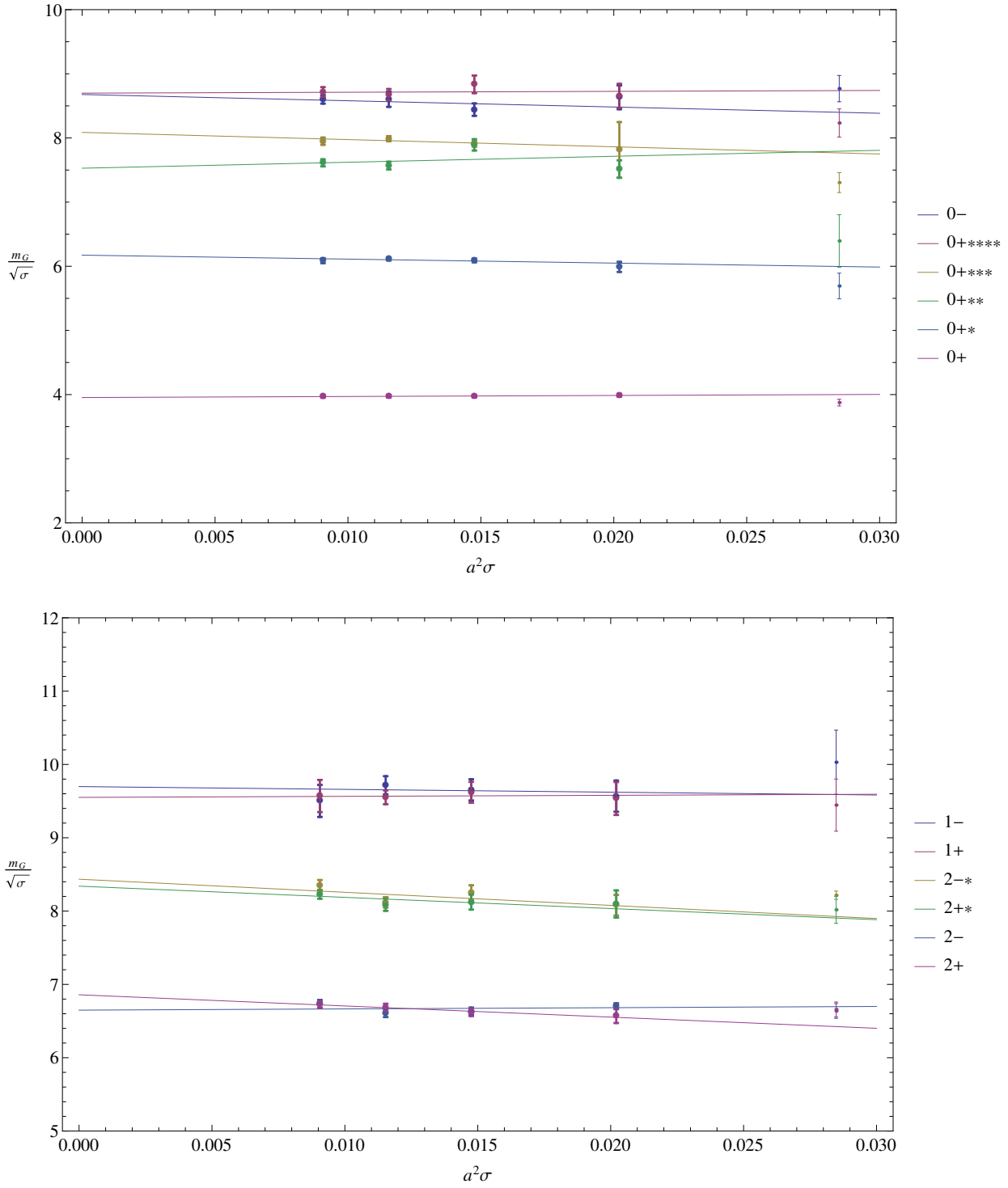

Figure 4.8: Continuum extrapolation of $SO(16)$ glueball mass spectrum in string tension units. We use only the thick style points in the extrapolations.

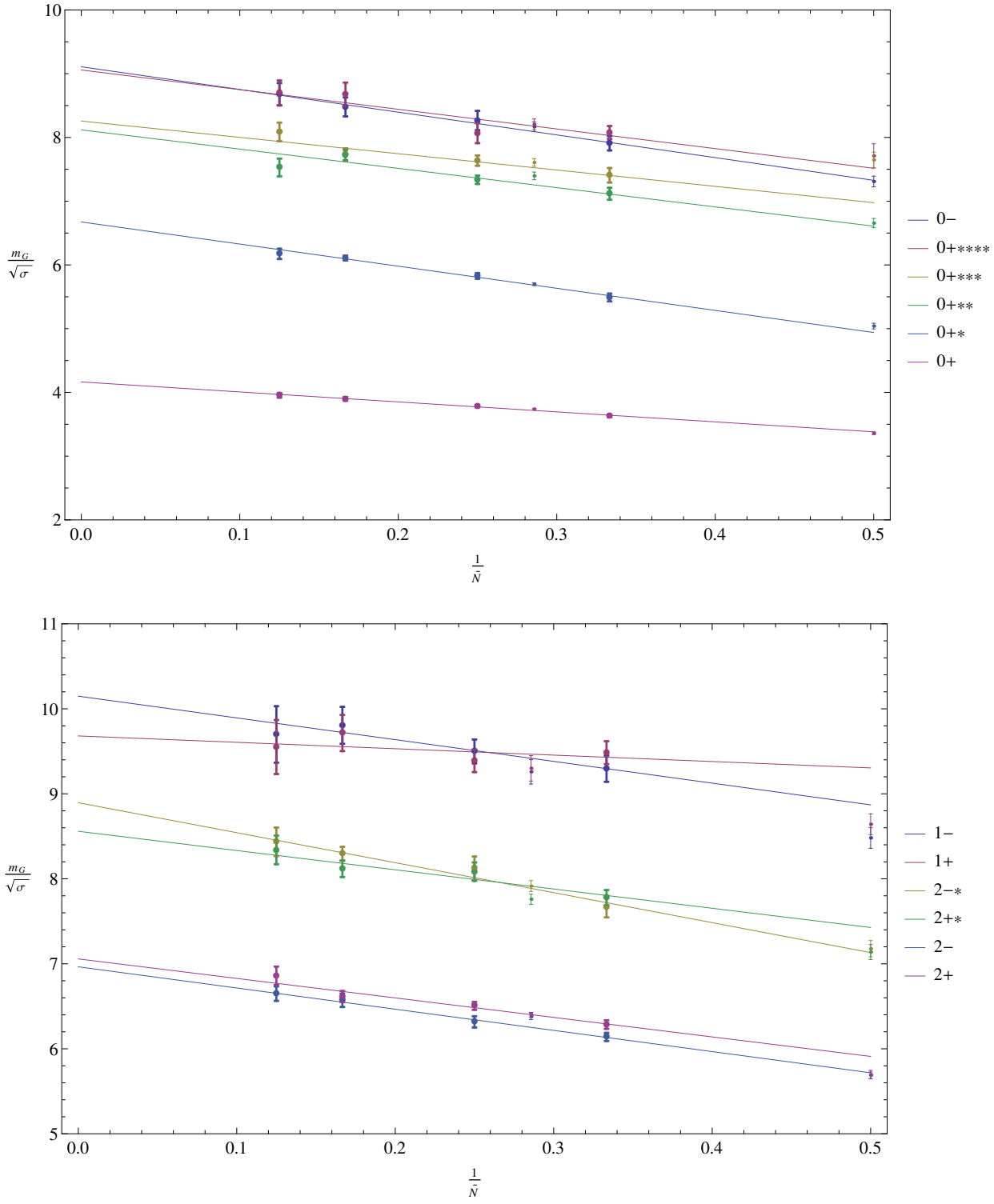

Figure 4.9: Large-N extrapolation of continuum $SO(N = 2\tilde{N})$ glueball mass spectrum in string tension units. We use only the thick style points in the extrapolations. We include the $SO(7)$ continuum values for comparison.

Chapter 5

Deconfining temperature

In this chapter, we calculate the deconfining temperatures of $SO(N)$ gauge theories in $2+1$ dimensions. We start by considering the theory behind the deconfining phase transition. We then go on to describe reweighting, which is the primary method we use to calculate the location of the phase transition. We then calculate the infinite volume limits, continuum limits, and large-N limits. We finally compare $SO(N)$ and $SU(N)$ deconfining temperatures between group equivalences.

5.1 Deconfinement

5.1.1 Finite temperature on the lattice

We can construct a finite temperature theory on the lattice by taking the infinite spatial volume limit $L_s \to \infty$ while fixing the 'temporal' length L_t and the inverse coupling β. A lattice field theory with lattice spacing a then has temperature $T(a) = 1/\left(a(\beta)L_t\right)$. If we assume that deconfinement occurs at $\beta = \beta_c$, then the deconfining temperature is

$$T_c(a) = \frac{1}{a(\beta_c)L_t} \tag{5.1}$$

5.1.2 Confinement in QCD

Quark confinement is a major feature of strong interactions, although there are competing definitions over what confinement actually is [39]. Experimentally, we observe that there are no free quarks in nature or, more generally, there are no particles of fractional electric charge. Hence, quarks must combine to form colour singlet hadronic states. In addition, we do not observe free gluons or other colour non-singlet states.

If we plot mesons of spin J against their mass squared m^2, we find that we can sort the data into groups that lie on straight lines known as Regge trajectories. We can recreate this result by a flux tube model linking a quark on one end to an antiquark on another [40]. The model predicts that the spins satisfy $J = m^2/(2\pi\sigma)$ where σ is the string tension, defined as the energy density per unit length of the flux tube, and the energy of the system scales like $m \sim \sigma l$ where l is the length of the flux tube. This model therefore indicates that the potential between a quark-antiquark pair is linear in its length and has been previously used to calculate the heavy quark spectrum.

The problem with confinement [39] is understanding why the gluonic flux is localised in a flux tube of fixed cross-sectional area, instead of spreading out like an electric field in QED or otherwise dissipating over space. As we pull apart sources in the fundamental representation such as very heavy quarks, the energy of the flux tube increases. If the energy of the flux tube exceeds the effective mass of light quark-antiquark pairs, then the flux tube decays to form heavy-light quark-antiquark pairs in a process we know as string breaking.

We can then express confinement in terms of a potential between a heavy quark-antiquark pair where $m_q \to \infty$ that approaches a linear dependence in its length l as $l \to \infty$.

5.1.3 The 'temporal' Polyakov loop

Consider a 'temporal' Polyakov loop l_P on a lattice with 'temporal' length L_t in direction of $\hat{t}$, representing a flux loop winding around the 'temporal' direction.

$$l_P(\mathbf{x}) = \mathrm{tr}\left(U_t(\mathbf{x})U_t(\mathbf{x}+\hat{t})\cdots U_t(\mathbf{x}-\hat{t})\right) \tag{5.2}$$

This operator represents the world line of a static quark at spatial site $\mathbf{x}$ [41]. This suggests that we can represent the free energy $F_{q\bar{q}}$ of a quark-antiquark pair at $\mathbf{x}$ and $\mathbf{y}$ respectively through the correlation function of two Polyakov loops at $\mathbf{x}$ and $\mathbf{y}$ with opposite orientations.

$$e^{-\frac{1}{T}F_{q\bar{q}}(x,y)} = \langle l_P(\mathbf{x}) l_P^T(\mathbf{y})\rangle \tag{5.3}$$

Assuming that the correlation function satisfies clustering, the correlation function decorrelates at large spatial distances.

$$\langle l_P(\mathbf{x}) l_P^T(\mathbf{y})\rangle \xrightarrow[|\mathbf{x}-\mathbf{y}|\to\infty]{} |\langle l_P\rangle|^2 \tag{5.4}$$

Hence, if $\langle l_P\rangle = 0$, then the free energy increases for large spatial separation of the quark-antiquark

pair. This is consistent with confinement. Similarly, if $\langle l_P \rangle \neq 0$, then the free energy approaches a constant value at large spatial separation. This is consistent with deconfinement.

We noted previously that $SO(2\tilde{N})$ gauge theories have a centre symmetry under which the action and measure are invariant. We can generate this centre symmetry by considering an element of the centre symmetry z and multiplying all 'temporal' links between two neighbouring spatial slices. However, the 'temporal' Polyakov loop is not invariant under this symmetry,

$$l_P \to z l_P \tag{5.5}$$

so that the expectation value of the Polyakov loop $\langle l_P \rangle$ must be zero for non-trivial z. However, this represents confinement. So we expect that the deconfinement phase transition represents a spontaneous breakdown of the centre symmetry. We note that $SO(2\tilde{N}+1)$ gauge theories have no such non-trivial centre symmetry so we cannot expect that these arguments hold in these cases.

5.2 Phase transitions and finite size scaling

5.2.1 Phase transitions

At infinite spatial volumes, phase transitions occur when the free energy becomes a non-analytic function in one of its parameters. We will see that we can classify the $SO(N)$ deconfining phase transitions into two different types. First order phase transitions occur when there is a discontinuity in the first derivative of the free energy such that the second derivative is typically a delta function singularity. Second order phase transitions occur when there is a divergence in the second derivative in the free energy although the first derivative is continuous. This results in a divergent correlation length.

On finite volumes, the partition function is finite so all derivatives are well-defined and analytic, so that there are no apparent non-analyticities. However, finite size scaling tells us that the results at finite volumes should converge towards the non-analyticity as we increase the spatial volume size, allowing us to classify the transition. We will use general arguments to explore these phase transitions.

5.2.2 First order transitions

Let us first consider first order transitions. Let O be an order parameter (such as the Polyakov loop) that takes a value O_c in the confined phase and O_d in the deconfined phase. We can define

a susceptibility $\chi_O(V,T)$ at a volume V and temperature T by

$$\chi_O(V,T) = \mathcal{N}V\left(\langle O(T)^2\rangle - \langle O(T)\rangle^2\right) \tag{5.6}$$

for some scaling constant $\mathcal{N}$. The system is in phase coexistence at the phase transition such that the order parameter takes values O_c and O_d with equal probability. Hence,

$$\chi_O(V,T_c) = \mathcal{N}V\left(\frac{(O_c^2+O_d^2)}{2} - \frac{(O_c+O_d)^2}{4}\right) = \mathcal{N}V\left(\frac{(O_c-O_d)^2}{4}\right) \tag{5.7}$$

Hence, the susceptibility height $\Delta\chi = \mathcal{O}(V)$. Similarly, consider the free energies $F_{c/d}(T) = f_{c/d}(T)V$ for the confined and deconfined phases respectively where f is the free energy per unit volume. The free energies are the same at the phase transition.

$$f_c(T_c) = f_d(T_c) \tag{5.8}$$

Consider the free energy ratio from these two phases at a temperature $T = T_c + \Delta T$ for small ΔT

$$\frac{e^{-F_c(T)/T}}{e^{-F_d(T)/T}} \approx \frac{e^{-[f_c(T_c)+\Delta T f_c'(T_c)]V/T_c}}{e^{-[f_d(T_c)+\Delta T f_d'(T_c)]V/T_c}} = e^{-[f_c'(T_c)-f_d'(T_c)]V\Delta T/T_c} \tag{5.9}$$

where we ignore higher order corrections in ΔT. This ratio compares the probabilities of being in either phase. If $|\Delta F|/T \gg 1$, then one phase dominates and the transition will go in only one direction [42]. This ratio also shows how the phase transition rate depends on V and T.

We now characterise this transition rate in terms of a characteristic susceptibility width in β. Define $\Delta\beta \equiv (\beta-\beta_c)/\beta_c = (T-T_c)/T_c = \Delta T/T_c$ if we use that $T = 1/(aL_t) = \beta g^2/(2NL_t)$. Consider the transition region around β_c in which the system tunnels between confined and deconfined phases, as we describe later. For there to be a susceptibility peak, tunnelling must occur between the confined and deconfined phases, so that the probability of being in either phase is comparable. Hence, we can see from (5.9), that this requires $V\Delta\beta = \mathcal{O}(1)$. This width $\Delta\beta$ of the transition region measures the characteristic width in the susceptibility χ_O. Hence, the characteristic susceptibility width decreases with V, $\Delta\beta = \mathcal{O}(1/V)$.

We can obtain more information about a temperature-driven first order transition by considering a thermodynamic system of spatial volume V, temperature T, and internal energy per site E. We follow the arguments in [43], and more generally [44–49]. We can describe the energy values E by a probability distribution $P_V(E)$, which we model as a Gaussian distribution centred at the infinite volume energy E_0 with a width proportional to the infinite volume specific heat C.

$$P_V(E) = \frac{\mathcal{N}}{\sqrt{C}} \exp\left(-\frac{(E-E_0)^2 V}{2k_B T^2 C}\right) \tag{5.10}$$

Here, $\mathcal{N}$ is a normalisation constant. At a first order transition, there is phase coexistence so that we expect $P_V(E)$ to be the superposition of two Gaussians centred at E_+ and E_-, where the subscripts $+/-$ correspond to the high temperature, ordered, deconfining phase and low temperature, disordered, confining phase respectively. At $\Delta T = T - T_c$, the two Gaussians are centred at $E_- + C_-\Delta T$ and $E_+ + C_+\Delta T$ where we assume that the specific heats in the two phases do not vary with temperature near T_c. If we express the free energy difference between the two phases as $\Delta F = F_+ - F_-$, then

$$P_V(E) = \sqrt{\frac{V}{2\pi k_B T^2}} \frac{1}{a_+ + a_-} \left(\frac{a_+}{\sqrt{C}_+} e^{-\frac{(E-(E_+ + C_+\Delta T))^2 V}{2k_B T^2 C_+}} + \frac{a_-}{\sqrt{C}_-} e^{-\frac{(E-(E_- + C_-\Delta T))^2 V}{2k_B T^2 C_-}} \right) \tag{5.11}$$

where, if there is only one deconfining and confining phase, $a_+ = e^x\sqrt{C_+}$, $a_- = e^{-x}\sqrt{C_-}$ and

$$x = \frac{-\Delta F V}{2k_B T} \tag{5.12}$$

We can then calculate the expectation value of the energy and specific heat at a finite volume V.

$$\begin{aligned}
\langle E \rangle_V &= \int \mathrm{d}E\, E P_V(E) \\
&= \frac{a_+ E_+ + a_- E_-}{a_+ + a_-} + \frac{(a_+ C_+ + a_- C_-)\Delta T}{a_+ + a_-} \\
C_V &= \frac{V}{k_B T^2} \left(\langle E^2 \rangle_V - \langle E \rangle_V^2 \right) \\
&= \frac{a_+ C_+ + a_- C_-}{a_+ + a_-} + \frac{a_+ a_- V \left[(E_+ - E_-) + (C_+ - C_-)\Delta T \right]^2}{k_B T^2 (a_+ + a_-)^2}
\end{aligned} \tag{5.13}$$

By expanding $F_\pm$ about T_c and using that $F_+(T_c) = F_-(T_c)$, we find that

$$\Delta F = \frac{-(E_+ - E_-)\Delta T}{T_c} \tag{5.14}$$

so that we can approximate x in (5.12)

$$x = \frac{(E_+ - E_-)\Delta T V}{2k_B T T_c} \approx \frac{(E_+ - E_-)\Delta T V}{2k_B T_c^2} \tag{5.15}$$

We see that in the infinite volume limit $V \to \infty$, if $\Delta T > 0$, then $a_+ \to \infty$ and $a_- \to 0$ so that the system is in the high temperature, deconfining phase and, if $\Delta T < 0$, then $a_+ \to 0$ and $a_- \to \infty$ so that the system is in the low temperature, confining phase, as we expect.

At finite volume, the two states contribute equally at the phase transition so that $a_+ = a_-$. Hence, we can see that $e^{2x} = \sqrt{C_-/C_+}$ so that

$$\frac{T_c(V) - T_c}{T_c} = \frac{k_B T_c \ln \sqrt{C_-/C_+}}{(E_+ - E_-)V} \tag{5.16}$$

where $T_c(V)$ is the deconfining temperature at spatial volume V. Hence, $T_c(V)$ differs from its infinite volume limit by $\mathcal{O}(1/V)$.

If $x \sim 1$, then we can estimate the scale of the transition region ΔT_{trans}.

$$\frac{\Delta T_{\text{trans}}}{T_c} \approx \frac{2k_B T_c}{(E_+ - E_-)V} \tag{5.17}$$

Hence, the transition occurs over a scale $\Delta T_{\text{trans}} = \mathcal{O}(1/V)$.

Finally, let us the consider the scaling form of the specific heat in (5.13). We expect that $E_+ - E_-$ and $C_+ - C_-$ are $\mathcal{O}(1)$ and since $\Delta T = \mathcal{O}(1/V)$ the term $(C_+ - C_-)\Delta T$ is small relative to $E_+ - E_-$ in the numerator of the second term in (5.13). Hence,

$$\begin{aligned} C_V &= c_1 + \frac{V(E_+ - E_-)^2 \sqrt{C_-/C_+}}{k_B T_c^2 \left[e^x + e^{-x}\sqrt{C_-/C_+}\right]^2} \\ &\approx c_1 + \frac{4V(E_+ - E_-)^2}{k_B T_c^2 \cosh^2(x)} \end{aligned} \tag{5.18}$$

where we take $C_+ \approx C_-$ and c_1 is a constant. This provides the scaling form for the specific heat.

Since $\Delta\beta \sim \Delta T$, these results together show that for a spatial volume V the transition occurs over a scale $\Delta\beta = \mathcal{O}(1/V)$ while the susceptibility forms a peak in the region of the bulk transition with height $\Delta\chi = \mathcal{O}(V)$ over a width $\Delta\beta = \mathcal{O}(1/V)$. This is consistent with a convergence towards a delta function singularity as $V \to \infty$.

5.2.3 Second order transitions

For a second order transition, finite size scaling tells us that the correlation length ξ approaches the spatial lattice length L_s close to T_c [45]. In this scaling region, dimensionless physical quantities depend on the dimensionless ratio L/ξ such that, for some scaling function f,

$$\frac{\chi(T, L_s)}{\chi(T, L_s \to \infty)} = f(L_s/\xi) \tag{5.19}$$

Let the reduced temperature

$$t = (T - T_c)/T_c = (\beta - \beta_c)/\beta_c \equiv \Delta\beta \tag{5.20}$$

if we use that $T = 1/(aL_t) = \beta g^2/(2NL_t)$. We define the critical exponents ν and γ by

$$\begin{aligned} \xi &\sim |t|^{-\nu} \sim |\Delta\beta|^{-\nu} \\ \chi(T, L_s \to \infty) &\sim |t|^{-\gamma} \sim |\Delta\beta|^{-\gamma} \end{aligned} \tag{5.21}$$

so that

$$\begin{aligned} \chi(T, L_s) &\sim |\Delta\beta|^{-\gamma} f(L_s|\Delta\beta|^{\nu}) \\ &= L_s^{\gamma/\nu}(L_s^{1/\nu}|\Delta\beta|)^{-\gamma} f(L_s|\Delta\beta|^{\nu}) \\ &= L_s^{\gamma/\nu} g(L_s^{1/\nu}|\Delta\beta|) \end{aligned} \tag{5.22}$$

for g a scaling function. For a spatial volume $V = L_s^d$, this shows that at the transition the susceptibility has height $\Delta\chi = \mathcal{O}(V^{\frac{\gamma}{d\nu}})$ over a width $\Delta\beta = \mathcal{O}(1/V^{\frac{1}{d\nu}})$. Hence if $\gamma > \nu$, we expect that the susceptibility peak height increases non-linearly as $V \to \infty$ and that this increase is greater than the decrease in the characteristic peak width so that it generates a set of overlapping peaks.

5.2.4 Scaling laws

Hence, we can distinguish between the first and second order transitions by examining the structure of susceptibility peaks over a range of different spatial volumes. We summarise the scaling laws by the following relations. In $D = 2 + 1$, the phase transition occurs at

$$\begin{aligned} &\frac{T_c(\infty) - T_c(V)}{T_c(\infty)} \sim \frac{1}{V} \qquad \Rightarrow \qquad \beta_c(V) = \beta_c(\infty)\left[1 - h\left(\frac{L_t}{L_s}\right)^2\right] \qquad \text{1st order} \\ &\frac{T_c(\infty) - T_c(V)}{T_c(\infty)} \sim \frac{1}{V^{\frac{1}{2\nu}}} \qquad \Rightarrow \qquad \beta_c(V) = \beta_c(\infty)\left[1 - k\left(\frac{L_t}{L_s}\right)^{\frac{1}{\nu}}\right] \qquad \text{2nd order} \end{aligned} \tag{5.23}$$

where h, k are constants and we used that $T = 1/(aL_t) = \beta g^2/(2NL_t)$. In $D = 2+1$, the maximum of the susceptibility peak $\chi_{\max}(V)$ depends on the spatial volume V as

$$\begin{aligned} \chi_{\max}(V) &= c_0 V + c_1 && \text{1st order} \\ \chi_{\max}(V) &= c_0 V^{\frac{\gamma}{2\nu}} + c_1 && \text{2nd order} \end{aligned} \tag{5.24}$$

for constants c_0 and c_1. Hence, finite size scaling shows us how $\beta_c(V)$ and $\chi_{\max}(V)$ varies with the spatial volume V, and how to extrapolate $\beta_c(V)$ to the infinite spatial volume limit.

5.2.5 Order parameters

An order parameter is a thermodynamic quantity that distinguishes between different phases and exhibits a non-analyticity at the phase transition. We need an order parameter to determine if and where the deconfinement phase transition occurs. We know that phase transitions correspond to non-analyticities in the derivatives of the free energy F with respect to β so consider the first two derivatives

$$\begin{aligned}\left(\frac{1}{N_p}\frac{\partial}{\partial\beta}\right)F &\sim \left(\frac{1}{N_p}\frac{\partial}{\partial\beta}\right)\ln Z \sim \langle\overline{U}_p\rangle \\ \left(\frac{1}{N_p}\frac{\partial}{\partial\beta}\right)^2 F &\sim \left(\frac{1}{N_p}\frac{\partial}{\partial\beta}\right)\langle\overline{U}_p\rangle = \langle\overline{U}_p^2\rangle - \langle\overline{U}_p\rangle^2 \equiv \chi_{\overline{U}_p}\end{aligned} \tag{5.25}$$

where N_p is the number of plaquettes, Z is the partition function, $\overline{U}_p = \frac{1}{N_p}\sum_p \left(\frac{1}{N}\mathrm{tr}(U_p)\right)$, and $\chi_O = \langle O^2\rangle - \langle O\rangle^2$ is the susceptibility of the operator O. This indicates that the plaquette $\overline{U}_p$ may be a suitable order parameter. If so, the peak in its susceptibility corresponds to the position of the phase transition.

However, our results indicate that the plaquette susceptibility has a weakly varying signal over the phase transition. Suppose that we partition plaquettes into those that are only spatial $\overline{U}_s$ and those that have links in a temporal direction $\overline{U}_t$. Figure 5.1 shows the spatial plaquette susceptibility $\chi_{\overline{U}_s}$ and the temporal plaquette susceptibility $\chi_{\overline{U}_t}$ in the region of the phase transition for an $SO(4)$ 32^23 volume, normalised for comparison. We want a clear peak in the susceptibility to identify the phase transition location. We can see that $\chi_{\overline{U}_s}$ has no peak structure and that $\chi_{\overline{U}_t}$ has a weak peak structure. At volumes for other $SO(N)$, $\chi_{\overline{U}_t}$ has no peak structure. So the plaquette susceptibility is not a suitable order parameter.

As previous arguments suggest, we use an alternative operator related to the 'temporal' Polyakov loop l_P. We consider the absolute value of the Polyakov loop (5.2) after we have averaged it over the spatial volume [50]

$$\left|\overline{l_P}\right| = \left|\frac{1}{L_s^2}\sum_{\mathbf{x}} l_P(\mathbf{x})\right| \tag{5.26}$$

We use $\left|\overline{l_P}\right|$ to be the order parameter and then construct an associated 'susceptibility'.

$$\frac{\chi_{|\overline{l_P}|}}{L_s^2 L_t} = \left\langle\left|\overline{l_P}\right|^2\right\rangle - \left\langle\left|\overline{l_P}\right|\right\rangle^2 \tag{5.27}$$

We use this order parameter and susceptibility for several reasons. Firstly, we note that it has

the same form as the susceptibility term in (5.25). We choose the normalisation $L_s^2 L_t$ but, since we will compare results by varying the spatial volume V for fixed L_t, we could similarly choose V or N_p without changing the results within rescaling. Secondly, the Polyakov loop operator $\overline{l_P}$ has a much clearer signal in the region of the phase transition, compared to the plaquette operators. It tunnels between confined and deconfined phases around the transition so that $\overline{l_P}$ takes discrete values within very small fluctuations, as we will see later. Thirdly, we use the absolute value of the Polyakov loop operator $\left|\overline{l_P}\right|$ instead of $\overline{l_P}$ because, as we will see later, $\overline{l_P}$ tunnels between two deconfined phases with opposite parities in an $SO(2\tilde{N})$ system, which would average to zero, incorrectly indicating that the system is still in a confined phase where $\left\langle \overline{l_P} \right\rangle \approx 0$. Finally, it has a very good signal in the region of the phase transition. We again calculate $\chi_{\left|\overline{l_P}\right|}$ for an $SO(4)$ $32^2 3$ volume and display its plot in Figure 5.1. We can see that $\chi_{\left|\overline{l_P}\right|}$ has a much clearer peak structure than the plaquette susceptibilities.

In summary, in a plot of $\left\langle \left|\overline{l_P}\right| \right\rangle$ against β in the neighbourhood of β_c, we would expect to see the value of $\left\langle \left|\overline{l_P}\right| \right\rangle$ increase from zero to a fixed non-zero value. We expect to see a corresponding peak in $\chi_{\left|\overline{l_P}\right|}$ at β_c. For a first order transition, we expect that the order parameter $\left\langle \left|\overline{l_P}\right| \right\rangle$ has a discontinuity at β_c and the susceptibility $\chi_{\left|\overline{l_P}\right|}$ to resemble a delta function singularity. Meanwhile, for a second order phase transition, we expect that the susceptibility $\chi_{\left|\overline{l_P}\right|}$ has a divergence at β_c while $\left\langle \left|\overline{l_P}\right| \right\rangle$ remains continuous there.

5.2.6 Tunnelling

We can represent $\overline{l_P}$ values over a configuration run for a given β as either a histogram over the entire run, or as a history plot along the run. For $\beta < \beta_c$, we expect the theory to be confining so that $\left\langle \overline{l_P} \right\rangle \approx 0$. On the histogram, we would expect that the values form a narrow peak around zero while, on the history plot, we would expect the values to fluctuate around zero. This represents a confined phase at zero. For $\beta > \beta_c$, the system would be in a deconfined phase so that $\left\langle \overline{l_P} \right\rangle \neq 0$, and we would expect to see deconfined peaks at non-zero values on the histogram. For $SO(2\tilde{N})$ gauge theories, we would expect to see two deconfined peaks at non-zero values while, for $SO(2\tilde{N}+1)$ gauge theories, we would only expect one deconfined peak at a non-zero value.

For $\beta \approx \beta_c$, the system jumps between different phases, which we can see on a history plot. We call these jumps tunnelling. The transition between different phases depends on its order. For a first order transition, as we increase β towards β_c, we would expect to see deconfined peaks appear at non-zero values while the confined peak at zero decreases. On the history plot, we would see the

$\overline{l_P}$ values start to jump between zero and non-zero values. This shows that the system is tunnelling between the confined and deconfined phases. At $\beta = \beta_c$, we would expect the probability of being in confined or deconfined phases to be equal, representing coexisting phases. The histogram would show approximately equal peaks at zero and non-zero values while the history plot would show considerable tunnelling between the phases. For a second order transition, there is no phase coexistence. As we increase β, we would expect the confined peak at zero to spread out and, once it disappears, the deconfined peaks emerge at $\beta = \beta_c$. On the history plot, we would expect to see significant fluctuations around zero for $\beta < \beta_c$ before suddenly tunnelling between non-zero values for $\beta > \beta_c$.

Hence, we can use both the histograms and history plots of $\overline{l_P}$ values to distinguish between the first and second order transitions.

5.3 Reweighting

We want to calculate the value of an observable (in our case, the susceptibility) for an arbitrary β value so that we can identify β_c corresponding to a maximum in the observable. We first collect data from separate runs at different β values and calculate the observable at each β. We could then estimate the location of the maximum over the dataset, for example by bisecting intervals of β to approach the maximum, and then calculating the observable at new β values to refine the estimate.

However, we would prefer to use the original data to calculate the observable directly at arbitrary β. To do this, we note that we could view the process of generating lattice configurations as sampling an underlying density of states, which is independent of β. If we could reconstruct the density of states, we could then use it to calculate observables at arbitrary values of β. We can do this by reweighting [51, 52], which uses the data from multiple runs to reconstruct this density of states. This was the approach taken by previous studies of the $SU(N)$ deconfining phase transition [42, 50, 53–56].

5.3.1 Single run reweighting

We can calculate the probability density of field configurations $P(S_i|\beta)$ with an action S_i at a value β using the partition function $Z(\beta)$ with a density of states $D(S_i)$.

$$P(S_i|\beta) = \tfrac{1}{Z(\beta)} D(S_i) e^{-\beta S_i}$$
$$Z(\beta) = \sum_i D(S_i) e^{-\beta S_i} \tag{5.28}$$

Consider the data from a single configuration run at $\beta = \beta_k$. Let the unnormalised histogram estimate of $P(S_i|\beta_k)$ be $N_k(S_i)$ with n_k total measured configurations.

$$\begin{aligned}
\Rightarrow \qquad N_k(S_i) n_k^{-1} &\approx \tfrac{1}{Z(\beta_k)} D(S_i) e^{-\beta_k S_i} \\
&= P(S_i|\beta) \tfrac{Z(\beta)}{Z(\beta_k)} e^{(\beta-\beta_k)S_i} \\
\Rightarrow \qquad P(S_i|\beta) &\approx \tfrac{Z(\beta_k)}{Z(\beta)} N_k(S_i) n_k^{-1} e^{(\beta_k-\beta)S_i} \\
\Rightarrow \qquad P(S_i|\beta) &\approx \frac{N_k(S_i) n_k^{-1} e^{(\beta_k-\beta)S_i}}{\sum_j N_k(S_j) n_k^{-1} e^{(\beta_k-\beta)S_j}}
\end{aligned} \tag{5.29}$$

where we used that $\sum_j P(S_j|\beta) = 1$ in the last step. In this expression for $P(S_i|\beta)$, we know everything on the right-hand side, so we can estimate the probability from the histogram data at a nearby value of $\beta = \beta_k$. Then, with data on how the observable values depend on action values $O(S_i)$, we can estimate an observable $\langle O(\beta) \rangle$.

$$\langle O(\beta) \rangle = \sum_i O(S_i) P(S_i|\beta) \tag{5.30}$$

5.3.2 The free energy

We can relate the free energy F_k to the partition function $Z(\beta_k)$ at $\beta = \beta_k$ by

$$Z(\beta_k) = e^{-\beta_k F_k} \tag{5.31}$$

We know from (5.28) that the density of states is given by

$$D(S_i) = P(S_i|\beta) Z(\beta) e^{\beta S_i} \tag{5.32}$$

Hence, define a density of states estimate $\tilde{D}_i^{(k)}$ using the histogram data at $\beta = \beta_k$ by

$$\begin{aligned}
\tilde{D}_i^{(k)} &= N_k(S_i) n_k^{-1} e^{\beta_k (S_i - F_k)} \\
&\approx D(S_i)
\end{aligned} \tag{5.33}$$

We will use this expression to carry out a multiple run reweighting.

5.3.3 Multiple run reweighting

Consider the data from multiple runs at different values of $\beta = \beta_k$. We can use this data to generate density of states estimates $\tilde{D}_i^{(k)}$. We want to combine these estimates to form an overall density of states estimate $\tilde{D}_i \approx D(S_i)$. To do this, we need to weight the contribution of each estimate $\tilde{D}_i^{(k)}$ by a weight $w_i^{(k)}$, normalised such that $\sum_k w_i^{(k)} = 1$, so that

$$\begin{aligned}\tilde{D}_i &= \sum_k w_i^{(k)} \tilde{D}_i^{(k)} \\ &= \sum_k w_i^{(k)} N_k(S_i) n_k^{-1} e^{\beta_k (S_i - F_k)}\end{aligned} \tag{5.34}$$

To minimise errors σ_D^2 in $\tilde{D}_i$, we pick specific weights [52].

$$w_i^{(k)} = \frac{n_k e^{\beta_k (F_k - S_i)}}{\sum_m n_m e^{\beta_m (F_m - S_i)}} \tag{5.35}$$

Hence, we generate estimates for the unnormalised probability density

$$\tilde{P}(S_i|\beta) \equiv \tilde{D}_i e^{-\beta S_i} \approx P(S_i|\beta) Z(\beta) \tag{5.36}$$

and the free energy $\tilde{F}$.

$$\tilde{D}_i = \frac{\sum_k N_k(S_i)}{\sum_m n_m e^{\beta_m (F_m - S_i)}} \quad \Rightarrow \quad \tilde{P}(S_i|\beta) = \frac{\sum_k N_k(S_i) e^{-\beta S_i}}{\sum_m n_m e^{\beta_m (\tilde{F}_m - S_i)}} \tag{5.37}$$

$$Z(\beta_k) = e^{-\beta_k F_k} \approx \sum_i \tilde{D}_i e^{-\beta_k S_i} \quad \Rightarrow \quad \tilde{F}_k = -\beta_k^{-1} \ln \sum_i \tilde{P}(S_i|\beta_k) \tag{5.38}$$

We can then iterate (5.37) and (5.38) to generate successive values for $\tilde{P}$ and $\tilde{F}$ to refine our estimate for the probability density $P(S_i|\beta)$. We then use these values to calculate an observable $\langle O(\beta) \rangle$ using (5.30) and that

$$P(S_i|\beta) \approx \frac{\tilde{P}(S_i|\beta)}{Z(\beta)} = \frac{\tilde{P}(S_i|\beta)}{\sum_j \tilde{P}(S_j|\beta)} \tag{5.39}$$

5.3.4 Reweighting in practice

We note that the expression for the probability $\tilde{P}$ in (5.37) has a factor of $e^{-\beta S_i}$. For $\beta \sim \mathcal{O}(10)$ and a lattice with $\mathcal{O}(1000)$ sites, $e^{-\beta S_i} \sim \mathcal{O}(e^{-10000})$, which may exceed the machine precision. Hence, we need to reduce the exponent range in the expression for $\tilde{P}$. Let $\bar{\beta}$ be a typical β value and $\bar{S}$ be a typical action value during a configuration run. Then a rescaled expression for (5.37) is

$$\tilde{P}(S_i|\beta) = \frac{e^{-(\beta-\bar{\beta})(S_i-\bar{S})}\sum_k N_k(S_i)}{e^{\bar{\beta}(S_i-S)+\beta\bar{S}}\sum_m n_m e^{\beta_m(\tilde{F}_m-S_i)}} \tag{5.40}$$

and this rescaling reduces the range of values of both the numerator and denominator. We also note that the free energy F in (5.38) is invariant under $F_m \to F_m + F'/\beta_m$ for some constant F'. The iterative process described by (5.37) and (5.38) does not necessarily lead the $\beta_k\tilde{F}_k$ values to converge but the differences between them do.

5.3.5 Curve fitting

For some very large spatial volumes, the range of $\tilde{P}$ values exceeds the machine precision even when we rescale them by (5.40). In these cases, we cannot use reweighting, and we instead propose a curve fit to the susceptibility plot to extract β_c. For first order phase transitions, (5.18) indicates that the susceptibility may take the form

$$\chi_V \sim \chi_{V\to\infty} + aV\text{sech}^2\left(bV(\beta-\mu)\right) \tag{5.41}$$

for constants a, b, and μ. However, our results show that the cases when we cannot use reweighting correspond to second order transitions. Here, we only have scaling arguments for the susceptibility form for finite volumes (5.22) and there is no obvious curve fit candidate.

To consider curve fit candidates, we apply a candidate to a range of values $(\beta, \chi(\beta))$ calculated by separate runs with β close to β_c, and remove points symmetrically about the peak until the fit has a $\bar{\chi}^2_{\text{dof}} \approx 1$. To test this procedure, we apply two such candidates, the Gaussian distribution f_G and logistic distribution f_L, to a data set where we can use reweighting

$$\begin{aligned} f_G(x|\mu,\sigma) &= \frac{A}{\sqrt{2\pi}\sigma}e^{-\frac{(x-\mu)^2}{2\sigma^2}} \\ f_L(x|\mu,s) &= \frac{B}{4s}\text{sech}^2\left(\frac{x-\mu}{2s}\right) \end{aligned} \tag{5.42}$$

for A, B scaling constants. We apply both reweighting and curve fitting to data for an $SO(4)$ 40^24 volume. We display the fits in Figure 5.2 and list the resulting β_c and $\chi(\beta_c)$ in Table 5.1. We see that the two curve fits agree well with the data and reweighted values around the peak, and that the estimates for β_c and $\chi(\beta_c)$ from the curve fits are within errors of the reweighting estimates. Although the curve fitting becomes increasingly unreliable further away from the peak, we only need it to be reliable close to the peak.

We conclude that curve fitting provides a useful alternative to reweighting for large volumes

where we cannot reweight. Since the results from both candidate fitting function give very similar results, we choose to use the logistic distribution because it is the fitting function for finite volumes with first order phase transitions in (5.18).

5.4 Infinite volume limits

5.4.1 Methodology

Summarising the theory above, for given $SO(N)$ and L_t values, we want to calculate $\beta_c(V \to \infty)$ at the infinite volume limit $L_s \to \infty$. To do this, we use $\left|\overline{l_P}\right|$ as the order parameter. For a given finite spatial volume V, we can calculate $\beta_c(V)$ by calculating the susceptibility $\chi_{\left|\overline{l_P}\right|}$ for a range of β values around β_c, reweighting data from those β values where there is tunnelling between different phases. If the lattice volume is too large for reweighting, we follow the curve fitting procedure that we detailed previously. Then $\beta_c(V)$ is the β value that corresponds to a maximum in $\chi_{\left|\overline{l_P}\right|}$.

As an example, consider the case of an $SO(6)$ $20^2 3$ volume using a run of a million configurations. In Figure 5.3, we display a plot of the Polyakov loop values $\left\langle\left|\overline{l_P}\right|\right\rangle$ for a range of β values. It shows a jump from a confined phase where $\left\langle\left|\overline{l_P}\right|\right\rangle \approx 0$ to a deconfined phase where $\left\langle\left|\overline{l_P}\right|\right\rangle \neq 0$. We draw three vertical lines at characteristic values $\beta = \beta_- < \beta_0 < \beta_+$. We display the history plots of the Polyakov loop values for these three β values in Figure 5.4. At $\beta = \beta_-$, we see that the system remains in a confined phase around zero with small statistical fluctuations and very limited tunnelling to non-zero values. At $\beta = \beta_0$, there is much more tunnelling and the system spends equal time in both the confined and deconfined phases. At $\beta = \beta_+$, the system settles into a deconfined phase, where $\left\langle\left|\overline{l_P}\right|\right\rangle$ takes a non-zero value, tunnelling occasionally between the deconfined phases. Similarly, we can look at the histograms of the Polyakov loop values for these three β values in Figure 5.5, where the histogram peaks strongly at zero for the confined phase at $\beta = \beta_-$, shows coexistent phases at $\beta = \beta_0$, and shows two peaks for the deconfined phase at $\beta = \beta_+$. Both the history plot and histogram show phase coexistence around β_c, indicating that this is a first order transition. We use both the history plots and histograms to find which β values correspond to tunnelling. We would then use these β values for reweighting. We now consider the Polyakov loop susceptibility $\chi_{\left|\overline{l_P}\right|}$ in Figure 5.6. The data from calculations at specific β values indicates a peak around $\beta = \beta_0$ so we may suspect that $\beta_0 \approx \beta_c$. To show this, we reweight using data from β values where there is tunnelling between confined and deconfined phases. We display the resulting reweighting data in Figure 5.6. We see that the reweighted data agrees well with our

original data and that the estimates for β_c and $\chi_{|\overline{l_P}|}(\beta_c)$ have very small errors.

For spatial volumes at different L_t, we note that L_s/L_t is dimensionless so we should compare lattice volumes at different L_t by keeping this ratio constant. Then we can extrapolate these values of $\beta_c(V)$ to $V \to \infty$ depending on the order of the transition using the equations

$$\begin{aligned} \beta_c(V) &= \beta_c(V \to \infty)\left[1 - h\,(L_t/L_s)^2\right] && \text{1st order} \\ \beta_c(V) &= \beta_c(V \to \infty)\left[1 - k\,(L_t/L_s)^{\frac{1}{\nu}}\right] && \text{2nd order} \end{aligned} \tag{5.43}$$

Finally, we consider how tunnelling varies with the volume V and N. Tunnelling occurs between phases that have similar free energies. Close to the transition, the lattice volume splits into two approximately equal domains for the confined or deconfined phases. Two domain walls separate these domains and each have surface tension per unit length σ_W. The most probable configuration of a domain wall is one that minimises the surface length. The energy of a domain wall with spatial length l_s is $E = \sigma_W l_s$. Hence, the probability P_W of a bubble with two spatial walls of length $l_s = aL_s$ is

$$P_W(T) = \exp\left(-\frac{2\sigma_W l_s}{T}\right) = \exp\left(-2a^2\sigma_W L_s L_t\right) \tag{5.44}$$

Papers on $SU(N)$ deconfining temperatures [53] indicate that the surface tension grows with N^2, $\sigma_W \propto N^2$. Hence, the probability of the domain walls and the probability of tunnelling exponentially decreases as either the volume V increases or as N increases. So transitions between the two states are increasingly rare at large V, especially at large N, and this provides upper bounds on the volumes we can consider for a given N. In particular, this means that, while keeping L_s/L_t constant for a given N, there are upper bounds on L_t before it exponentially suppresses tunnelling.

5.4.2 $SO(4)$ and $SO(5)$

The $SO(4)$ and $SO(5)$ deconfining phase transitions are second order. We can see this from the $\langle\overline{l_P}\rangle$ histograms, such as Figure 5.7, which show a continuous transition from confined to deconfined phases as we increase β. We can also see this in susceptibility plots for different spatial volumes at fixed L_t, such as Figure 5.8, which show that, as the spatial volume increases, the susceptibility peak height increases faster than the characteristic peak width decreases.

For $SO(4)$, we can use reweighting for $2 \leq L_t \leq 4$ to calculate β_c. For $L_t = 5$, the susceptibility peak is at $\beta \in [9.0, 10.0]$. This is in the bulk transition region, as we will discuss later, which affects

the data so greatly that reweighting does not work. For $L_t \geq 6$, the spatial volumes become so large that we cannot reweight the data and so we need to curve fit instead. For smaller L_t, the values lie on a smooth curve with small errors and the reweighted values fit well with the original data. At larger L_t, the data is more scattered than at smaller L_t, although we can still estimate β_c with low errors. We present the values of $\beta_c(V)$ for volumes V for $L_t = 2, 3, 4, 6, 7, 8, 10, 12$ in Tables 5.2 and 5.3.

To extrapolate $\beta_c(V \to \infty)$ to the infinite volume limit using (5.43), we need a value for the critical exponent ν. To obtain an estimate for ν, we simultaneously fit the data for each L_t with

$$\beta_c(V, L_t) = c_0(L_t) + c_1(L_t) \left(\frac{L_t}{L_s}\right)^{\frac{1}{\nu}} \tag{5.45}$$

where $c_0(L_t)$ and $c_1(L_t)$ are coefficients that depend on L_t and we require ν to be the same value across all data. We present these fitting results in Figure 5.9 and we find that $\nu = 0.65(7)$. There is a high $\bar{\chi}^2_{\text{dof}}$ for two reasons. Firstly, it is difficult to obtain an accurate value for ν since it is difficult to constrain the fit (5.45) near $L_t/L_s \approx 0$ without many data values at large spatial volumes. Secondly, there is scattering in some data sets with very low data errors so it is difficult to apply fits without a large $\bar{\chi}^2_{\text{dof}}$. Removing these data sets reduces the $\bar{\chi}^2_{\text{dof}}$ while ν remains at similar values. We also fit ν to the data with $L_t \leq 4$ and $L_t \geq 6$ separately in Figure 5.9, which we show later correspond to the strong and weak coupling values respectively. We see that the values of ν are 1.10(22) in strong coupling and 0.39(4) in weak coupling. We see that the $\bar{\chi}^2_{\text{dof}}$ from $L_t \geq 6$ values varies considerably for different ν values while there is little variance for the $L_t \leq 4$ values. Given the variance of these results and because we will extrapolate the weak coupling values for the large-N extrapolation, we choose $\nu = \frac{1}{2}$, the same scaling as for first order transitions. We note that, since $SO(2\tilde{N})$ gauge groups have a $\mathbb{Z}_2$ centre symmetry, the Svetitsky-Yaffe conjecture [57] puts the $SO(2\tilde{N})$ deconfining phase transition in the same universality class as a spin system invariant under a $\mathbb{Z}_2$ symmetry with the same spatial dimensions. Hence, we might naively expect it to share the same critical exponents as the $D = 2$ Ising model, such as $\nu = 1$. This was the critical exponent used for the second order $SU(2)$ deconfining transition [50]. However, this value is unsuitable for the weak coupling $L_t \geq 6$ data. The universality classes for $SO(4) \sim SU(2) \times SU(2)$, a cross product group, and $SO(5)$ are also uncertain so this requires future investigation.

We list these infinite volume limits in Table 5.11. We see that the extrapolation values are good with very small errors and most of the $\bar{\chi}^2_{\text{dof}}$ values are reasonable. One $\bar{\chi}^2_{\text{dof}}$ value is large, which is

due to scattering among values with very small errors.

For $SO(5)$, we can use reweighting for $2 \leq L_t \leq 6$ and curve fitting for $L_t = 7$ to calculate β_c. Due to the lack of a $\mathbb{Z}_2$ centre symmetry, there is only one deconfined vacua but this does not affect our approach. As we stated earlier, the lack of the $\mathbb{Z}_2$ centre symmetry also means that we cannot expect $\langle |\overline{l_P}| \rangle \approx 0$ in the confined phase. However, our calculations of $\langle |\overline{l_P}| \rangle$ show that this is the case. As with $SO(4)$, we take the critical exponent $\nu = \frac{1}{2}$ in extrapolating $\beta_c(V \to \infty)$. We list the β_c values for finite volumes in Table 5.4 and for the infinite volume limits in Table 5.12. We see that the extrapolation values are good with very small errors and that the $\bar{\chi}^2_{\text{dof}}$ values are reasonable.

5.4.3 $SO(6)$

The $SO(6)$ deconfining phase transition is weakly first order. The coexisting phases are occasionally apparent, but are less defined than for $SO(N \geq 7)$. Susceptibility plots (such as Figure 5.10) indicate that the transition has features from both first and second order transitions while the $\langle \overline{l_P} \rangle$ histograms (such as Figure 5.5) show first order phase coexistence. We extrapolate to the infinite volume limit using (5.43). We list the β_c values for finite volumes in Table 5.5 and for the infinite volume limits in Table 5.13. We see that the extrapolation values are good with very small errors and that the $\bar{\chi}^2_{\text{dof}}$ values are reasonable.

5.4.4 $SO(7)$, $SO(8)$, $SO(9)$, $SO(12)$, and $SO(16)$

The $SO(N \geq 7)$ deconfining phase transition is first order. There is clear phase coexistence in the $\langle \overline{l_P} \rangle$ histograms and the susceptibility peaks (such as Figure 5.11) show the characteristic susceptibility peak width decreasing at the same rate as the peak height increases. As we stated earlier, the lack of the $\mathbb{Z}_2$ centre symmetry for $SO(7)$ and $SO(9)$ gauge theories means that we cannot expect $\langle |\overline{l_P}| \rangle \approx 0$ in the confined phase. However, as with $SO(5)$, our calculations confirm that $\langle |\overline{l_P}| \rangle \approx 0$. We extrapolate to the infinite volume limit using (5.43). For $SO(N)$ with $N = 7, 8, 9, 12, 16$, we list the β_c values for finite volumes in Tables 5.6, 5.7, 5.8, 5.9, and 5.10 and the infinite volume limits in Tables 5.14, 5.15, 5.16, 5.17, and 5.18. We see that the extrapolation values are good with very small errors and that the $\bar{\chi}^2_{\text{dof}}$ values are reasonable.

5.5 Continuum limits

5.5.1 Methodology

We can express the critical temperature in string tension units $T_c/\sqrt{\sigma}$, evaluated at the critical coupling β_c. The string tension sets a scale for the critical temperature.

$$\frac{T_c}{\sqrt{\sigma}} = \frac{1}{a\sqrt{\sigma}L_t} \tag{5.46}$$

Since this is the ratio of two quantities with mass dimensions, we expect the leading correction to be $\mathcal{O}(a^2)$ [1]. Hence, for some constant c,

$$\frac{T_c}{\sqrt{\sigma}}(a) = \frac{T_c}{\sqrt{\sigma}}(a=0) + ca^2\sigma + \cdots \tag{5.47}$$

Once we have calculated β_c for a value of L_t, we calculate the continuum string tension at β_c on a large volume using Polyakov loop operators, following the same methods we used to obtain the $SO(N)$ string tensions.

5.5.2 Bulk transition

Lattice gauge theories generally have a bulk transition between regions of strong and weak coupling where the coupling expansions changes from powers of $\beta \propto 1/(ag^2)$ to $1/\beta \propto ag^2$ respectively. We can only extrapolate to the continuum limit $a \to 0$ in the weak coupling region so it is important to know where this bulk transition occurs. On the lattice, we find that the location of the $SO(N)$ bulk transition seems to correspond to a region where the scalar glueball mass m_{0^+} becomes unusually light [58]. This is an interesting but not well-understood phenomenon, which we may explore in the future but not in this thesis. Nonetheless, it proves to be a useful way to identify the bulk transition location. Hence, through evaluating the m_{0^+} mass across a region of β, we can identify the location of the transition.

We display one such scan for the m_{0^+} mass in Figure 5.12 for three $SO(4)$ volumes. For $\beta < 8.0$, we can see that the m_{0^+} mass remains approximately constant. It then decreases to zero in the region $\beta \in [8.0, 10.5]$ before jumping to its original value for $\beta > 10.5$. This drop in the m_{0^+} mass indicates that the bulk transition is in the region $\beta \in [8.0, 10.5]$. As L_s increases, we can see that the lower bound of the bulk transition region increases while the upper bound stays constant. So we can find approximate bounds for this region for each $SO(N)$ by calculating the region using

volumes with smaller L_s than we use for the deconfining temperature calculations.

We show the β_c values corresponding to the bulk transition in Table 5.19. As N increases, we find that we need volumes with smaller L_s to identify the bulk transition. At volumes with larger L_s, there is no signal of the bulk transition.

To calculate the continuum limit of the deconfinement temperature, we should use data corresponding to values in the weak coupling region. This means that we may have to discard data from L_t values that have β_c values in the strong coupling region. We show these lower bounds of L_t in Table 5.19. Unless we otherwise state, we only extrapolate to the continuum limit using L_t values in the weak coupling region.

5.5.3 $SO(4)$

For $SO(4)$, β_c values for $L_t < 5$ are in the strong coupling region whereas β_c values for $L_t > 5$ are in the weak coupling region. We treat these two regions separately since we only expect a continuum extrapolation in the weak coupling region. We give the values for the critical temperatures $T_c/\sqrt{\sigma}$ in Table 5.20. We can obtain very accurate string tension values since we can complete high statistic runs due to the small dimension of the gauge group. We can then plot $T_c/\sqrt{\sigma}$ against $a^2\sigma$ and extrapolate to the continuum limit using (5.47). We display this plot in Figure 5.13. In this plot, firstly we can see that we can fit the strong coupling values ($L_t < 5$) with a linear extrapolation in $a^2\sigma$ with a very small $\bar{\chi}^2_{\text{dof}}$. This is surprising since there is no natural continuum limit for the strong coupling expansion. Secondly, we see that the weak coupling values $L_t > 5$ fit naturally on a continuum extrapolation and agree with each other within errors so that the first order term in $a^2\sigma$ is small. The continuum limits are

$$\begin{aligned}
&\frac{T_c}{\sqrt{\sigma}}(a=0) = 0.7844(51) \qquad \bar{\chi}^2_{\text{dof}} = 0.36 \qquad SO(4) \text{ (weak coupling)} \\
&\frac{T_c}{\sqrt{\sigma}}(a=0) = 0.8579(2) \qquad \bar{\chi}^2_{\text{dof}} = 0.00005 \qquad SO(4) \text{ (strong coupling)}
\end{aligned} \tag{5.48}$$

Thirdly, we see that the weak and strong coupling continuum values do not agree with each other, indicating that the physics in these two coupling regions are different. This shows that we must distinguish between these regions and identify the location of the bulk transition.

5.5.4 $SO(5)$ and $SO(6)$

For both $SO(5)$ and $SO(6)$, β_c values for $L_t \geq 5$ are in the weak coupling region. As before, we obtain the continuum string tensions at each β_c. There were complications in doing this for both gauge groups. At volumes with smaller L_s, similar to those that we used for $SO(4)$ and $SO(N \geq 7)$, there were no obvious plateaus in the Polyakov loop masses. Instead, the mass values steadily decreased over large ranges, making it difficult to extract the string tensions. We found that this improved if we used volumes with larger L_s, although this also increased the Polyakov loop masses and hence increased their errors. For a temporal length $L_t = 1/(aT_c)$, we use volumes $L_s^2(L_s + 8)$ where $L_s/L_t \approx 3.2$. We list the critical temperature values for $SO(5)$ in Table 5.21 and $SO(6)$ in Table 5.22 and display the continuum extrapolation for $SO(5)$ in Figure 5.14 and for $SO(6)$ in Figure 5.15. In the case of $SO(5)$, unlike $SO(4)$, we did not find a good linear extrapolation in the strong coupling. For $SO(6)$, there is a good linear extrapolation at strong coupling and its continuum limit is within errors of the weak coupling value, unlike $SO(4)$. The continuum limits are

$$\begin{aligned}
&\frac{T_c}{\sqrt{\sigma}}(a=0) = 0.7595(81) \qquad \bar{\chi}^2_{\rm dof} = 0.94 \qquad SO(5) \\
&\frac{T_c}{\sqrt{\sigma}}(a=0) = 0.8105(42) \qquad \bar{\chi}^2_{\rm dof} = 0.16 \qquad SO(6) \text{ (weak coupling)} \\
&\frac{T_c}{\sqrt{\sigma}}(a=0) = 0.8144(20) \qquad \bar{\chi}^2_{\rm dof} = 0.59 \qquad SO(6) \text{ (strong coupling)}
\end{aligned} \tag{5.49}$$

We note that these fits are very good with low $\bar{\chi}^2_{\rm dof}$.

5.5.5 $SO(7)$, $SO(8)$, $SO(9)$, $SO(12)$, and $SO(16)$

For these gauge groups, β_c values are in the weak coupling region for $L_t \geq 4$ for $SO(7)$ and $SO(8)$ and for $L_t \geq 3$ for $SO(9)$, $SO(12)$, and $SO(16)$. We list the critical temperature values for these groups in Tables 5.23, 5.24, 5.25, 5.26, and 5.27 and display the continuum extrapolations of the weak coupling values in Figures 5.16, 5.17, 5.18, 5.19 and 5.20. The continuum limits are

$$\begin{aligned}
&\frac{T_c}{\sqrt{\sigma}}(a=0) = 0.8351(38) && \bar{\chi}^2_{\text{dof}} = 0.98 && SO(7) \\
&\frac{T_c}{\sqrt{\sigma}}(a=0) = 0.8418(39) && \bar{\chi}^2_{\text{dof}} = 0.05 && SO(8) \\
&\frac{T_c}{\sqrt{\sigma}}(a=0) = 0.8515(14) && \bar{\chi}^2_{\text{dof}} = 0.30 && SO(9) \\
&\frac{T_c}{\sqrt{\sigma}}(a=0) = 0.8642(38) && \bar{\chi}^2_{\text{dof}} = 0.02 && SO(12) \\
&\frac{T_c}{\sqrt{\sigma}}(a=0) = 0.8780(38) && \bar{\chi}^2_{\text{dof}} = 0.15 && SO(16)
\end{aligned} \tag{5.50}$$

We note that these fits are very good with low $\bar{\chi}^2_{\text{dof}}$.

5.6 Large-N limits

We calculate the large-N limit of the $SO(N)$ deconfining temperatures. Given 't Hooft's argument that we explained previously, we expect the physics of an $SO(N)$ gauge theory to approach a large-N limit if we hold the 't Hooft coupling g^2N, or equivalently $\sqrt{\sigma}$, constant. Hence, we expect $T_c/\sqrt{\sigma}$ to converge to a large-N limit.

$$\lim_{N\to\infty} \frac{T_c}{\sqrt{\sigma}} = \left.\frac{T_c}{\sqrt{\sigma}}\right|_{SO(N\to\infty)} \tag{5.51}$$

Furthermore, if we apply 't Hooft's $1/N$ argument, we expect the leading correction to this limit at finite N to be $\mathcal{O}(1/N)$.

$$\left.\frac{T_c}{\sqrt{\sigma}}\right|_{SO(N\to\infty)} = \frac{T_c}{\sqrt{\sigma}} + \frac{c_1}{N} \tag{5.52}$$

for a constant c_1.

We list the $SO(N)$ deconfining temperatures in Table 5.28. We initially apply a linear fit in $1/\tilde{N}$ to $SO(2\tilde{N})$ values specifically to obtain the large-$\tilde{N}$ limit for two reasons. Firstly, we intend to compare this limit to the $SU(\tilde{N})$ large-$\tilde{N}$ limit because of the large-N orbifold equivalence. Secondly, $SO(2\tilde{N}+1)$ has a different centre to $SO(2\tilde{N})$, so the deconfinement properties might differ between the two sets of gauge theories. We display the large-$\tilde{N}$ extrapolation in Figure 5.21. The fit gives us a deconfining temperature at the large-N limit of

$$\left.\frac{T_c}{\sqrt{\sigma}}\right|_{SO(2\tilde{N}\to\infty)} = 0.9076(41) \qquad \bar{\chi}^2_{\text{dof}} = 2.82 \tag{5.53}$$

We see that the linear fit is reasonable and we get an accurate deconfining temperature at large-N.

We also note that if we used the deconfining temperature from $SO(4)$ strong coupling value then this would significantly disagree with the linear fit. This validates our decision to consider only the $SO(4)$ weak coupling value.

We now consider the $SO(2\tilde{N}+1)$ values in relation to the $SO(2\tilde{N})$ values. We see that the linear fit in Figure 5.21 agrees well with the $SO(7)$ and $SO(9)$ values but the $SO(5)$ deconfining temperature is significantly below the value what we would expect. This raises three possible explanations. Firstly, as we stated above $SO(5)$ does not have the $\mathbb{Z}_2$ centre symmetry of $SO(2\tilde{N})$ groups, so deconfinement might be different. However, the $SO(7)$ and $SO(9)$ deconfining temperatures also have trivial centres but do agree with the extrapolation through $SO(2\tilde{N})$ values. Secondly, we know that the $SO(5)$ deconfining phase transition is second order compared to the first order phase transitions for $SO(N \geq 6)$. However, the $SO(4)$ deconfining temperature also has a second order phase transition and seems to agree with the extrapolation through $SO(N \geq 6)$ values. Thirdly, there may be $\mathcal{O}(1/N^2)$ corrections to the large-N limit applying to the $SO(5)$ value although the $SO(4)$ deconfining temperature again agrees with the linear fit. It may be that a combination of these factors leads to this anomalous $SO(5)$ result. A linear fit through all $SO(N)$ values including the $SO(5)$ value would give us a large-N value of 0.9113(40) with a $\bar{\chi}^2_{\text{dof}} = 5.85$, more than double that of the $SO(2\tilde{N})$ value, despite the agreement among the $SO(2\tilde{N})$, $SO(7)$, and $SO(9)$ values. This demonstrates that the $SO(5)$ value greatly affects a linear fit.

5.7 Equivalences between $SO(N)$ and $SU(N)$ gauge theories

5.7.1 Lie algebra equivalences

We now compare the deconfining temperatures between specific $SO(N)$ and $SU(N)$ gauge theories whose gauge groups share Lie algebras.

We know that $SU(2) \times SU(2)$ and $SO(4)$ share a common Lie algebra so we could ask how the deconfining temperatures compare between $SO(4)$ and $SU(2)$. For the cross product group $SU(2) \times SU(2)$, we expect a contribution from each $SU(2)$ group to the string tension so that $\sigma|_{SU(2)\times SU(2)} = 2\,\sigma|_{SU(2)}$ Hence, we expect that

$$\left.\frac{T_c}{\sqrt{\sigma}}\right|_{SO(4)} = \left.\frac{T_c}{\sqrt{\sigma}}\right|_{SU(2)\times SU(2)} = \frac{1}{\sqrt{2}}\left.\frac{T_c}{\sqrt{\sigma}}\right|_{SU(2)} \tag{5.54}$$

We know that the $SU(2)$ deconfining temperature is $T_c/\sqrt{\sigma} = 1.1238(88)$ [50] so that we can

compare this to the value for the $SO(4)$ deconfining temperature.

$$\begin{aligned} \frac{T_c}{\sqrt{\sigma}} &= 0.7844(31) && SO(4) \\ \frac{1}{\sqrt{2}}\frac{T_c}{\sqrt{\sigma}} &= 0.7946(62) && SU(2) \end{aligned} \tag{5.55}$$

We see that these values are within 1.5σ of each other, which is consistent with the expectation (5.54). We also note that the $SO(4)$ and $SU(2)$ deconfining phase transitions are both second order.

We know that $SO(6)$ and $SU(4)$ share a common Lie algebra so we could ask how the deconfining temperatures compare between $SO(6)$ and $SU(4)$. As we discussed previously, the $SO(6)$ fundamental string tension is equivalent to the $SU(4)$ $k = 2A$ string tension so that we expect

$$\left.\frac{T_c}{\sqrt{\sigma_f}}\right|_{SO(6)} = \left.\frac{T_c}{\sqrt{\sigma_{2A}}}\right|_{SU(4)} \tag{5.56}$$

Hence, to compare between the $SO(6)$ and $SU(4)$ deconfining temperatures measured in fundamental string tension units, we use the ratio of the $SU(4)$ $k = 2A$ and fundamental string tensions in $D = 2+1$, $\sigma_{2A}/\sigma_f|_{SU(4)} = 1.355(9)$ [9]. We know that the $SU(4)$ deconfining temperature is $T_c/\sqrt{\sigma_f} = 0.9572(39)$ [50]. Hence, we can compare between the $SO(6)$ and $SU(4)$ mass spectra in the appropriate string tension units.

$$\begin{aligned} \frac{T_c}{\sqrt{\sigma_f}} &= 0.8105(42) && SO(6) \\ \frac{T_c}{\sqrt{\sigma_{2A}}} &= 0.8223(61) && SU(4) \end{aligned} \tag{5.57}$$

We see that these values are within 1.5σ of each other, which is consistent with the expectation (5.56). We also note that the $SO(6)$ and $SU(4)$ deconfining phase transitions are both weakly first order.

5.7.2 Large-N orbifold equivalence

We now compare the large-N limit of the $SO(2\tilde{N})$ and $SU(\tilde{N})$ deconfining temperatures. From the large-N equivalence, we expect that

$$\left.\frac{T_c}{\sqrt{\sigma}}\right|_{SO(2\tilde{N}\to\infty)} = \left.\frac{T_c}{\sqrt{\sigma}}\right|_{SU(\tilde{N}\to\infty)} \tag{5.58}$$

As stated in previous chapters, $SU(N)$ values have a $\mathcal{O}(1/N^2)$ correction to its large-N limit. We

use previous results for the $SU(\tilde{N})$ deconfining temperatures [50], choosing to apply a quadratic fit in $1/\tilde{N}$ to the data for $\tilde{N} \geq 3$. We list these $SO(2\tilde{N})$ and $SU(\tilde{N})$ continuum values in Table 5.29. We display the two large-$\tilde{N}$ extrapolations in Figure 5.22. The two large-$\tilde{N}$ limits are

$$\begin{aligned} \frac{T_c}{\sqrt{\sigma}} &= 0.9076(41) \qquad & SO(2\tilde{N} \to \infty) \\ \frac{T_c}{\sqrt{\sigma}} &= 0.9030(29) \qquad & SU(\tilde{N} \to \infty) \end{aligned} \tag{5.59}$$

We see that these two values agree within errors, validating the expectation from the large-N orbifold equivalence (5.58).

5.8 Data

Data Fit	β_c	$\chi(\beta_c)$	$\bar{\chi}^2_{\text{dof}}$
Reweighting	8.493(10)	25.40(30)	n/a
Gaussian	8.500(11)	25.66(40)	0.62
Logistic	8.500(6)	25.71(41)	0.64

Table 5.1: Comparisons between reweighting, Gaussian fits, and logistic fits to obtain β_c and $\chi(\beta_c)$ on an $SO(4)$ $40^2 4$ volume.

$L_s^2 L_t$	β_c	$\chi_{\lvert\overline{l_P}\rvert}$
$20^2 2$	6.4748(4)	10.77(4)
$24^2 2$	6.4771(4)	13.64(5)
$28^2 2$	6.4788(3)	16.80(9)
$32^2 2$	6.4797(3)	20.16(8)
$36^2 2$	6.4813(4)	23.65(12)
$40^2 2$	6.4819(3)	27.58(14)
$48^2 2$	6.4822(4)	35.15(43)
$56^2 2$	6.4840(4)	44.42(63)
$60^2 2$	6.4850(4)	49.92(89)
$80^2 2$	6.4853(4)	78.57(132)

$L_s^2 L_t$	β_c	$\chi_{\lvert\overline{l_P}\rvert}$
$32^2 3$	7.534(3)	19.60(14)
$36^2 3$	7.538(3)	23.22(16)
$40^2 3$	7.539(1)	26.37(25)
$44^2 3$	7.545(2)	31.09(38)
$48^2 3$	7.546(3)	35.56(38)
$52^2 3$	7.552(2)	40.58(53)
$66^2 3$	7.552(2)	58.75(131)
$80^2 3$	7.555(3)	81.02(193)
$90^2 3$	7.557(3)	95.80(171)
$40^2 4$	8.493(10)	25.40(30)
$48^2 4$	8.501(6)	33.88(56)
$56^2 4$	8.509(8)	42.02(93)
$64^2 4$	8.526(7)	51.67(120)
$72^2 4$	8.520(3)	59.46(140)
$80^2 4$	8.535(6)	66.44(173)
$88^2 4$	8.545(8)	75.23(296)

Table 5.2: β_c and $\chi_{\lvert\overline{l_P}\rvert}$ for $SO(4)$ $L_t \leq 4$ volumes.

$L_s^2 L_t$	β_c	$\chi_{\lvert\overline{l_P}\rvert}$
$36^2 6$	11.110(31)	20.68(18)
$48^2 6$	10.924(17)	28.87(36)
$60^2 6$	10.861(9)	38.76(53)
$72^2 6$	10.837(14)	47.33(83)
$84^2 6$	10.809(21)	57.82(125)
$96^2 6$	10.824(14)	70.28(199)
$120^2 6$	10.835(8)	95.57(321)
$42^2 7$	12.685(45)	29.41(38)
$56^2 7$	12.494(22)	41.46(64)
$70^2 7$	12.397(12)	54.24(94)
$84^2 7$	12.303(12)	68.11(111)
$98^2 7$	12.224(12)	81.74(172)
$112^2 7$	12.261(19)	100.03(247)
$126^2 7$	12.274(19)	117.10(302)

$L_s^2 L_t$	β_c	$\chi_{\lvert\overline{l_P}\rvert}$
$64^2 8$	14.005(37)	55.93(88)
$80^2 8$	13.836(24)	71.23(136)
$96^2 8$	13.901(16)	93.98(248)
$112^2 8$	13.712(16)	106.33(214)
$128^2 8$	13.736(14)	131.84(390)
$144^2 8$	13.767(20)	158.18(629)
$80^2 10$	17.096(31)	95.93(174)
$90^2 10$	16.919(35)	107.06(234)
$100^2 10$	16.870(24)	127.64(305)
$110^2 10$	16.790(53)	137.15(367)
$120^2 10$	16.731(24)	154.83(462)
$140^2 10$	16.725(23)	184.45(659)
$72^2 12$	20.648(62)	107.12(158)
$84^2 12$	20.202(66)	122.92(199)
$96^2 12$	20.098(52)	144.13(252)
$120^2 12$	19.797(29)	190.28(414)
$144^2 12$	19.757(27)	236.11(603)

Table 5.3: β_c and $\chi_{\lvert\overline{l_P}\rvert}$ for $SO(4)$ $L_t \geq 6$ volumes.

$L_s^2 L_t$	β_c	$\chi_{\lvert\overline{l_P}\rvert}$
$16^2 2$	10.380(1)	10.75(3)
$18^2 2$	10.378(1)	12.82(4)
$20^2 2$	10.378(1)	14.74(7)
$22^2 2$	10.376(1)	16.83(9)
$24^2 2$	10.377(2)	18.53(12)
$26^2 3$	12.058(3)	13.41(14)
$28^2 3$	12.054(3)	14.07(15)
$30^2 3$	12.049(3)	14.76(12)
$32^2 3$	12.053(4)	15.28(15)
$34^2 3$	12.049(4)	16.02(25)
$32^2 4$	13.964(10)	16.42(12)
$36^2 4$	13.964(9)	18.90(13)
$40^2 4$	13.955(7)	21.27(18)
$48^2 4$	13.962(12)	24.13(27)

$L_s^2 L_t$	β_c	$\chi_{\lvert\overline{l_P}\rvert}$
$40^2 5$	16.316(14)	20.75(14)
$44^2 5$	16.342(8)	24.15(23)
$50^2 5$	16.300(13)	26.37(20)
$54^2 5$	16.295(26)	27.87(18)
$60^2 5$	16.265(8)	30.58(29)
$70^2 5$	16.290(6)	35.40(40)
$42^2 6$	19.017(34)	28.35(49)
$48^2 6$	18.939(61)	31.74(41)
$54^2 6$	18.965(19)	36.39(49)
$60^2 6$	18.930(18)	40.39(76)
$56^2 7$	21.715(17)	46.57(67)
$60^2 7$	21.663(16)	48.70(77)
$64^2 7$	21.592(15)	53.02(81)
$68^2 7$	21.595(15)	55.50(90)
$72^2 7$	21.554(11)	58.01(99)

Table 5.4: β_c and $\chi_{\lvert\overline{l_P}\rvert}$ for $SO(5)$ volumes.

$L_s^2 L_t$	β_c	$\chi_{\lvert\overline{l_P}\rvert}$
$8^2 2$	15.175(2)	3.191(8)
$10^2 2$	15.185(1)	4.972(8)
$12^2 2$	15.192(1)	7.151(12)
$12^2 3$	17.810(9)	3.94(1)
$16^2 3$	17.793(4)	6.22(2)
$20^2 3$	17.821(4)	9.18(3)
$24^2 3$	17.831(4)	12.34(5)
$28^2 3$	17.833(3)	15.79(8)
$32^2 3$	17.839(3)	19.53(13)
$28^2 4$	21.295(6)	12.07(5)
$32^2 4$	21.358(8)	15.56(12)
$36^2 4$	21.356(8)	18.58(9)
$40^2 4$	21.352(4)	22.23(13)
$44^2 4$	21.370(6)	25.85(15)

$L_s^2 L_t$	β_c	$\chi_{\lvert\overline{l_P}\rvert}$
$28^2 5$	25.479(24)	14.25(8)
$32^2 5$	25.496(16)	17.77(12)
$40^2 5$	25.501(14)	25.25(18)
$48^2 5$	25.549(14)	33.99(38)
$56^2 5$	25.577(11)	44.40(41)
$60^2 5$	25.589(10)	48.77(68)
$42^2 6$	29.781(26)	31.45(18)
$48^2 6$	29.727(18)	38.65(30)
$54^2 6$	29.791(33)	47.09(75)
$60^2 6$	29.796(31)	55.66(75)
$66^2 6$	29.819(9)	65.52(89)
$44^2 7$	34.031(37)	38.73(30)
$50^2 7$	33.907(25)	46.75(48)
$56^2 7$	34.078(49)	57.24(96)
$60^2 7$	34.042(36)	62.06(65)
$64^2 7$	34.021(19)	69.71(85)
$68^2 7$	34.009(25)	75.83(107)
$72^2 7$	34.092(23)	83.87(143)

Table 5.5: β_c and $\chi_{\lvert\overline{l_P}\rvert}$ for $SO(6)$ volumes.

$L_s^2 L_t$	β_c	$\chi_{\lvert\overline{l_P}\rvert}$
$8^2 2$	20.963(3)	3.347(3)
$10^2 2$	20.960(3)	5.381(10)
$12^2 2$	20.953(3)	7.916(14)
$12^2 3$	25.148(29)	4.00(3)
$16^2 3$	25.022(14)	6.60(4)
$20^2 3$	24.982(13)	9.96(8)
$24^2 3$	24.988(5)	14.27(7)
$28^2 3$	25.011(7)	19.40(14)
$24^2 4$	30.721(24)	12.65(12)
$32^2 4$	30.714(21)	21.04(30)
$40^2 4$	30.721(7)	31.62(27)
$48^2 4$	30.727(6)	44.05(43)
$56^2 4$	30.726(8)	58.67(67)

$L_s^2 L_t$	β_c	$\chi_{\lvert\overline{l_P}\rvert}$
$32^2 5$	36.909(20)	23.75(21)
$40^2 5$	36.885(19)	35.40(43)
$48^2 5$	36.895(24)	50.05(80)
$56^2 5$	36.930(22)	66.59(110)
$64^2 5$	36.909(19)	83.37(151)
$52^2 6$	43.088(25)	62.57(104)
$56^2 6$	43.089(10)	72.92(93)
$60^2 6$	43.164(14)	83.65(127)
$64^2 6$	43.129(17)	94.02(115)

Table 5.6: β_c and $\chi_{\lvert\overline{l_P}\rvert}$ for $SO(7)$ volumes.

$L_s^2 L_t$	β_c	$\chi_{\lvert\overline{l_P}\rvert}$
$8^2 2$	27.583(4)	3.241(4)
$10^2 2$	27.594(3)	5.279(6)
$12^2 2$	27.605(3)	7.851(7)
$16^2 3$	33.488(22)	6.29(6)
$18^2 3$	33.503(17)	8.05(7)
$20^2 3$	33.468(13)	9.68(5)
$24^2 3$	33.521(8)	14.54(7)
$24^2 4$	41.573(14)	13.20(6)
$28^2 4$	41.600(18)	17.88(16)
$32^2 4$	41.631(14)	23.71(17)
$40^2 4$	41.686(14)	37.98(28)

$L_s^2 L_t$	β_c	$\chi_{\lvert\overline{l_P}\rvert}$
$32^2 5$	50.073(23)	25.70(27)
$40^2 5$	50.163(21)	40.21(40)
$48^2 5$	50.178(37)	58.72(72)
$56^2 5$	50.247(22)	81.93(90)
$42^2 6$	58.560(18)	46.27(34)
$48^2 6$	58.742(24)	63.38(78)
$54^2 6$	58.703(19)	79.59(60)
$60^2 6$	58.758(12)	101.15(99)

Table 5.7: β_c and $\chi_{\lvert\overline{l_P}\rvert}$ for $SO(8)$ volumes.

$L_s^2 L_t$	β_c	$\chi_{\lvert\overline{l_P}\rvert}$
$16^2 3$	43.443(9)	6.79(2)
$18^2 3$	43.425(6)	8.64(2)
$20^2 3$	43.427(7)	10.80(4)
$22^2 3$	43.431(7)	13.26(5)
$24^2 3$	43.460(7)	16.16(5)
$26^2 3$	43.457(6)	19.17(6)
$30^2 3$	43.424(7)	25.59(9)
$36^2 3$	43.433(12)	37.59(26)
$42^2 3$	43.399(8)	51.23(30)

$L_s^2 L_t$	β_c	$\chi_{\lvert\overline{l_P}\rvert}$
$20^2 4$	54.449(28)	10.96(10)
$24^2 4$	54.375(28)	15.93(14)
$28^2 4$	54.393(19)	22.01(16)
$32^2 4$	54.505(17)	30.22(18)
$40^2 4$	54.464(14)	48.16(26)
$48^2 4$	54.434(12)	70.28(55)
$24^2 5$	65.634(38)	16.87(9)
$28^2 5$	65.654(46)	23.34(16)
$32^2 5$	65.661(38)	31.17(22)
$36^2 5$	65.674(15)	40.16(22)
$40^2 5$	65.648(20)	50.10(36)
$48^2 5$	65.760(17)	75.33(53)

Table 5.8: β_c and $\chi_{\lvert\overline{l_P}\rvert}$ for $SO(9)$ volumes.

$L_s^2 L_t$	β_c	$\chi_{\lvert\overline{l_P}\rvert}$
$6^2 2$	63.57(1)	1.593(1)
$7^2 2$	63.59(1)	2.248(1)
$8^2 2$	63.58(1)	3.014(3)
$8^2 3$	80.72(1)	1.620(3)
$10^2 3$	80.83(1)	2.640(8)
$12^2 3$	80.96(1)	4.043(8)
$14^2 3$	81.05(1)	5.800(16)
$16^2 3$	81.12(1)	7.929(17)

$L_s^2 L_t$	β_c	$\chi_{\lvert\overline{l_P}\rvert}$
$12^2 4$	101.81(5)	3.995(25)
$16^2 4$	102.11(8)	7.619(84)
$20^2 4$	102.19(4)	12.739(71)
$24^2 4$	102.28(4)	19.393(88)
$16^2 5$	123.03(10)	7.709(60)
$20^2 5$	123.26(8)	12.988(104)
$24^2 5$	123.52(4)	19.769(137)
$28^2 5$	123.62(6)	27.835(284)

Table 5.9: β_c and $\chi_{\lvert\overline{l_P}\rvert}$ for $SO(12)$ volumes.

$L_s^2 L_t$	β_c	$\chi_{\lvert\overline{l_P}\rvert}$
$4^2 2$	114.85(2)	0.595(1)
$5^2 2$	114.82(2)	0.998(2)
$6^2 2$	114.84(2)	1.512(3)
$6^2 3$	149.17(2)	0.940(2)
$8^2 3$	149.32(2)	1.832(3)
$10^2 3$	149.58(3)	3.141(4)
$12^2 3$	149.76(2)	4.839(10)
$14^2 3$	149.89(3)	6.897(20)

$L_s^2 L_t$	β_c	$\chi_{\lvert\overline{l_P}\rvert}$
$6^2 4$	192.07(26)	1.016(7)
$8^2 4$	189.04(32)	1.804(25)
$10^2 4$	188.91(17)	3.011(42)
$12^2 4$	189.13(11)	4.617(47)
$14^2 4$	189.33(11)	6.725(74)
$16^2 4$	189.55(6)	9.221(40)
$8^2 5$	230.62(44)	1.972(18)
$10^2 5$	229.42(56)	3.013(44)
$12^2 5$	228.60(5)	4.591(14)
$14^2 5$	228.77(6)	6.572(18)
$16^2 5$	229.01(7)	9.036(31)
$20^2 5$	229.51(12)	15.429(88)

Table 5.10: β_c and $\chi_{\lvert\overline{l_P}\rvert}$ for $SO(16)$ volumes.

L_t	$\beta_c(V \to \infty)$	L_s range	$\bar{\chi}^2_{\text{dof}}$
2	6.4863(3)	$L_s \geq 32$	1.98
3	7.560(2)	$L_s \geq 32$	2.78
4	8.547(6)	$L_s \geq 48$	1.67
6	10.819(10)	$L_s \geq 60$	1.23
7	12.163(12)	$L_s \geq 42$	5.37
8	13.660(17)	$L_s \geq 64$	13.22
10	16.554(42)	$L_s \geq 90$	0.95
12	19.432(37)	$L_s \geq 72$	2.43

Table 5.11: Infinite volume limits $\beta_c(V \to \infty)$, extrapolation range, and $\bar{\chi}^2_{\text{dof}}$ for $SO(4)$ volumes.

L_t	$\beta_c(V \to \infty)$	L_s range	$\bar{\chi}^2_{\text{dof}}$
2	10.373(2)	$L_s \geq 16$	0.71
3	12.036(8)	$L_s \geq 26$	0.46
4	13.951(19)	$L_s \geq 32$	0.32
5	16.251(10)	$L_s \geq 40$	4.82
6	18.857(46)	$L_s \geq 42$	0.44
7	21.312(36)	$L_s \geq 56$	1.24

Table 5.12: Infinite volume limits $\beta_c(V \to \infty)$, extrapolation range, and $\bar{\chi}^2_{\text{dof}}$ for $SO(5)$ volumes.

L_t	$\beta_c(V \to \infty)$	L_s range	$\bar{\chi}^2_{\text{dof}}$
2	15.205(3)	$L_s \geq 8$	0.62
3	17.854(3)	$L_s \geq 12$	0.83
4	21.399(6)	$L_s \geq 28$	6.42
5	25.613(11)	$L_s \geq 28$	2.25
6	29.872(21)	$L_s \geq 42$	2.79
7	34.113(32)	$L_s \geq 44$	4.44

Table 5.13: Infinite volume limits $\beta_c(V \to \infty)$, extrapolation range, and $\bar{\chi}^2_{\text{dof}}$ for $SO(6)$ volumes.

L_t	$\beta_c(V \to \infty)$	L_s range	$\bar{\chi}^2_{\text{dof}}$
2	20.947(6)	$L_s \geq 8$	0.82
3	24.992(11)	$L_s \geq 12$	5.46
4	30.729(9)	$L_s \geq 24$	0.14
5	36.913(20)	$L_s \geq 32$	0.81
6	43.311(62)	$L_s \geq 52$	5.00

Table 5.14: Infinite volume limits $\beta_c(V \to \infty)$, extrapolation range, and $\bar{\chi}^2_{\text{dof}}$ for $SO(7)$ volumes.

L_t	$\beta_c(V \to \infty)$	L_s range	$\bar{\chi}^2_{\text{dof}}$
2	27.622(5)	$L_s \geq 8$	0.66
3	33.547(21)	$L_s \geq 16$	4.06
4	41.769(32)	$L_s \geq 24$	0.22
5	50.319(32)	$L_s \geq 32$	0.46
6	58.935(29)	$L_s \geq 42$	6.65

Table 5.15: Infinite volume limits $\beta_c(V \to \infty)$, extrapolation range, and $\bar{\chi}^2_{\text{dof}}$ for $SO(8)$ volumes.

L_t	$\beta_c(V \to \infty)$	L_s range	$\bar{\chi}^2_{\text{dof}}$
3	43.450(7)	$L_s \geq 16$	6.10
4	54.457(13)	$L_s \geq 20$	6.78
5	65.678(32)	$L_s \geq 24$	0.47

Table 5.16: Infinite volume limits $\beta_c(V \to \infty)$, extrapolation range, and $\bar{\chi}^2_{\text{dof}}$ for $SO(9)$ volumes.

L_t	$\beta_c(V \to \infty)$	L_s range	$\bar{\chi}^2_{\text{dof}}$
2	63.610(14)	$L_s \geq 6$	3.35
3	81.299(17)	$L_s \geq 8$	0.70
4	102.424(45)	$L_s \geq 12$	0.16
5	124.011(15)	$L_s \geq 16$	0.34

Table 5.17: Infinite volume limits $\beta_c(V \to \infty)$, extrapolation range, and $\bar{\chi}^2_{\text{dof}}$ for $SO(12)$ volumes.

L_t	$\beta_c(V \to \infty)$	L_s range	$\bar{\chi}^2_{\text{dof}}$
2	114.824(35)	$L_s \geq 4$	0.66
3	150.128(33)	$L_s \geq 8$	0.83
4	189.975(14)	$L_s \geq 12$	0.19
5	230.096(212)	$L_s \geq 14$	1.06

Table 5.18: Infinite volume limits $\beta_c(V \to \infty)$, extrapolation range, and $\bar{\chi}^2_{\text{dof}}$ for $SO(16)$ volumes.

$SO(N)$	$L_s^2 L_t$	Bulk transition	Weak coupling region
4	$20^2 24$	$\beta \in [9.1, 10.2]$	$L_t \geq 6$
5	$12^2 24$	$\beta \in [13.5, 15.4]$	$L_t \geq 5$
6	$12^2 24$	$\beta \in [18.0, 21.3]$	$L_t \geq 5$
7	$8^2 24$	$\beta \in [23.5, 28.0]$	$L_t \geq 4$
8	$8^2 24$	$\beta \in [31, 35]$	$L_t \geq 4$
9	$4^2 24$	$\beta \in [37, 42]$	$L_t \geq 3$
12	$4^2 24$	$\beta \in [65, 73]$	$L_t \geq 3$
16	$2^2 24$	$\beta \in [111, 124]$	$L_t \geq 3$

Table 5.19: Bounds for the $D = 2 + 1$ bulk transition calculated on volumes $L_s^2 L_t$.

L_t	$\beta_c(V \to \infty)$	$a\sqrt{\sigma}$	$T_c/\sqrt{\sigma}$	Coupling
2	6.4863(3)	0.6216(2)	0.8044(3)	
3	7.560(2)	0.3988(5)	0.8358(11)	Strong
4	8.547(6)	0.2956(7)	0.8458(21)	
6	10.819(10)	0.2134(14)	0.7810(51)	
7	12.163(12)	0.1818(7)	0.7858(30)	
8	13.660(17)	0.1591(6)	0.7856(28)	Weak
10	16.554(42)	0.1278(9)	0.7825(55)	
12	19.432(37)	0.1065(7)	0.7828(48)	

Table 5.20: $SO(4)$ critical temperatures in string tension units $T_c/\sqrt{\sigma}$ and string tension $a\sqrt{\sigma}$, evaluated at the infinite volume limit $\beta_c(V \to \infty)$.

L_t	$\beta_c(V \to \infty)$	$a\sqrt{\sigma}$	$T_c/\sqrt{\sigma}$	Coupling
2	10.373(2)	0.6437(11)	0.7767(13)	
3	12.036(8)	0.4236(12)	0.7870(23)	Strong
4	13.951(19)	0.3212(8)	0.7784(20)	
5	16.251(10)	0.2579(13)	0.7756(39)	
6	18.857(46)	0.2153(10)	0.7743(35)	Weak
7	21.312(36)	0.1863(8)	0.7668(35)	

Table 5.21: $SO(5)$ critical temperatures in string tension units $T_c/\sqrt{\sigma}$ and string tension $a\sqrt{\sigma}$, evaluated at the infinite volume limit $\beta_c(V \to \infty)$.

L_t	$\beta_c(V \to \infty)$	$a\sqrt{\sigma}$	$T_c/\sqrt{\sigma}$	Coupling
2	15.205(3)	0.6535(13)	0.7651(15)	
3	17.854(3)	0.4201(7)	0.7935(13)	Strong
4	21.399(6)	0.3106(10)	0.8050(27)	
5	25.613(11)	0.2501(7)	0.7996(22)	
6	29.872(21)	0.2077(3)	0.8024(14)	Weak
7	34.113(32)	0.1774(4)	0.8053(19)	

Table 5.22: $SO(6)$ critical temperatures in string tension units $T_c/\sqrt{\sigma}$ and string tension $a\sqrt{\sigma}$, evaluated at the infinite volume limit $\beta_c(V \to \infty)$.

L_t	$\beta_c(V \to \infty)$	$a\sqrt{\sigma}$	$T_c/\sqrt{\sigma}$	Coupling
2	20.947(6)	0.6571(8)	0.7610(10)	Strong
3	24.992(11)	0.4181(7)	0.7972(13)	
4	30.729(9)	0.3104(5)	0.8053(12)	
5	36.913(20)	0.2455(7)	0.8147(22)	Weak
6	43.311(62)	0.2023(6)	0.8239(26)	

Table 5.23: $SO(7)$ critical temperatures in string tension units $T_c/\sqrt{\sigma}$ and string tension $a\sqrt{\sigma}$, evaluated at the infinite volume limit $\beta_c(V \to \infty)$.

L_t	$\beta_c(V \to \infty)$	$a\sqrt{\sigma}$	$T_c/\sqrt{\sigma}$	Coupling
2	27.622(5)	0.6586(8)	0.7591(9)	Strong
3	33.547(21)	0.4179(7)	0.7977(14)	
4	41.769(32)	0.3051(11)	0.8193(28)	
5	50.319(32)	0.2415(4)	0.8281(15)	Weak
6	58.935(29)	0.2003(5)	0.8320(20)	

Table 5.24: $SO(8)$ critical temperatures in string tension units $T_c/\sqrt{\sigma}$ and string tension $a\sqrt{\sigma}$, evaluated at the infinite volume limit $\beta_c(V \to \infty)$.

L_t	$\beta_c(V \to \infty)$	$a\sqrt{\sigma}$	$T_c/\sqrt{\sigma}$	Coupling
3	43.450(7)	0.4150(2)	0.8032(4)	
4	54.457(13)	0.3025(4)	0.8263(11)	Weak
5	65.678(32)	0.2395(3)	0.8351(12)	

Table 5.25: $SO(9)$ critical temperatures in string tension units $T_c/\sqrt{\sigma}$ and string tension $a\sqrt{\sigma}$, evaluated at the infinite volume limit $\beta_c(V \to \infty)$.

L_t	$\beta_c(V \to \infty)$	$a\sqrt{\sigma}$	$T_c/\sqrt{\sigma}$	Coupling
2	63.610(14)	0.6600(24)	0.7576(27)	Strong
3	81.299(17)	0.4070(6)	0.8191(12)	
4	102.424(45)	0.2977(6)	0.8399(18)	Weak
5	124.011(15)	0.2354(12)	0.8497(43)	

Table 5.26: $SO(12)$ critical temperatures in string tension units $T_c/\sqrt{\sigma}$ and string tension $a\sqrt{\sigma}$, evaluated at the infinite volume limit $\beta_c(V \to \infty)$.

L_t	$\beta_c(V \to \infty)$	$a\sqrt{\sigma}$	$T_c/\sqrt{\sigma}$	Coupling
2	63.610(14)	0.6438(25)	0.7766(31)	Strong
3	81.299(17)	0.4003(12)	0.8328(24)	
4	102.424(45)	0.2925(9)	0.8547(26)	Weak
5	124.011(15)	0.2320(7)	0.8622(28)	

Table 5.27: $SO(16)$ critical temperatures in string tension units $T_c/\sqrt{\sigma}$ and string tension $a\sqrt{\sigma}$, evaluated at the infinite volume limit $\beta_c(V \to \infty)$.

$SO(N)$	$T_c/\sqrt{\sigma}$	$\bar{\chi}^2_{\rm dof}$
4	0.7844(51)	0.36
5	0.7595(81)	0.94
6	0.8105(42)	0.16
7	0.8351(38)	0.98
8	0.8418(39)	0.05
9	0.8515(15)	0.30
12	0.8642(38)	0.02
16	0.8780(38)	0.15

Table 5.28: $SO(N)$ continuum limits of the deconfining temperatures in string tension units $T_c/\sqrt{\sigma}$ and extrapolation $\bar{\chi}^2_{\rm dof}$.

$\tilde{N}$	$SO(2\tilde{N})$	$SU(\tilde{N})$
2	0.7844(51)	1.1238(88)
3	0.8105(42)	0.9994(40)
4	0.8418(39)	0.9572(39)
5		0.9380(19)
6	0.8642(38)	0.9300(48)
8	0.8780(38)	0.9144(41)

Table 5.29: $SO(2\tilde{N})$ and $SU(\tilde{N})$ [50] continuum limits of the deconfining temperatures in string tension units $T_c/\sqrt{\sigma}$.

5.9 Figures

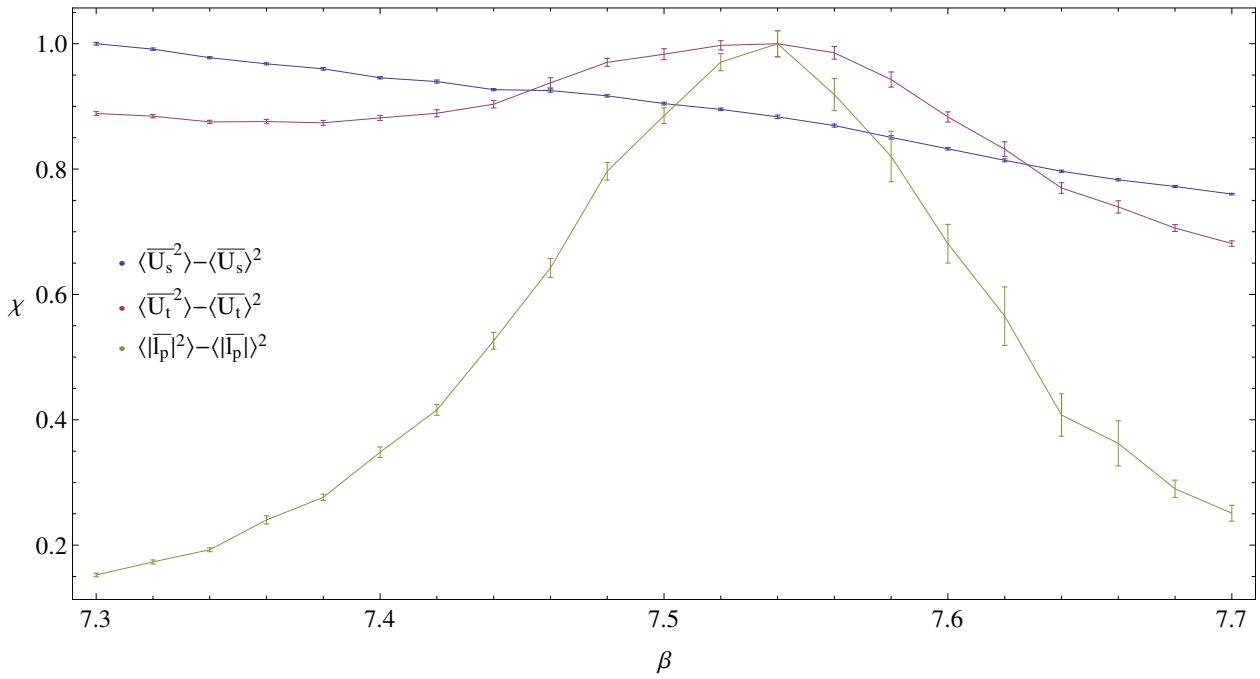

Figure 5.1: Normalised susceptibility plots for the spatial plaquette $\overline{U}_s$, the temporal plaquette $\overline{U}_t$, and the Polyakov loop $\left|\overline{l_P}\right|$ for an $SO(4)$ 32^23 volume.

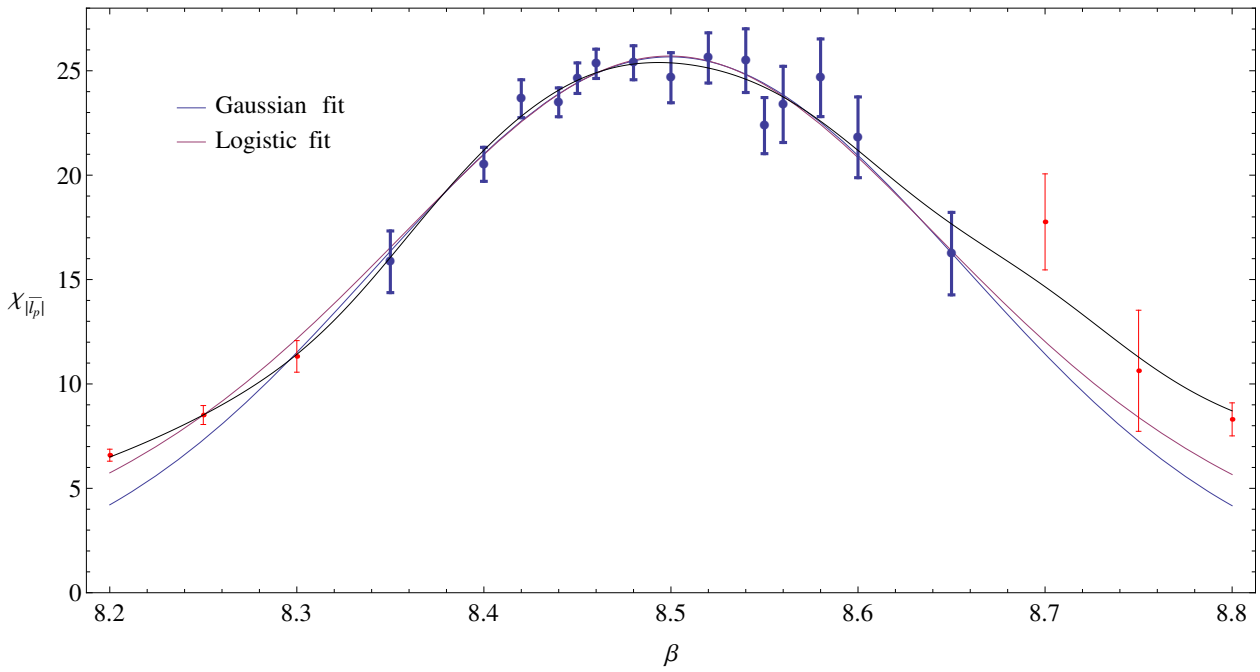

Figure 5.2: Curve fitting to susceptibility data for a $SO(4)$ 40^24 volume. The points represent calculations of the susceptibility at specific β values while the black line represents reweighted values. For the curve fitting, we used the data from the blue points rather than the red points to reduce the $\bar{\chi}^2_{\text{dof}}$ of the fits.

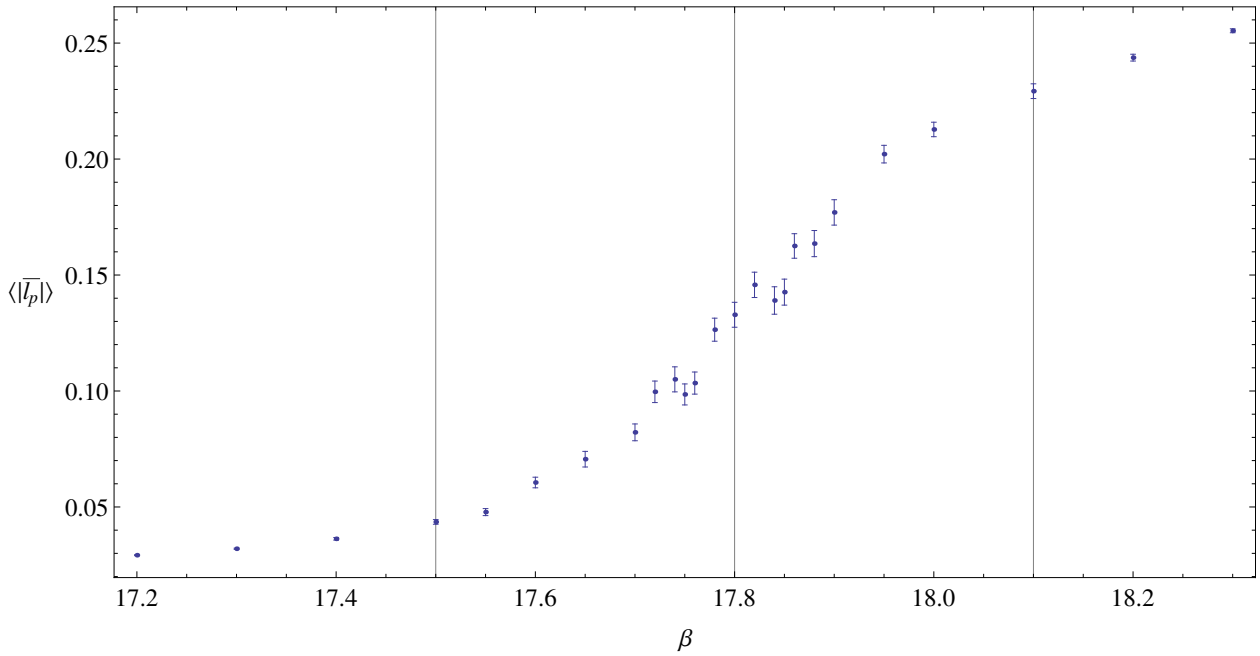

Figure 5.3: The Polyakov loop $\langle|\overline{l_P}|\rangle$ for an $SO(6)$ $20^2 3$ volume. The vertical lines correspond to the three characteristic values $\beta = \beta_- < \beta_0 < \beta_+$.

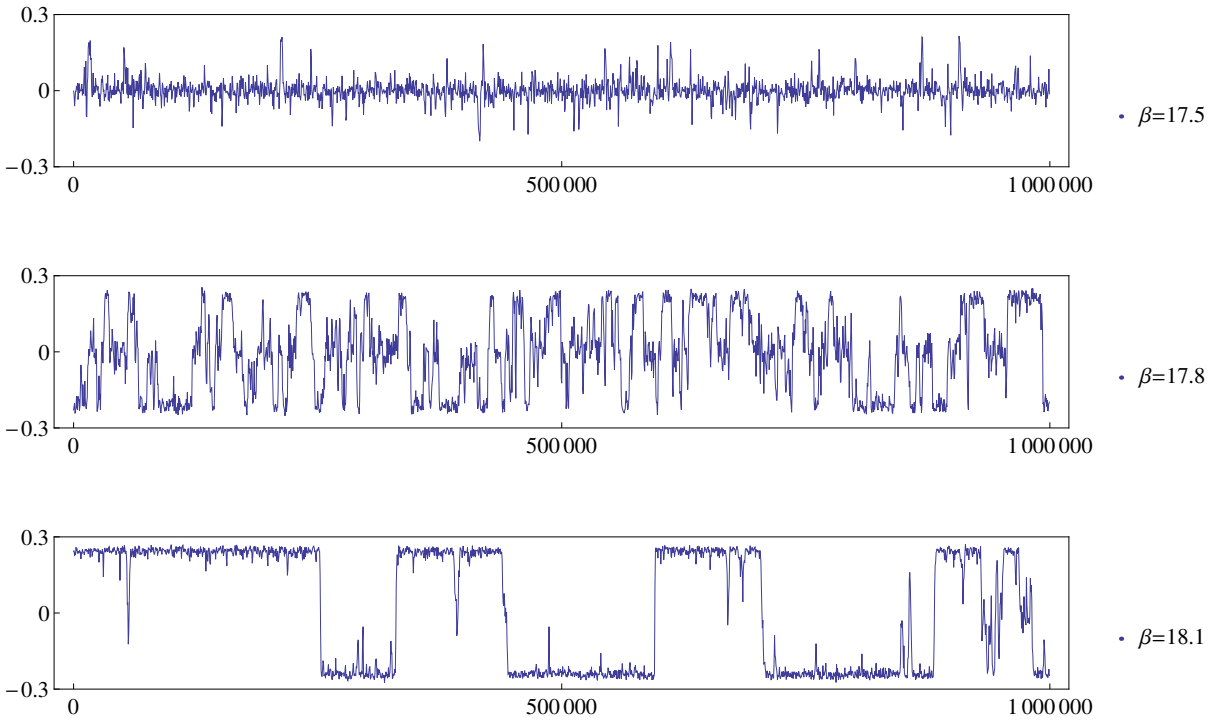

Figure 5.4: The Polyakov loop $\overline{l_P}$ history plots at three characteristic β values for an $SO(6)$ $20^2 3$ volume over a run of a million configurations.

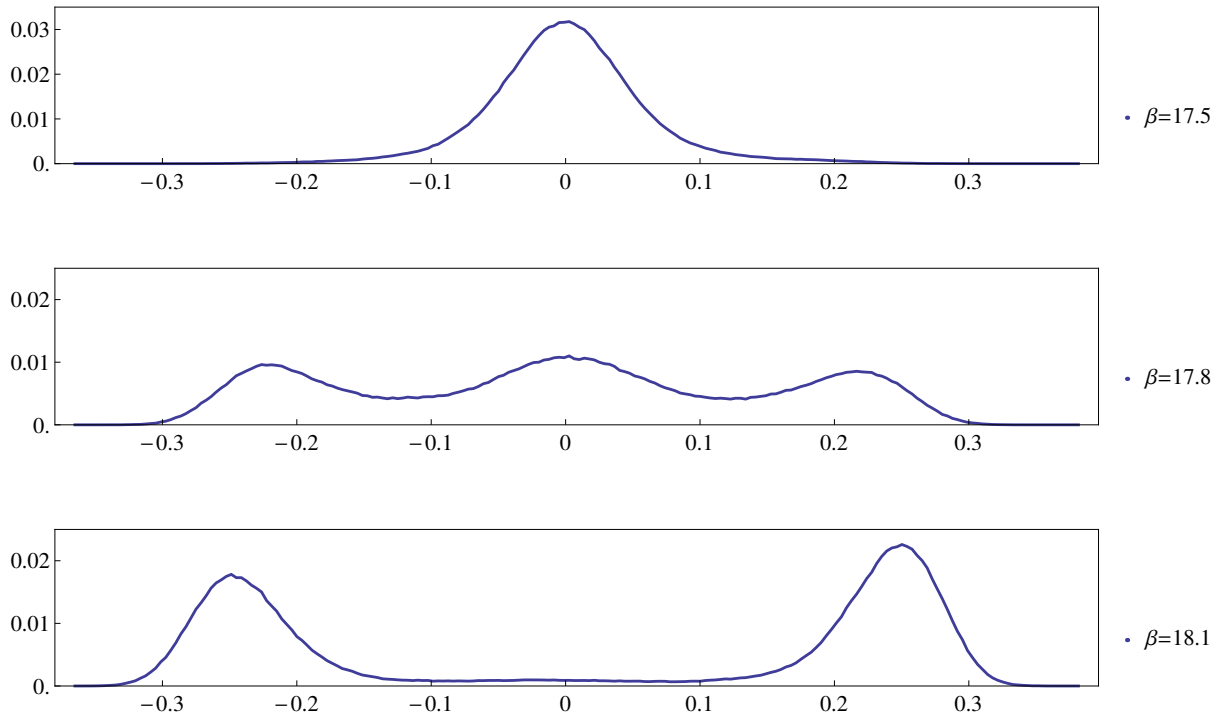

Figure 5.5: The Polyakov loop $\overline{l_P}$ histograms at three characteristic β values for an $SO(6)$ $20^2 3$ volume.

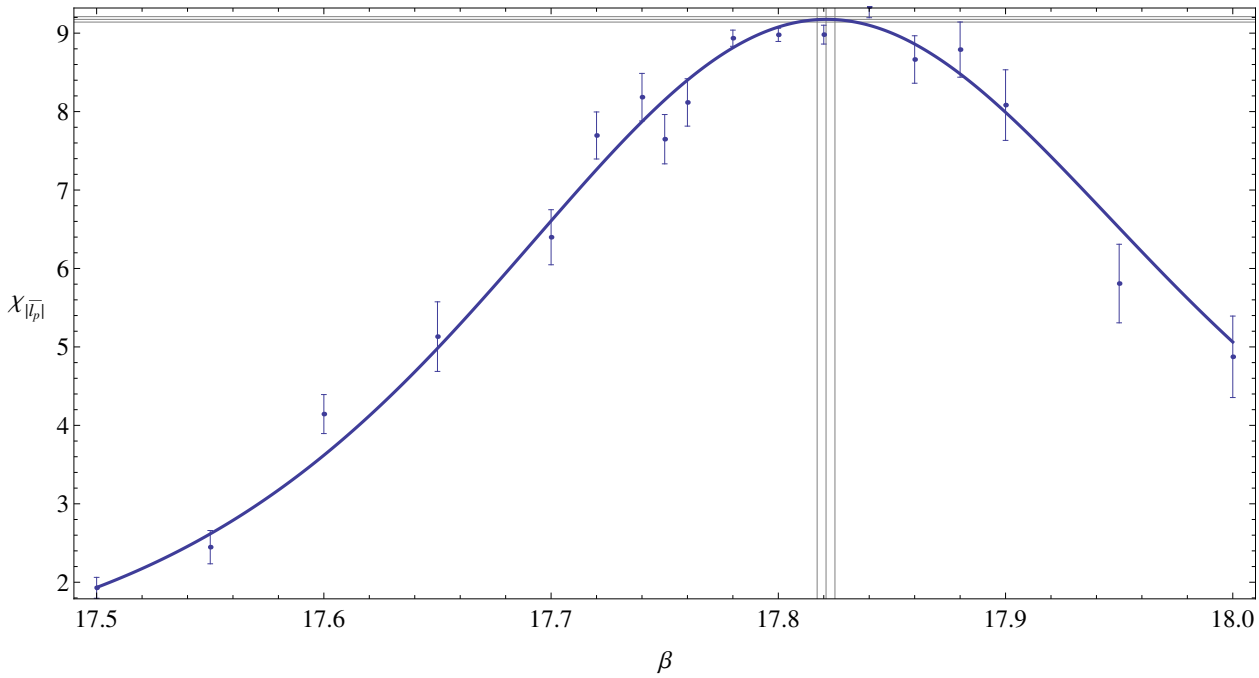

Figure 5.6: The reweighted susceptibility $\chi_{|\overline{l_P}|}$ (along with original susceptibility data) for an $SO(6)$ $20^2 3$ volume. The points represent the calculated susceptibility at specific β values whereas the line represents the reweighted values. The vertical and horizontal lines correspond to the maximum susceptibility values along with its error. We find that $\beta_c = 17.821(4)$ and $\chi_{|\overline{l_P}|}(\beta_c) = 9.18(3)$

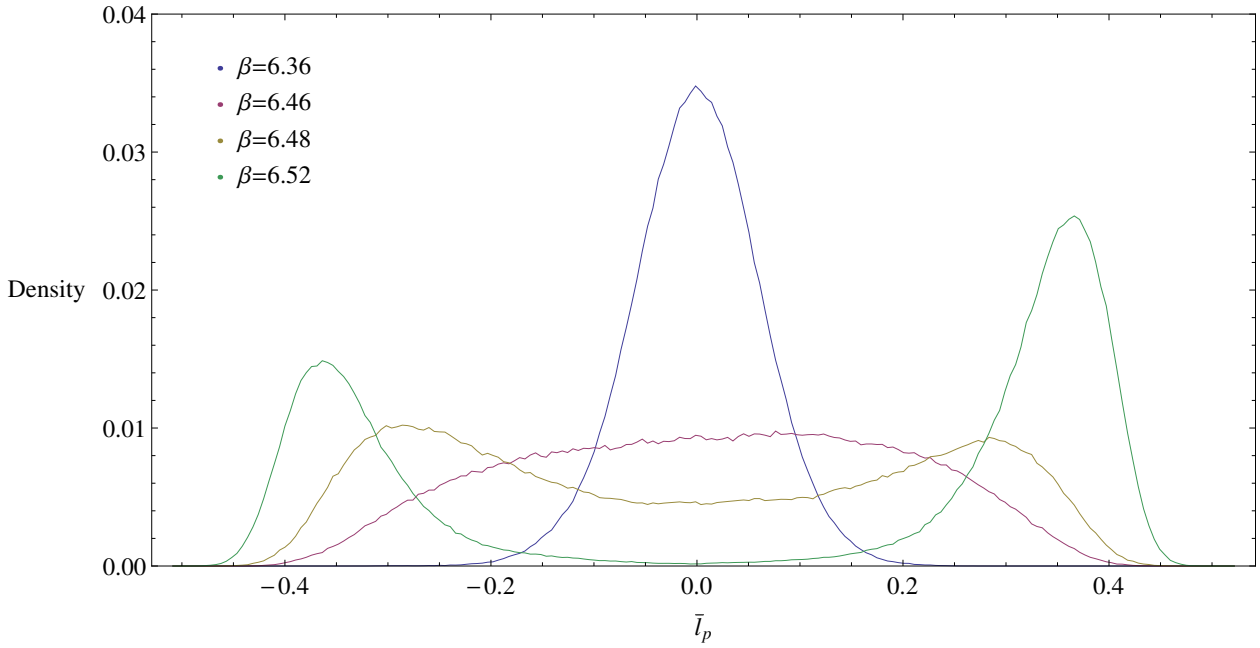

Figure 5.7: The Polyakov loop $\overline{l_P}$ histograms for an $SO(4)$ $28^2 2$ volume.

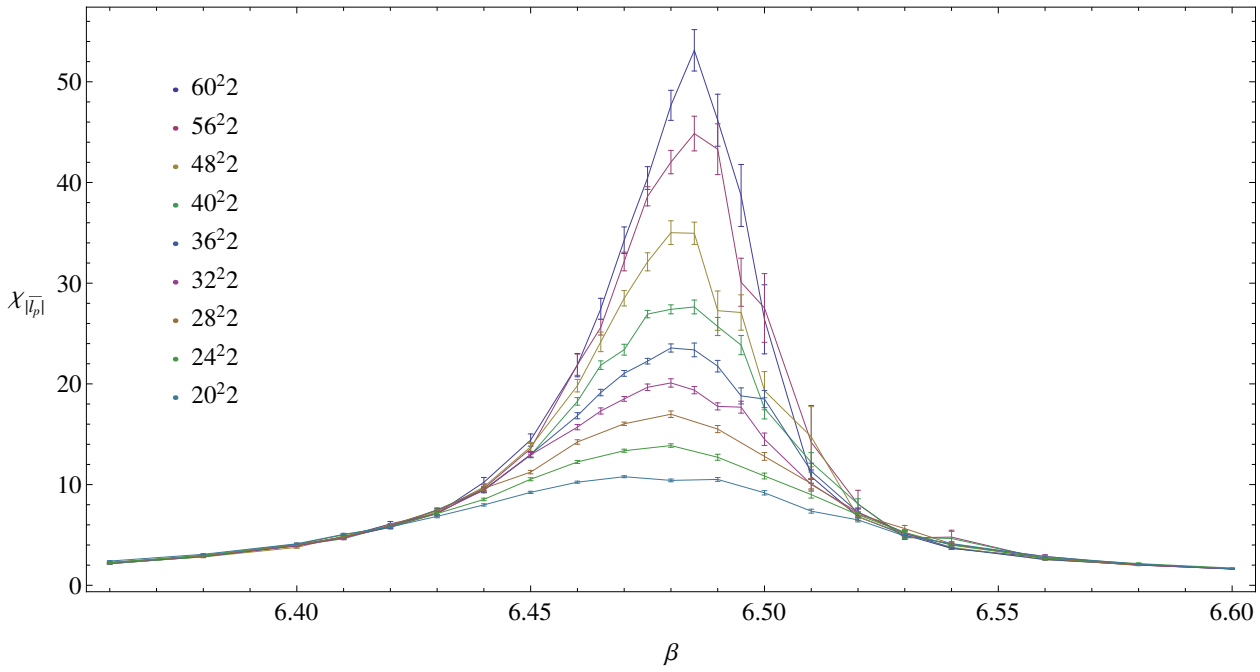

Figure 5.8: The Polyakov loop susceptibility for $SO(4)$ $L_t = 2$ volumes.

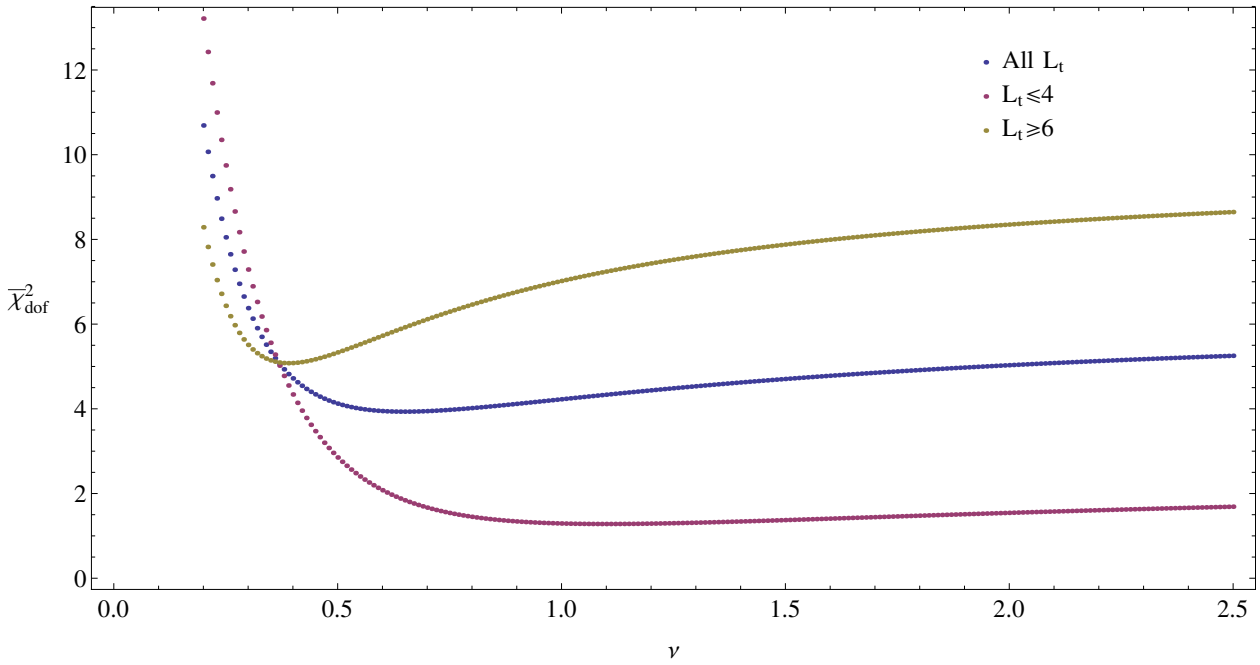

Figure 5.9: $\bar{\chi}^2_{\rm dof}$ against the critical exponent ν when fitting to all $SO(4)$ data (blue), all data with $L_t \leq 4$ (red), and all data with $L_t \geq 6$ (yellow). The minimum $\bar{\chi}^2_{\rm dof}$ of the blue plot is at $\nu = 0.65(7)$, the red plot at 1.10(22), and the yellow plot at 0.39(4).

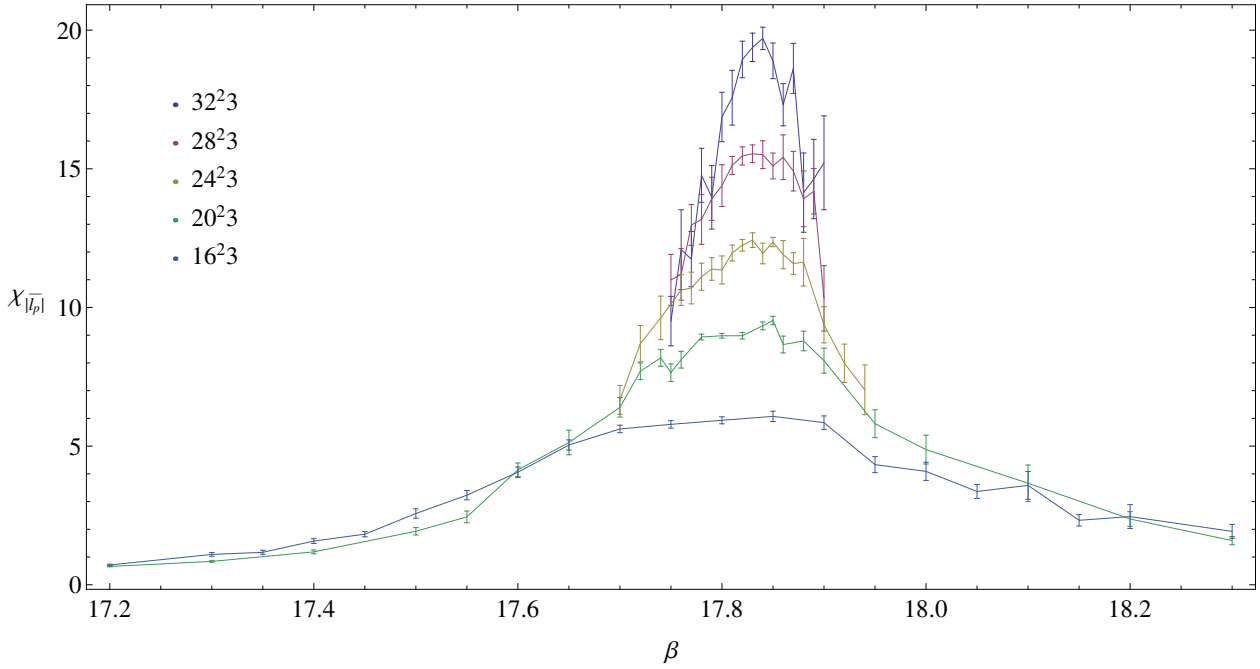

Figure 5.10: The Polyakov loop susceptibility for $SO(6)$ $L_t = 3$ volumes.

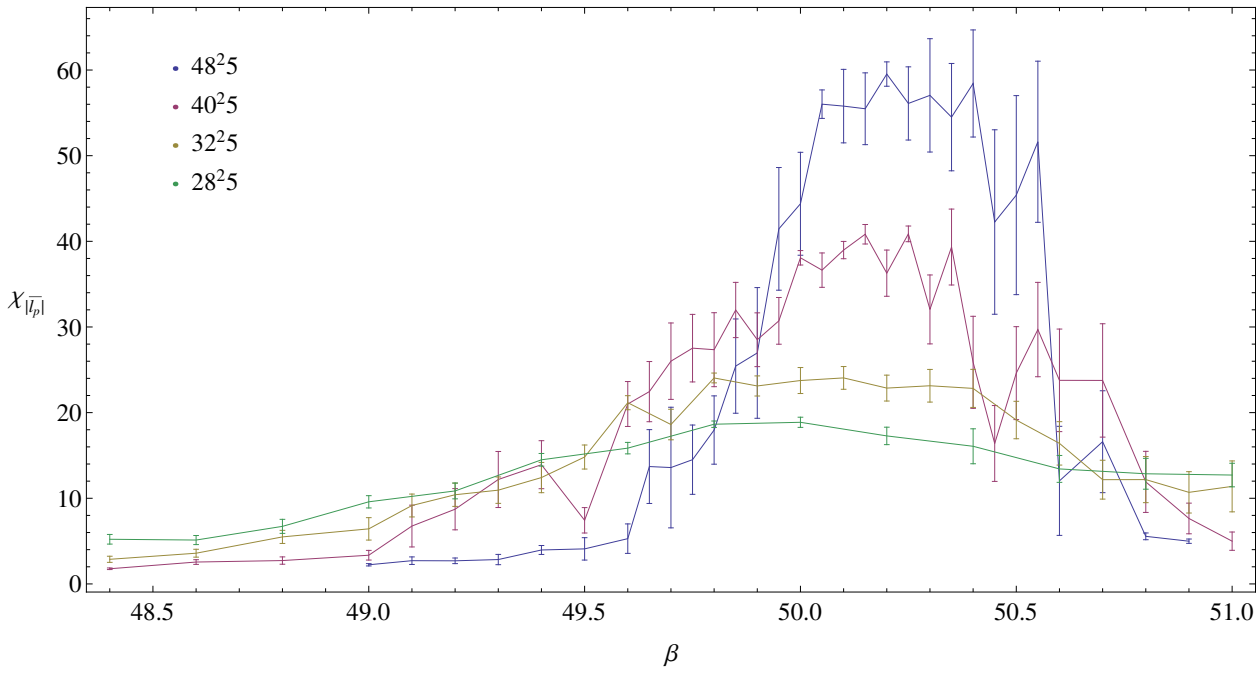

Figure 5.11: The Polyakov loop susceptibility for $SO(8)$ $L_t = 5$ volumes.

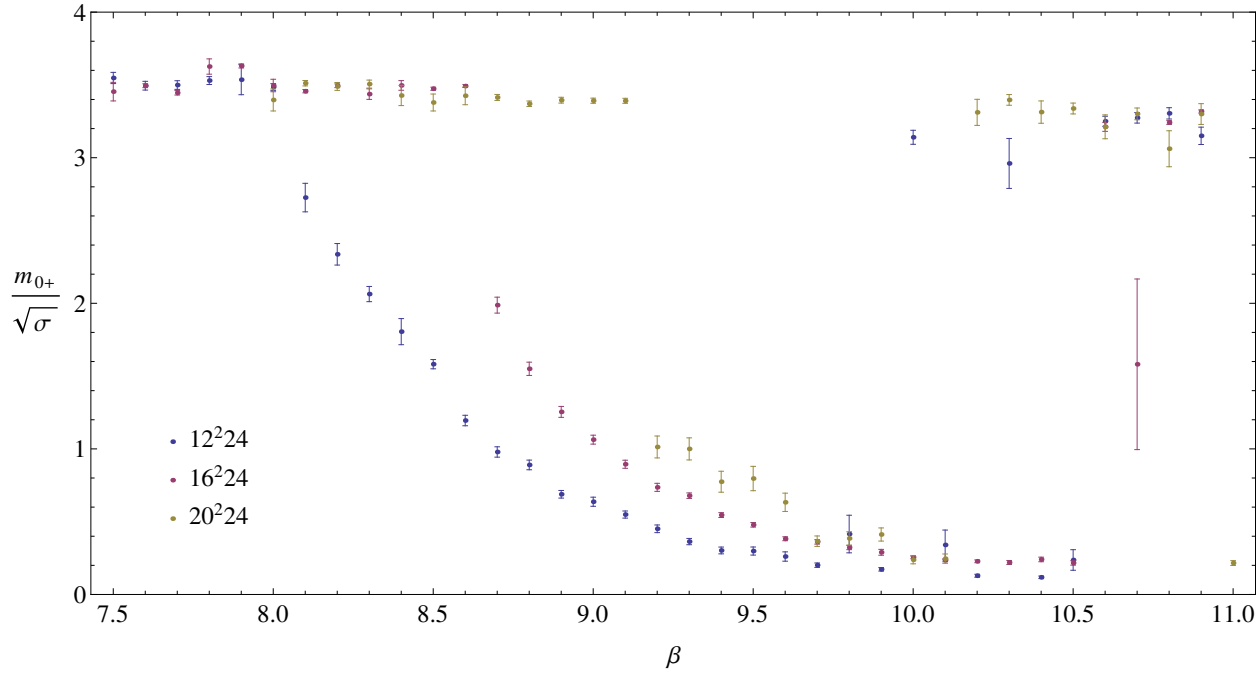

Figure 5.12: The scalar glueball mass in string tension units $m_G/\sqrt{\sigma}$ for three different $SO(4)$ volumes. The decrease in the glueball mass corresponds to the region of the bulk transition.

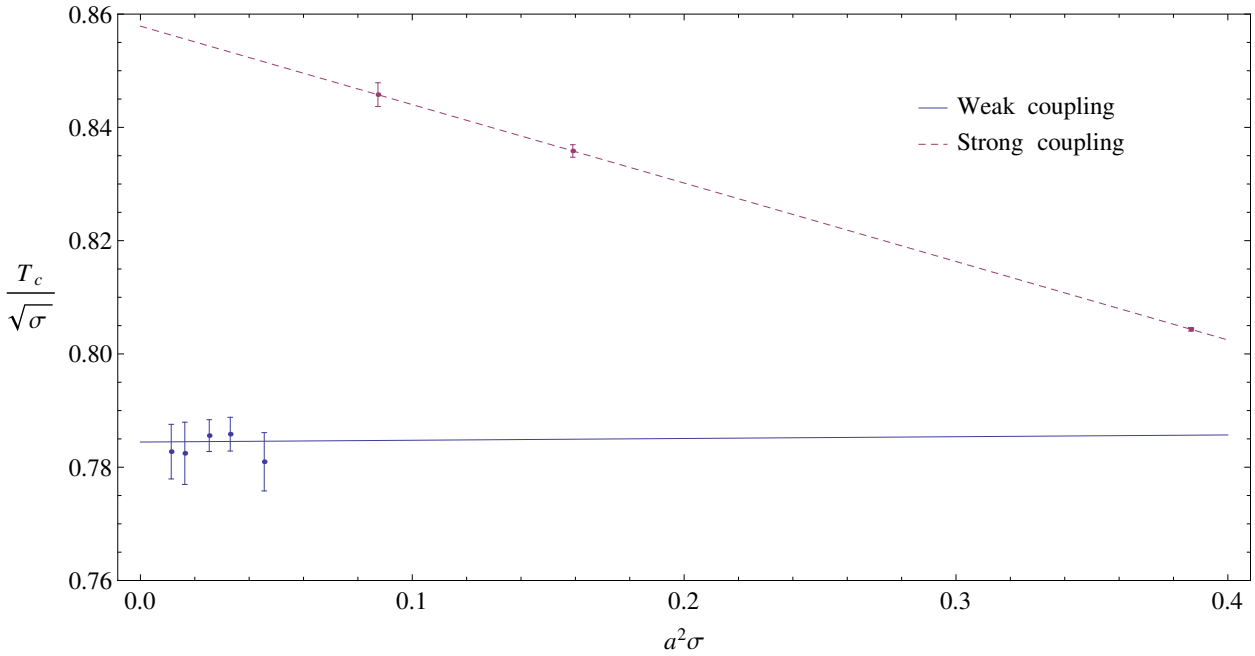

Figure 5.13: Continuum extrapolation of $SO(4)$ deconfining temperatures in string tension units.

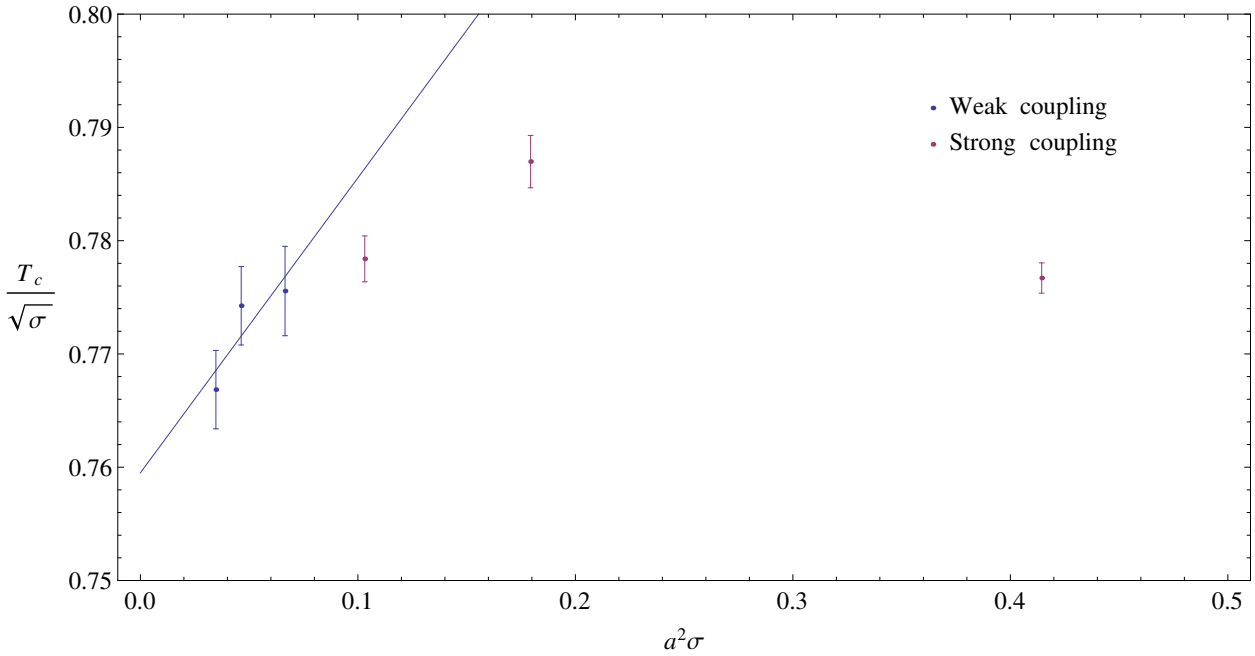

Figure 5.14: Continuum extrapolation of $SO(5)$ deconfining temperatures in string tension units.

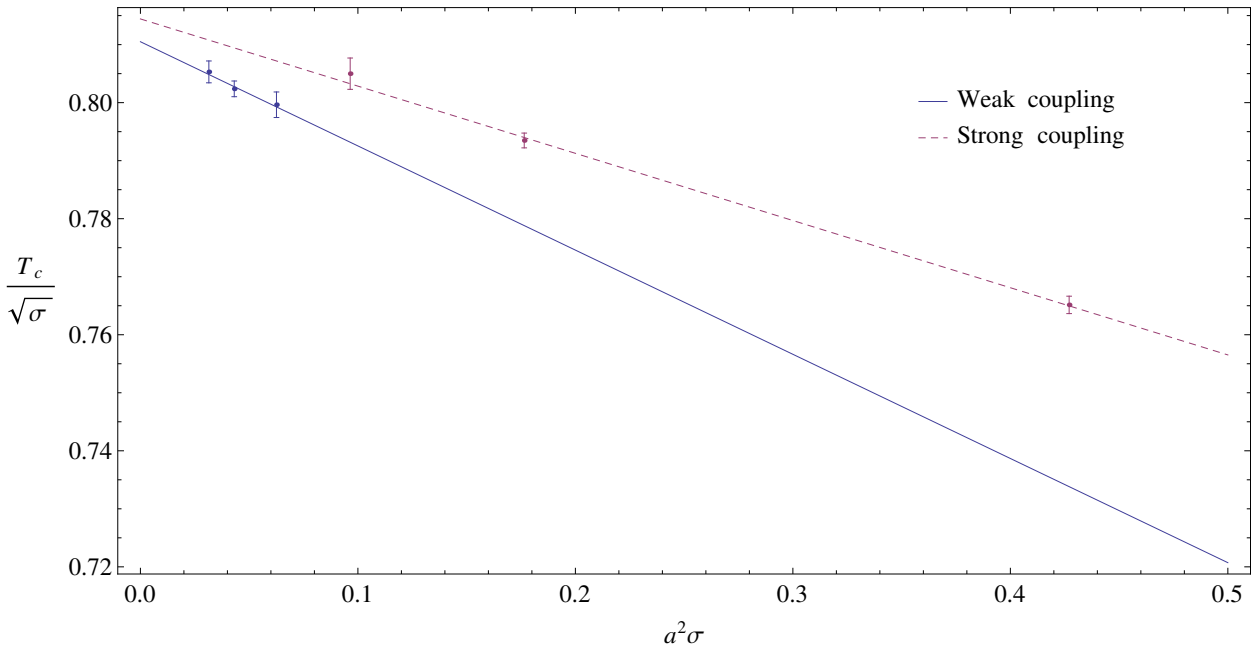

Figure 5.15: Continuum extrapolation of $SO(6)$ deconfining temperatures in string tension units.

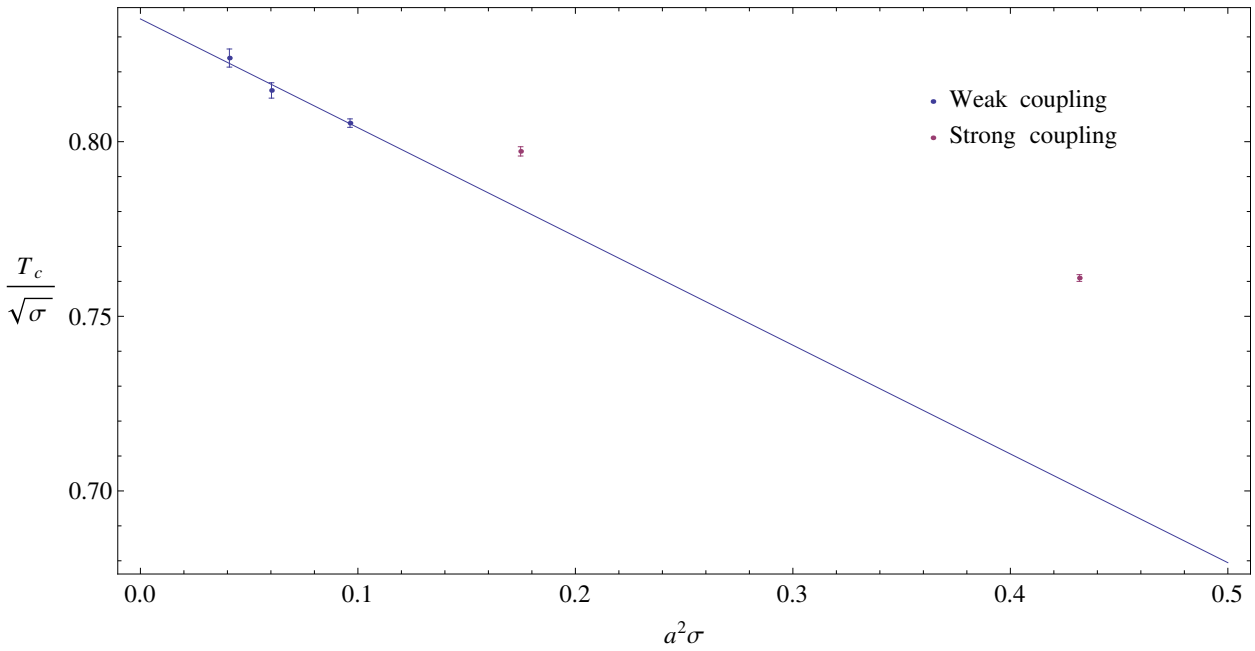

Figure 5.16: Continuum extrapolation of $SO(7)$ deconfining temperatures in string tension units.

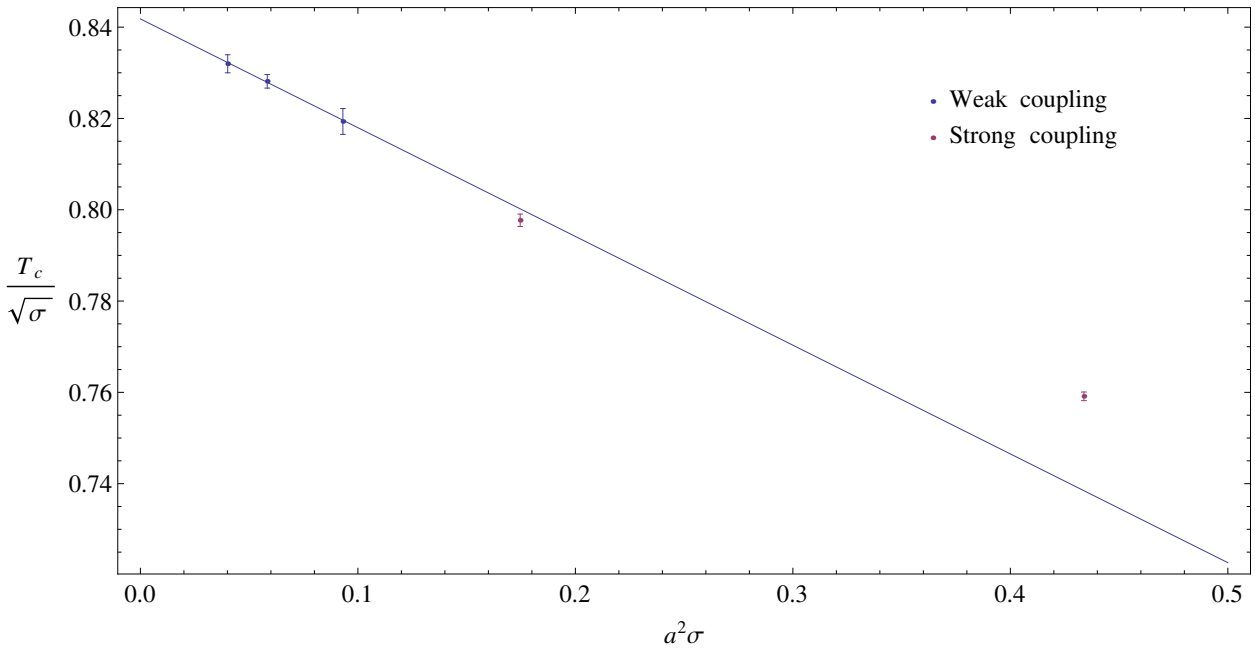

Figure 5.17: Continuum extrapolation of $SO(8)$ deconfining temperatures in string tension units.

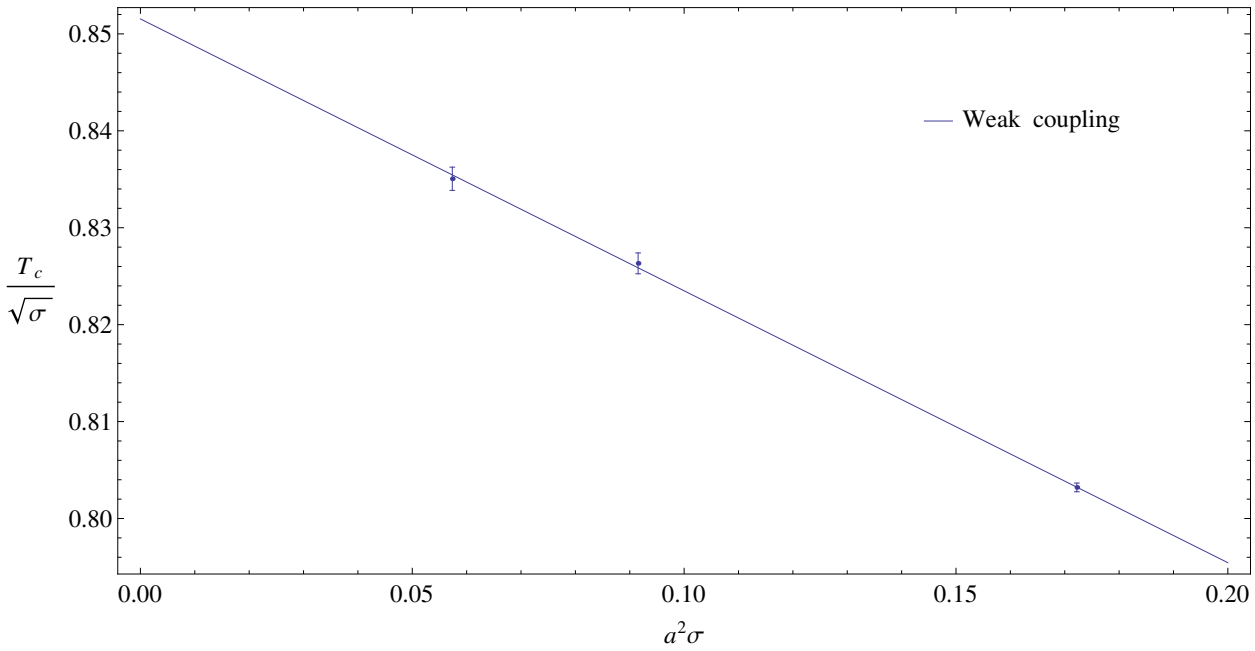

Figure 5.18: Continuum extrapolation of $SO(9)$ deconfining temperatures in string tension units.

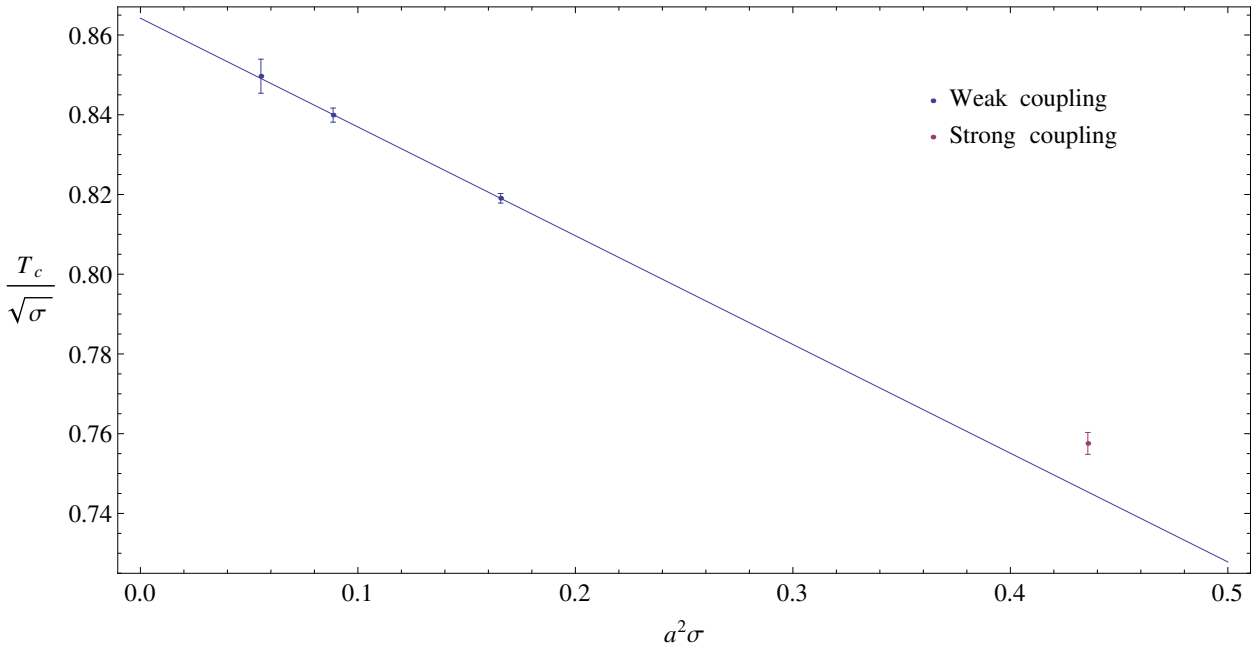

Figure 5.19: Continuum extrapolation of $SO(12)$ deconfining temperatures in string tension units.

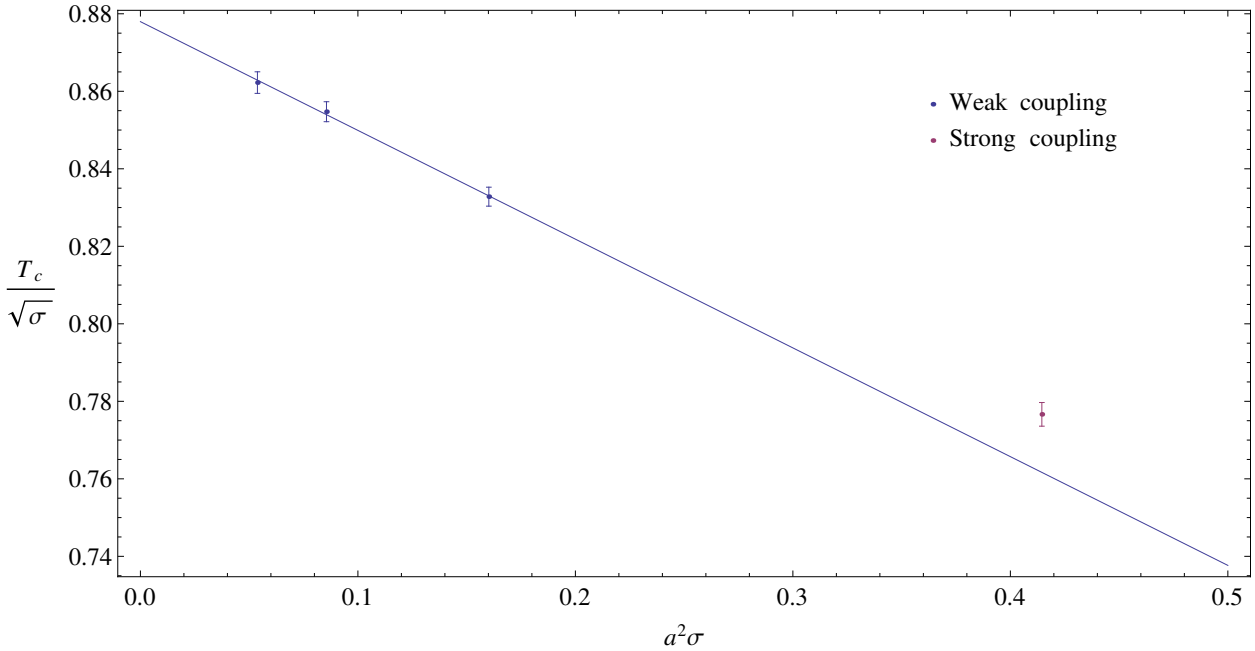

Figure 5.20: Continuum extrapolation of $SO(16)$ deconfining temperatures in string tension units.

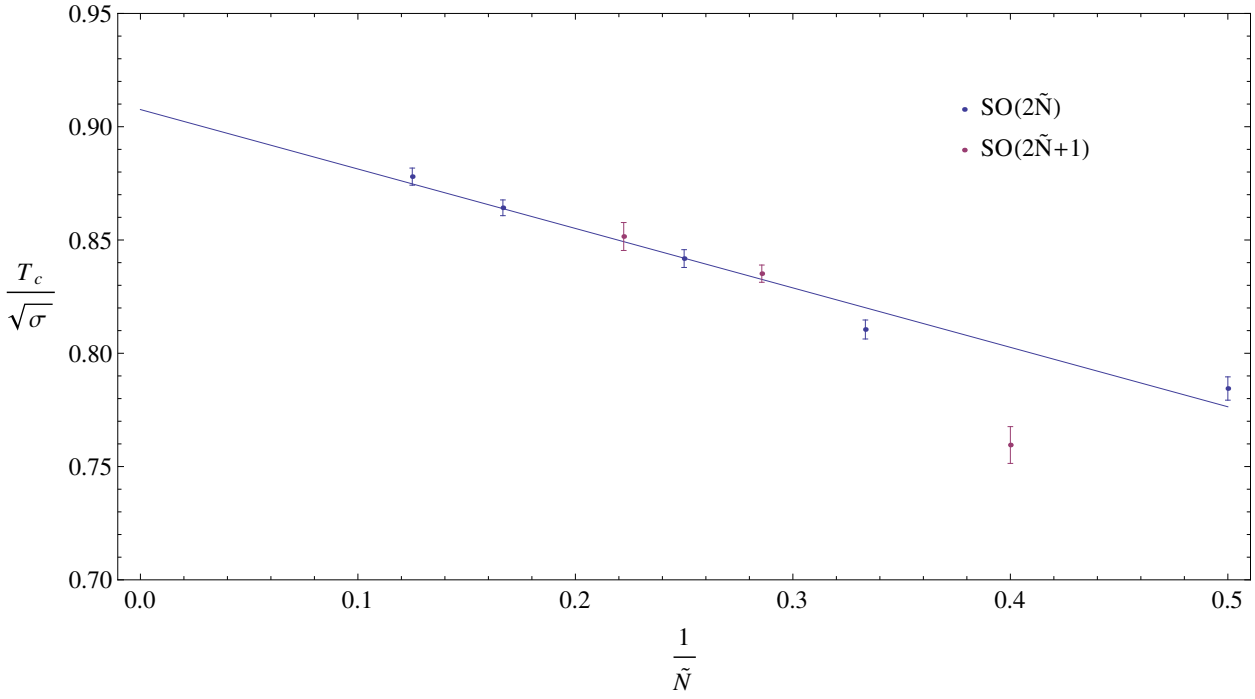

Figure 5.21: Large-$\tilde{N}$ extrapolation of $SO(2\tilde{N})$ deconfining temperatures in string tension units. We plot the $SO(2\tilde{N}+1)$ values in red.

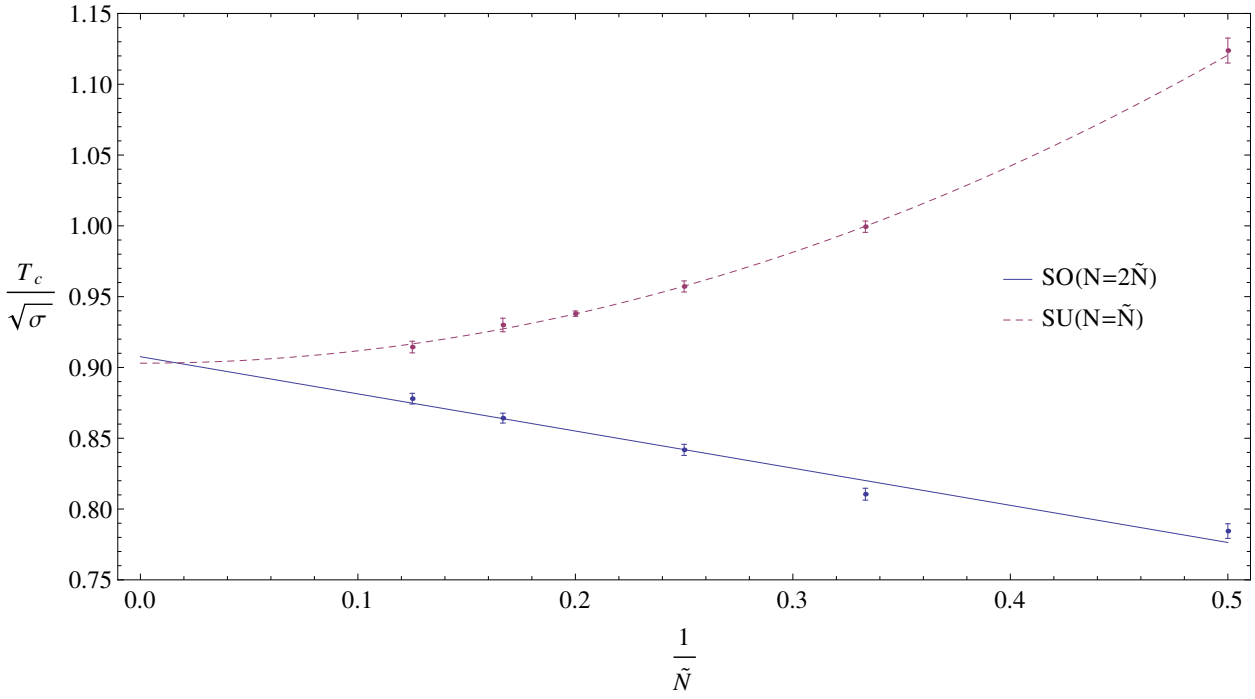

Figure 5.22: Large-$\tilde{N}$ extrapolation of $SO(2\tilde{N})$ and $SU(\tilde{N})$ deconfining temperatures in string tension units.

Conclusions

In this thesis, we presented the string tensions, mass spectrum, and deconfining temperatures of $SO(N)$ gauge theories in $2+1$ dimensions. We calculated the continuum values for various $SO(N)$ theories before extrapolating to the large-N limit. Finally, we compared our $SO(N)$ results to known $SU(N)$ values and showed that they have matching physical quantities between group equivalences.

We showed that lattice techniques, previously used to study $SU(N)$ pure gauge theories, also apply to $SO(N)$ pure gauge theories with only a few adjustments such as a different heat bath algorithm. We found that the same properties of $D = 2+1$ $SU(N)$ theories appear in $D = 2+1$ $SO(N)$ theories such as the order of the deconfining phase transition as well as more general features such as parity doubling. We obtained accurate continuum values through considering a large range of lattice spacing a and a large basis of operators for the string tensions and glueball spectrum, and by looking at a large range of volumes and L_t values for the deconfining temperatures.

We showed that our values match those of known $SU(N)$ values across specific Lie algebra equivalences $SO(4)$ and $SU(2) \times SU(2)$, and $SO(6)$ and $SU(4)$ and that the differing global group properties do not affect the equivalence in the physical properties we investigated.

We discussed the theory behind large-N physics. We firstly extended 't Hooft's $1/N$ argument to $SO(N)$ gauge theories so that we could obtain a large-N limit with $\mathcal{O}(1/N)$ corrections. Secondly, we outlined the perturbative justification behind the large-$\tilde{N}$ orbifold equivalence between $SO(2\tilde{N})$ and $SU(\tilde{N})$ gauge theories. This provided a route linking finite $SO(N)$ and $SU(N)$ results. We showed that our results confirm these expectations in $D = 2+1$ pure gauge theories, despite differing global properties such as centre symmetries. Furthermore, we showed that $SO(2\tilde{N}+1)$ values mostly agree with our large-N extrapolations despite not having the $\mathbb{Z}_2$ symmetry in $SO(2\tilde{N})$ theories.

As we described in this thesis, a potential application of these equivalences is studying problems

in $SU(N)$ QCD theories at finite chemical potential, which the fermion sign problem currently affects. Our results motivate future research in $SO(N)$ gauge theories. Firstly, we might consider the $SO(N)$ hadronic spectrum, which we have not considered in this thesis. Following on from $2+1$ dimensions, we could also consider $3+1$ dimensions. These calculations are more complicated than those in $D = 2+1$ since, as well as the added complexity of calculating at lattice volumes in higher dimensions, there is a bulk transition in $SO(N)$ gauge theories at much smaller lattice spacings than in $D = 2 + 1$ [3]. We have seen that this bulk transition largely does not affect $D = 2 + 1$ calculations except for low L_t in the deconfining temperature results. It is clearly important that the bulk transition occurs at a coupling value where the lattice spacing is not too small, so that the lattice size in lattice units does not need to be very large. Hence, in $D = 3 + 1$ dimensions, the location of the bulk transition makes the task of obtaining a continuum extrapolation at weak coupling much more challenging than in $D = 2 + 1$. Potential solutions to this bulk transition problem include considering much larger lattices or designing a lattice action improvement that shifts the bulk transition to stronger coupling. If successful, these approaches should allow us to test if the large-N equivalence also applies in $D = 3 + 1$, and if $SO(N)$ gauge theories at small N are similar to an $SU(3)$ gauge theory, which would be directly relevant to addressing the QCD sign problem.

Bibliography

[1] K. Symanzik. Continuum limit and improved action in lattice theories: (i). Principles and ϕ^4 theory. *Nuclear Physics B*, 226(1):187 – 204, 1983.

[2] Michael J. Teper. $SU(N)$ gauge theories in 2+1 dimensions. *Phys. Rev. D*, 59:014512, Dec 1998.

[3] Philippe de Forcrand and Oliver Jahn. Comparison of $SO(3)$ and $SU(2)$ lattice gauge theory. *Nuclear Physics B*, 651(1–2):125 – 142, 2003.

[4] Michael Creutz, Laurence Jacobs, and Claudio Rebbi. Monte carlo computations in lattice gauge theories. *Physics Reports*, 95(4):201 – 282, 1983.

[5] A.D. Kennedy and B.J. Pendleton. Improved heatbath method for monte carlo calculations in lattice gauge theories. *Physics Letters B*, 156(5,6):393 – 399, 1985.

[6] Nicola Cabibbo and Enzo Marinari. A new method for updating $SU(N)$ matrices in computer simulations of gauge theories. *Physics Letters B*, 119(4-6):387 – 390, 1982.

[7] Christof Gattringer and Christian B. Lang. *Quantum Chromodynamics on the Lattice*. Springer, 2010.

[8] Howard Georgi. *Lie Algebras In Particle Physics: from Isospin To Unified Theories*. Frontiers in Physics, 1999.

[9] Barak Bringoltz and Michael Teper. Closed k-strings in $SU(N)$ gauge theories: dimensions. *Physics Letters B*, 663(5):429–437, 2008.

[10] Francis Bursa, Richard Lau, and Michael Teper. $SO(2N)$ and $SU(N)$ gauge theories in 2+1 dimensions. *Journal of High Energy Physics*, 2013(5), 2013.

[11] Michael E. Peskin and Daniel V. Schroeder. *An Introduction to Quantum Field Theory*. Westview Press, 1995.

[12] G.'t Hooft. A planar diagram theory for strong interactions. *Nuclear Physics B*, 72(3):461 – 473, 1974.

[13] Aneesh V. Manohar. Large N QCD. pages 1091–1169, 1998.

[14] Sidney Coleman. *Aspects of Symmetry*. Cambridge University Press, 1985.

[15] Mike Blake and Aleksey Cherman. Large N_c equivalence and baryons. *Phys. Rev. D*, 86:065006, Sep 2012.

[16] C. Lovelace. Universality at large N. *Nuclear Physics B*, 201(2):333 – 340, 1982.

[17] Shamit Kachru and Eva Silverstein. 4D conformal field theories and strings on orbifolds. *Phys. Rev. Lett.*, 80:4855–4858, Jun 1998.

[18] Michael Bershadsky and Andrei Johansen. Large N limit of orbifold field theories. *Nuclear Physics B*, 536(1–2):141 – 148, 1998.

[19] Martin Schmaltz. Duality of nonsupersymmetric large N gauge theories. *Phys. Rev. D*, 59:105018, Apr 1999.

[20] Aleksey Cherman, Masanori Hanada, and Daniel Robles-Llana. Orbifold equivalence and the sign problem at finite baryon density. *Phys. Rev. Lett.*, 106:091603, Mar 2011.

[21] Aleksey Cherman and Brian C. Tiburzi. Orbifold equivalence for finite density QCD and effective field theory. *Journal of High Energy Physics*, 2011(6):1–38, 2011.

[22] Mithat Ünsal and Laurence G. Yaffe. (In)validity of large N orientifold equivalence. *Phys. Rev. D*, 74:105019, Nov 2006.

[23] Masanori Hanada and Naoki Yamamoto. Universality of phases in QCD and QCD-like theories. *Journal of High Energy Physics*, 2012(2), 2012.

[24] Masanori Hanada. Large-N_c Universality of Phases in QCD and QCD-like Theories. 2011.

[25] M. Teper. An improved method for lattice glueball calculations. *Physics Letters B*, 183(3–4):345–350, 1987.

[26] M. Teper. The scalar and tensor glueball masses in lattice gauge theory. *Physics Letters B*, 185(1–2):121–126, 1987.

[27] Ph. De Forcrand, G. Schierholz, H. Schneider, and M. Teper. The string and its tension in $SU(3)$ lattice gauge theory: Towards definitive results. *Physics Letters B*, 160(1–3):137–143, 1985.

[28] M. Lüscher, K. Symanzik, and P. Weisz. Anomalies of the free loop wave equation in the WKB approximation. *Nuclear Physics B*, 1733(3):365–396, 1980.

[29] Andreas Athenodorou, Barak Bringoltz, and Michael Teper. Closed flux tubes and their string description in $D = 2 + 1$ $SU(N)$ gauge theories. *Journal of High Energy Physics*, 2011(5), 2011.

[30] Andreas Athenodorou, Barak Bringoltz, and Michael Teper. Closed flux tubes and their string description in $D = 3 + 1$ $SU(N)$ gauge theories. *Journal of High Energy Physics*, 2011(2), 2011.

[31] Ofer Aharony and Matthew Dodelson. Effective string theory and nonlinear lorentz invariance. *Journal of High Energy Physics*, 2012(2), 2012.

[32] G. Peter Lepage and Paul B. Mackenzie. Viability of lattice perturbation theory. *Phys. Rev. D*, 48:2250–2264, Sep 1993.

[33] Biagio Lucini and Michael Teper. $SU(N)$ gauge theories in 2+1 dimensions – further results. *Phys. Rev. D*, 66:097502, Nov 2002.

[34] Barak Bringoltz and Michael Teper. A precise calculation of the fundamental string tension in $SU(N)$ gauge theories in 2+1 dimensions. *Physics Letters B*, 645(4):383–388, 2007.

[35] Harvey B. Meyer. The spectrum of $SU(N)$ gauge theories in finite volume. *Journal of High Energy Physics*, 2005(03):064, 2005.

[36] M. Lüscher. Volume dependence of the energy spectrum in massive quantum field theories. i. stable particle states. *Communications in Mathematical Physics*, 104(2):177–206, 1986.

[37] Biagio Lucini, Antonio Rago, and Enrico Rinaldi. Glueball masses in the large N limit. *Journal of High Energy Physics*, 2010(8), 2010.

[38] H.B. Meyer and M.J. Teper. High spin glueballs from the lattice. *Nuclear Physics B*, 658(1–2):113 – 155, 2003.

[39] J Greensite. The confinement problem in lattice gauge theory. *Progress in Particle and Nuclear Physics*, 51(1):1 – 83, 2003.

[40] Harvey B Meyer and Michael J Teper. Glueball regge trajectories in (2+1)-dimensional gauge theories. *Nuclear Physics B*, 668(1–2):111 – 137, 2003.

[41] Heinz J. Rothe. *Lattice Gauge Theories: An Introduction.* World Scientific Lecture Notes in Physics, 2005.

[42] Biagio Lucini, Michael Teper, and Urs Wenger. Properties of the deconfining phase transition in $SU(N)$ gauge theories. *Journal of High Energy Physics*, 2005(02):033, 2005.

[43] Murty S. S. Challa, D. P. Landau, and K. Binder. Finite-size effects at temperature-driven first-order transitions. *Phys. Rev. B*, 34:1841–1852, Aug 1986.

[44] K. Binder and D. P. Landau. Finite-size scaling at first-order phase transitions. *Phys. Rev. B*, 30:1477–1485, Aug 1984.

[45] K. Binder. Finite size effects on phase transitions. *Ferroelectrics*, 73(1):43–67, 1987.

[46] K. Binder. Finite size scaling analysis of ising model block distribution functions. *Zeitschrift für Physik B Condensed Matter*, 43(2):119–140, 1981.

[47] Vladimir Privman and Michael E. Fisher. Finite-size effects at first-order transitions. *Journal of Statistical Physics*, 33(2):385–417, 1983.

[48] Vladimir Privman. *Finite-Size Scaling Theory.* World Scientific Lecture Notes in Physics, 1990.

[49] Hildegard Meyer-Ortmanns. Phase transitions in quantum chromodynamics. *Rev. Mod. Phys.*, 68:473–598, Apr 1996.

[50] Jack Liddle and Michael Teper. The deconfining phase transition in $D = 2 + 1$ $SU(N)$ gauge theories. arXiv:0803.2128, 2008.

[51] Alan M. Ferrenberg and Robert H. Swendsen. New monte carlo technique for studying phase transitions. *Phys. Rev. Lett.*, 61:2635–2638, Dec 1988.

[52] Alan M. Ferrenberg and Robert H. Swendsen. Optimized monte carlo data analysis. *Phys. Rev. Lett.*, 63:1195–1198, Sep 1989.

[53] Biagio Lucini, Michael Teper, and Urs Wenger. The high temperature phase transition in $SU(N)$ gauge theories. *Journal of High Energy Physics*, 2004(01):061, 2004.

[54] Kieran Holland. Another weak first order deconfinement transition: three-dimensional $SU(5)$ gauge theory. *Journal of High Energy Physics*, 2006(01):023, 2006.

[55] Kieran Holland, Michele Pepe, and Uwe-Jens Wiese. Revisiting the deconfinement phase transition in $SU(4)$ yang-mills theory in 2+1 dimensions. *Journal of High Energy Physics*, 2008(02):041, 2008.

[56] S. Huang, K.J.M. Moriarty, E. Myers, and J. Potvin. The density of states method and the velocity of sound in hot QCD. *Zeitschrift für Physik C Particles and Fields*, 50(2):221–236, 1991.

[57] Benjamin Svetitsky and Laurence G. Yaffe. Critical behavior at finite-temperature confinement transitions. *Nuclear Physics B*, 210(4):423 – 447, 1982.

[58] Biagio Lucini and Mike Teper. $SU(N)$ gauge theories in four dimensions: exploring the approach to $N = \infty$. *Journal of High Energy Physics*, 2001(06):050, 2001.